POLARITON CONDENSATES IN A TRAP AND PHOTON LASING IN TWO-DIMENSIONAL SEMICONDUCTOR MICROCAVITIES

by

Bryan L Nelsen

B.S., Physics, Georgia Southern University, 2005

M.S., Physics, University of Pittsburgh, 2008

Submitted to the Graduate Faculty of

the Kenneth P. Dietrich School of Arts and Sciences in partial fulfillment

of the requirements for the degree of

Doctor of Philosophy

University of Pittsburgh

2012

UNIVERSITY OF PITTSBURGH

DEPARTMENT OF PHYSICS AND ASTRONOMY

This dissertation was presented

by

Bryan L Nelsen

It was defended on

April 11, 2012

and approved by

David W. Snoke, Physics and Astronomy

M.V. Gurudev Dutt, Physics and Astronomy

David Jasnow, Physics and Astronomy

James A. Mueller, Physics and Astronomy

Joel Falk, Electrical and Computer Engineering

Dissertation Director: David W. Snoke, Physics and Astronomy

POLARITON CONDENSATES IN A TRAP AND PHOTON LASING IN TWO-DIMENSIONAL SEMICONDUCTOR MICROCAVITIES

Bryan L Nelsen, PhD

University of Pittsburgh, 2012

Recent experiments in microcavity polaritons have shown many effects that can be associated with the phase transition known as Bose-Einstein condensation; these effects include a dramatic increase in both the population of the zero-momentum state and lowest-lying energy state, the formation of first- and second-order coherence in both space and time, and the spontaneous polarization of the polariton ensemble. However, these same results can also be a consequence of lasing. The primary focus of this dissertation is to examine these effects and determine to what degree the effects of lasing can be distinguished from those of Bose-Einstein condensation. Bose-Einstein condensation in a two-dimensional weakly-interacting gas, such as polaritons, is predicted to not occur without the aid of spatial confinement, i.e., a trap. Polaritons were subjected to various methods of confinement, including stress traps and exciton-reservoir traps, and the signatures of condensation in these traps are shown to be dramatically different than those of lasing in a system without confinement. It is also shown that, when driving the polariton condensate to very high density, the polaritons dissociate and the lasing transition succeeds Bose-Einstein condensation. The geometry of the trapping potential was also exploited to indicate that the symmetry of the condensate momentum-space distribution followed that of the ground state of the trap.

At reasonable densities, the lifetime of polaritons is of the same order as the polariton-polariton interaction time, hence the previously shown effects are an incomplete Bose-Einstein condensation since thermodynamic equilibrium is not reached. A second part of this work has been to extend the lifetime of polaritons to achieve a more thermalized en-

semble. We do this by increasing the Q factor of the microcavity through improving the reflectivity of the mirrors. These samples exhibit many interesting phenomenon since the polariton lifetime becomes long enough to traverse significant distances. Here, Bose-Einstein condensation occurs at a point spatially separated from the excitation source, ruling out the possibility of nonlinear amplification of the pump laser. Also, a superfluid-like transition is observed, giving rise to possible signatures of vortices.

Keywords: Polariton, Bose-Einstein Condensation, Lasing, Microcavity, Quantum Well, Exciton, Stress Trap, Electron-Hole Exchange, Valence-Band Mixing.

TABLE OF CONTENTS

LIST OF TABLES

LIST OF FIGURES

PREFACE

First of all, I would like to thank my wife Julia for her caring and support during this endeavor. I could not have finished this work without her encouragement and love.

Secondly, the work done in this thesis would not have been possible if it were not for the aid of others in this research group. I would like to thank Jeff Wuenschell and Nick Sinclair for their support on the theoretical aspects of this project. Also, many thanks to Mark Steger and Gangqiang Liu for all of their assistance in laboratory procedures and experiments. I am also thankful for the leadership of my predecessors, Ryan Balili and Vincent Hartwell, by initiating this project and guiding me in the laboratory during the early stages of this work. Most importantly, I am thankful for the guidance and patience bestowed upon me by my adviser, David W. Snoke, to whom I am indebted for giving me the opportunity to pursue my scientific ambitions in the laboratory.

Finally, thanks to all the staff in the Physics Department who helped make all of this possible and thanks to my friends and family who supported me through it all.

1.0 INTRODUCTION

An exciton-polariton, as the name suggests, is a composite particle comprised of a photon and an exciton; an exciton is a conduction-band electron Coulomb bound to a valence-band hole. Given that the state space spanned by the polariton is bosonic in nature, namely, it is comprised of a spin-1 photon and an exciton with integer spin, one expects that it will follow Bose statistics, and for a given density, and below a critical temperature, the particles may potentially Bose condense. Several features make the polariton uniquely qualified for studying Bose-Einstein Condensates (BEC). Since polaritons are part photon, they have a very small effective mass ($10^{-4}m_e$, where m_e is the electron mass), and therefore a high critical temperature. Unlike photons, however, they have an exciton-like component which gives them a scattering cross-section and the ability to thermalize. Polaritons also have a finite lifetime which is governed primarily by the microcavity photon states. In many structures, polaritons typically only undergo a few scattering events in their lifetime; as a result, the polariton gas is only in a quasi-thermodynamic equilibrium, pushing the envelope of the methods used in statistical thermodynamics.

These features of the polariton make it a desirable system to study, and in fact, many groups have already done so [1, 2, 3, 4, 5, 6]. What makes our experiments unique is that the polaritons are trapped by applying stress to the sample [7], whereas other groups rely on defect fluctuations [8] or complex microstructures [9] for trapping. Although there is much experimental evidence showing polaritons undergo a phase transition exhibiting the spontaneous formation of coherence, there has been some debate as to what degree this phenomenon can be called BEC. This is due, in part, to the fact that the polariton lifetime is typically so short that they only reach a quasi-equilibrium state. A focus of this dissertation is to examine some of the unanswered questions as to whether or not the observed phenomenon

is truly BEC [10, 11]. A greater understanding of this spontaneous coherence may lead to exciting new discoveries in fundamental physics, and may mean that polaritons will find their way into new applications, such as low-threshold coherent light sources.

In this work, we also focus on engineering polariton structures to push the polariton gas closer to equilibrium by increasing the lifetime by a factor of ∼20 over existing structures [12]. We also pay close attention to minimize polariton density fluctuations caused by inherent fluctuations in the lab equipment used to create the polariton gas. Since the condensate's phase stability is dependent on the interaction energy, and hence the density, minimizing these fluctuations can have a dramatic effect on the coherence times of the condensate.

1.1 POLARITONS AS QUASIPARTICLES

The study of light-matter interactions is nothing new. Even a detailed understanding of a classical field interacting with a quantum mechanical oscillator dates back almost 80 years. But it wasn't until the full second-quantized picture of light and excitons [13] was completed that we were able to gain some understanding of the polariton. This led to the observation of the existence of polaritons in specially tailored microcavity structures [14], and subsequently, the experimental evidence that polaritons obeyed Bose statistics [15]. That began the search to see the now ubiquitous BEC of polaritons [2].

To understand the many-body effects of polaritons, we first must understand the underlying physical structure of polaritons. A brief inquiry into semiconductor physics and photons naturally begins this discussion since the polaritons that we wish to discuss are a quantum superposition of the fundamental excitations in these media. In the following sections, these composite particles will be dissected into their constituent parts in order to gain a better understanding of their behavior.

1.1.1 Semiconductors, Electrons, and Holes

The goal of this section is to introduce the second-quantized picture of semiconductors. The second-quantized picture is most relevant in this work since we'd like to understand how the excitations in these media behave like quasiparticles and the consequences of treating these excitations as such. This discussion begins with the full many-body Hamiltonian for electrons interacting with themselves through the Coulomb interaction along with a general periodic potential $U(\mathbf{x})$ from the electrons interacting with the lattice:

$$\begin{aligned} H = &\int \mathbf{\Psi}(\mathbf{x})^\dagger \left(-\frac{\hbar^2}{2m}\nabla^2 + U(\mathbf{x}) \right) \mathbf{\Psi}(\mathbf{x}) d\mathbf{x} \\ &+ \frac{1}{2} \int \int \mathbf{\Psi}(\mathbf{x})^\dagger \mathbf{\Psi}(\mathbf{x}')^\dagger \frac{e}{|\mathbf{x}-\mathbf{x}'|} \mathbf{\Psi}(\mathbf{x}) \mathbf{\Psi}(\mathbf{x}') d^3x d^3x'. \end{aligned} \tag{1.1}$$

Here m_e is the electron mass, $\hbar$ is Plank's constant divided by 2π, e is the charge of the electron and $\mathbf{\Psi}(\mathbf{x})$ is the electron field operator. Without loss of generality, I've also dropped the spin index for simplicity and will only consider spin when it is necessary. In the standard techniques of solid state physics (see for example [16, 17, 18]), we can exploit the periodicity and symmetry of the lattice potential. The basis states of the system become the Bloch functions with a corresponding destruction operator for that state. Hence we can expand the many-body wave function as:

$$\Psi(\mathbf{x}) = \frac{1}{\sqrt{V}} \sum_{n,\mathbf{k}} e^{i\mathbf{k}\cdot\mathbf{x}} u_{n,\mathbf{k}}(\mathbf{x}) \mathbf{b}_{n,\mathbf{k}}. \tag{1.2}$$

This is just standard notation, where n labels the bands, $\mathbf{k}$ is the crystal momentum, $u_{n,\mathbf{k}}(\mathbf{x})$ are known as the cell functions and $\mathbf{b}_{n,\mathbf{k}}$ are the fermionic destruction operators. Just as useful is the fact that the cell functions at zone center, $u_{n,0}(\mathbf{x})$, have the full symmetry of the crystal and these states at $\mathbf{k} = 0$ form a complete, orthonormal basis for the expansion of any other states:

$$u_{n,\mathbf{k}}(\mathbf{x}) = \sum_m a_{n,m}(\mathbf{k}) u_{m,0}(\mathbf{x}). \tag{1.3}$$

This fact will be used later when calculating, under the formalism of $\mathbf{k}\cdot\mathbf{p}$ theory, the Luttinger-Köhn [19] and Pikus-Bir [20] Hamiltonians. These Hamiltonians are very powerful tools when considering quantum confinement and deformed lattices.

For most III-V and II-VI semiconductors, the uppermost valence-band states usually wind up with p-like symmetry due to the nature of the bonds formed with neighboring atoms. In particular, our samples consist of GaAs, AlAs, and $Al_{0.2}Ga_{0.8}As$. All three of these materials have valence-band cell functions that exhibit T_d symmetry [16]:

$$\begin{aligned}
u_{1,0}(\mathbf{x}) &= \mid 3/2, 3/2\rangle = \frac{-1}{\sqrt{2}} \mid (X + iY)\uparrow\rangle \\
u_{2,0}(\mathbf{x}) &= \mid 3/2, -3/2\rangle = \frac{1}{\sqrt{2}} \mid (X - iY)\downarrow\rangle \\
u_{3,0}(\mathbf{x}) &= \mid 3/2, 1/2\rangle = \frac{-1}{\sqrt{6}} \mid (X + iY)\downarrow\rangle + \sqrt{\frac{2}{3}} \mid Z\uparrow\rangle \\
u_{4,0}(\mathbf{x}) &= \mid 3/2, -1/2\rangle = \frac{1}{\sqrt{6}} \mid (X - iY)\uparrow\rangle + \sqrt{\frac{2}{3}} \mid Z\downarrow\rangle \\
u_{5,0}(\mathbf{x}) &= \mid 1/2, 1/2\rangle = \frac{1}{\sqrt{3}} \mid (X + iY)\downarrow\rangle + \sqrt{\frac{1}{3}} \mid Z\uparrow\rangle \\
u_{6,0}(\mathbf{x}) &= \mid 1/2, -1/2\rangle = \frac{1}{\sqrt{3}} \mid (X - iY)\uparrow\rangle - \sqrt{\frac{1}{3}} \mid Z\downarrow\rangle,
\end{aligned} \tag{1.4}$$

with the notation $\mid J, m\rangle$ being standard quantum notation to deal with total angular momentum. The conduction-band states are trivially s-like. Figure 1.1 shows the near $\mathbf{k} = 0$ cartoon of the conduction- and valence-band states using the Luttinger-Kohn Hamiltonian derived in Appendix C. In most cases we can completely ignore the split-off band ($\mid 1/2, \pm 1/2\rangle$ states) due to its energy separation from the other states of interest. This energy splitting comes about due to spin-orbit interaction. The states labeled $\mid 3/2, \pm 3/2\rangle$ are known as heavy-hole states because of their heavier effective mass, while the $\mid 3/2, \pm 1/2\rangle$ states are known as the light-hole states.

The electron/hole picture gives us a more convenient tool to treat the almost infinite number of electrons in the valence band. Here we adopt the picture of the Fermi sea [21] and instead of thinking about an excited electron in the conduction band and the remaining electrons in the valence band, we consider the vacancy in the valence band as its own particle. This particle is known as a hole, and its creation operator is the time-reversed valence-band destruction operator. Thus the hole creation operator is defined as the removal of an electron from the valence band:

$$\mathbf{h}^{\dagger}_{\mathbf{k},\uparrow} = \mathbf{b}_{v,-\mathbf{k},\downarrow}. \tag{1.5}$$

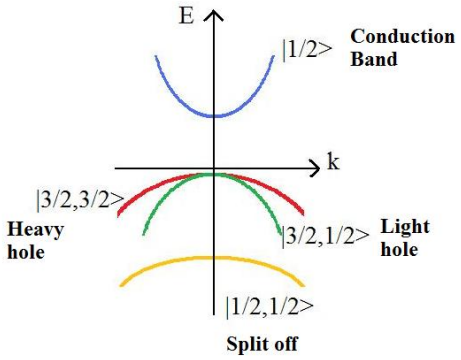

Figure 1.1: Depiction of the band structure of a III-V semiconductor such as GaAs.

In the picture of the Fermi sea, the hole becomes almost completely analogous to the positron with only a few differences enumerated below. Because we are no longer thinking of electrons in the valence band, electron creation operators will only act on the conduction-band states such that we'll redefine $\mathbf{b}_{c,\mathbf{k}}$ as $\mathbf{e}_{\mathbf{k}}$. Using the assumptions of the Bloch functions and adopting the electron-hole picture, Eq. (1.1) can be simplified as

$$\begin{aligned} H = &\sum_{\mathbf{k}} E_e(\mathbf{k}) \mathbf{e}^\dagger_{\mathbf{k}} \mathbf{e}_{\mathbf{k}} + \sum_{\mathbf{k}} E_h(\mathbf{k}) \mathbf{h}^\dagger_{\mathbf{k}} \mathbf{h}_{\mathbf{k}} \\ &+ \frac{1}{2} \sum_{\mathbf{k},\mathbf{p},\mathbf{q}\neq\mathbf{0}} V(\mathbf{q}) \left(\mathbf{e}^\dagger_{\mathbf{k}+\mathbf{q}} \mathbf{e}^\dagger_{\mathbf{p}-\mathbf{q}} \mathbf{e}_{\mathbf{p}} \mathbf{e}_{\mathbf{k}} + \mathbf{h}^\dagger_{\mathbf{k}+\mathbf{q}} \mathbf{h}^\dagger_{\mathbf{p}-\mathbf{q}} \mathbf{h}_{\mathbf{p}} \mathbf{h}_{\mathbf{k}} \right) \\ &- \sum_{\mathbf{k},\mathbf{p},\mathbf{q}\neq\mathbf{0}} V(\mathbf{q}) \mathbf{e}^\dagger_{\mathbf{k}+\mathbf{q}} \mathbf{h}^\dagger_{\mathbf{p}-\mathbf{q}} \mathbf{h}_{\mathbf{p}} \mathbf{e}_{\mathbf{k}}. \end{aligned} \tag{1.6}$$

It may not appear much simpler than Eq. (1.1), but in the next section we will show that, in certain limits, this Hamiltonian is diagonalizable with a simple transformation. Appendix A has full derivation of Eq. (1.6).

1.1.1.1 Quantum Wells

Modern semiconductor growth techniques provide an interesting mechanism to study quantum confinement. Using epitaxial growth, it is possible to create structures composed of layers of different materials while also controlling the width of these layers down to the precision of a single atomic layer [22]. For GaAs, a single atomic layer

is represented by a thickness of just 2.5 Å. One of the fundamentally interesting structures that can be created with these techniques is a quantum well. Figure 1.2 shows a sandwich of two different materials, GaAs and AlAs. Because these two materials have different bandgap energies, when placed next to each other they form a finite square well. Since the light hole and heavy hole bands have different masses, they also have different square well confinement energies, with the light hole having more confinement energy than the heavy hole. Essentially, the quantum well pins the wavevector, **k**, of the electrons and holes along one dimension, leaving the other two dimensions as degrees of freedom. Because of this confinement, the confined states of the square well are 2-dimensional (2D).

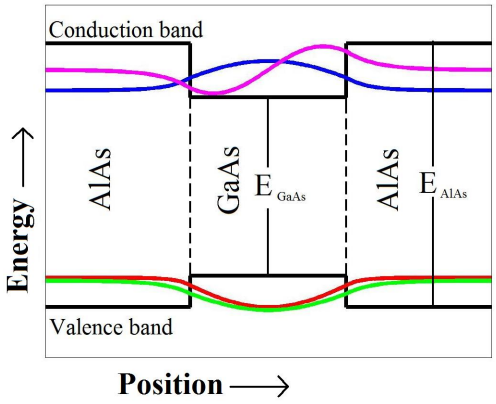

Figure 1.2: Calculated quantum-well wave functions for the conduction and valence bands using Model-Solid theory [23] and the Luttinger-Kohn Hamiltonian. The blue curve is the ground state conduction band wave function; the purple curve is the first excited state conduction band wave function; the red curve is the ground state heavy-hole wave function; the green curve is the ground state light-hole wave function. E_{GaAs} and E_{AlAs} are the band gap energies for GaAs and AlAs respectively

At this point it is necessary to make an aside which is a recurring argument that will be made throughout this work. For the quantum wells shown in Fig. 1.2, which are similar to the ones used in our samples, the light hole has a confinement energy of ∼30 meV more than the heavy hole. If we compare that to $k_B T$, we find that the thermal occupation of this state is negligible until the temperature is ∼75 K. Hence, when working at low temperatures, the occupation of this state becomes negligible for most cases. This same argument can also be

applied to the excited states of the quantum well which are energetically separated by more than 30 meV.

1.1.1.2 Electron-Hole Creation and Recombination Returning to the analogy in which the hole is like a positron and the conduction-band electron is like a free space electron, we expect that the electron and the hole can annihilate and produce a photon. This is indeed the case. The annihilation of the electron and hole can be thought of as the conduction-band electron simply transitioning back to the hole in the valence state. In order to conserve energy, a photon must be created. This process works in reverse too; a photon can be absorbed to create an electron-hole pair. To take this transition into account, we must first add another term to the Hamiltonian in (1.6):

$$H_{int} = \int \Psi^{\dagger}(\mathbf{x}) \left(\frac{-e}{m_e} \mathbf{A} \cdot \mathbf{p} \right) \Psi(\mathbf{x}) d^3x. \tag{1.7}$$

here $\mathbf{A}$ is the vector potential, and we are working in the Coulomb gauge. Since we are only interested in the states near zone center, the assumptions of the long wavelength approximation apply (see for example [16, 24]). Under the same methods we used to arrive at Eq. (1.6), and if we treat the electric field as a classical wave, this equation simplifies to

$$= -\frac{e\mathbf{A_0}}{2m_e} \cdot \left[\int_{\Omega_{\text{cell}}} \frac{d\mathbf{x}}{\Omega}_{\text{cell}} u^*_{c,\mathbf{k_c}}(\mathbf{x}) \mathbf{p} u_{v,\mathbf{k_v}}(\mathbf{x}) \right] \mathbf{b}^{\dagger}_{c,\mathbf{k_c}} \mathbf{b}_{v,\mathbf{k_v}} \delta_{\mathbf{k_c},\mathbf{k_v}+\mathbf{k_p}}. \tag{1.8}$$

Here, Ω_{cell} represents the volume of the unit cell and $\mathbf{k_p}$ is the electric field wavevector. Buried in this equation are the selection rules for which an electron-hole pair can be created or destroyed through interactions with an electric field. Clearly, momentum is also conserved. One only needs to calculate the matrix elements $1/\Omega_{\text{cell}} \int_{\Omega_{\text{cell}}} d^3x u^*_{c,\mathbf{k_c}}(\mathbf{x}) \mathbf{p} u_{v,\mathbf{k_v}}(\mathbf{x}) \equiv \boldsymbol{\mu}$, where $\boldsymbol{\mu}$ is known as the dipole matrix, to determine if the transition is allowed.

1.1.2 Excitons

With the filled valence band and empty conduction band of a semiconductor being analogous to the ground state of the vacuum, it is easy to envision once a particle-antiparticle pair is created, that positronium-like states can form. Just as an electron and positron can form hydrogen-like bound states known as positronium, conduction-band electrons and valence-band holes form bound states inside a semiconductor known as excitons. These particle-antiparticle pairs many properties similar to the electron-positron pair: both have finite lifetimes owing to the fact that they can annihilate; both form quantized orbits similar to the hydrogen atom; and both are, on certain length scales, composite bosons. The effective mass of the exciton can be much lighter ($\sim$0.1 m_e [25]) than that of positronium ($2m_e$); also, the binding energy of the exciton is reduced due to screening of the dielectric constant in the medium and the reduced mass of the exciton. The 3-dimensional (3D) binding energy in a dielectric medium is

$$\Delta_{3D} = \frac{\mu e^4}{2\hbar^2 \epsilon^2 n^2}, \tag{1.9}$$

where μ is the reduced mass between the electron and the hole, e is the electron charge and ϵ is the dielectric constant of the material. For GaAs ($\epsilon \approx 12.6\epsilon_o$ [25]), the binding energy is reduced significantly from that of positronium.

Here we will restrict ourselves to exclusively discussing Wannier-Mott excitons because these are the types of excitons that exist in the most generic semiconductor microcavity polariton structures; however, as a side note, recent experiments in polymer-based microcavity polaritons [26] have Frenkel-like excitons. The Wannier-Mott exciton is a Coulomb-bound electron-hole pair with weak binding energy such that its wave function spans many lattice cells. Wannier-Mott excitons have a typical binding energy of less than 0.1 eV. In fact, in GaAs the 3D binding energy is only around 4 meV [25].

Looking at the Hamiltonian in Eq. (1.6), the second line has terms that look like $\hat{N}^2$, where $\hat{N}$ is the number operator. In the low density limit these terms become negligible. If we neglect them, we can diagonalize Eq. (1.6) with the following transformation:

$$\mathbf{X}_\nu^\dagger(\mathbf{K}) \equiv \sum_{\mathbf{k},\mathbf{k}'} \delta_{\mathbf{K},\mathbf{k}+\mathbf{k}'} \phi_\nu(\mathbf{p}) \mathbf{h}_{\mathbf{k}'}^\dagger \mathbf{e}_{\mathbf{k}}^\dagger. \tag{1.10}$$

This operator is known as the exciton creation operator, where $\phi_\nu(\mathbf{p})$ is the center-of-mass hydrogen wave function as described above and ν is the exciton state index, and $\mathbf{p} = \alpha\mathbf{k} - \beta\mathbf{k}'$ is the relative momentum between the electron and hole with $\alpha = m_e/(m_e + m_h)$ and $\beta = m_h/(m_e + m_h)$. The new form of Eq. (1.6) under this transformation becomes

$$H = \sum_{\nu,\mathbf{K}} E_X^\nu(\mathbf{K}) \mathbf{X}_\nu^\dagger(\mathbf{K}) \mathbf{X}_\nu(\mathbf{K}), \tag{1.11}$$

where $E_X^\nu(\mathbf{K})$ is the k-dependent energy of one exciton.

When excitons are confined in quantum wells, as discussed in the previous section, they behave as 2D particles and their dispersion relation is given by

$$E_X(\mathbf{k}_\parallel) = \frac{\hbar^2 {\mathbf{k}_\parallel}^2}{2m^*} + E_{conf}(\mathbf{k}_\perp) + E_{gap} - \Delta_{2D}, \tag{1.12}$$

where $\mathbf{k}_\parallel$ is the exciton center-of-mas wavevector in the plane of the quantum well, m^* is the exciton effective mass, and E_{conf} is the total confinement energy of both the electron and hole. Δ_{2D} is the two-dimensional exciton binding energy, which is different from the 3D binding energy because the quantum wells "freeze out" the third dimension of motion. Δ_{2D} can only be calculated in closed form for the ideal case where the excitons are truly 2D; in reality, there is some evanescent component of the electron and hole wave functions into the barriers of the quantum wells causing the binding energy to be somewhere in between Δ_{2D} and Δ_{3D}. For the ideal case, $\Delta_{2D} = 4\Delta_{3D}$; however, for the real case the binding energy is also a function of well width [27].

We've already invoked the low density limit in order to use the exciton operator (Eq. (1.10)) to diagonalize the Hamiltonian. Let us look at the implications this has toward the bosonic nature of the exciton. From Eq. (1.10) we can calculate the commutator and we notice that in the low density limit, excitons can be approximately treated statistically as bosons. This has profound applications later on when thinking about polaritons. Taking the commutator one finds [55]:

$$\begin{aligned}\left[\mathbf{X}_\mu(\mathbf{K}), \mathbf{X}_\nu^\dagger(\mathbf{K}')\right] = \delta_{\mu,\nu}\delta_{\mathbf{K},\mathbf{K}'} &- \sum_{\mathbf{p}} \phi_\nu^*(\alpha\mathbf{K}' - \mathbf{p})\phi_\mu(\alpha\mathbf{K} - \mathbf{p}) \mathbf{e}_{\mathbf{K}-\mathbf{p}}^\dagger \mathbf{e}_{\mathbf{K}'-\mathbf{p}} \\ &- \sum_{\mathbf{p}} \phi_\nu^*(\mathbf{p} - \beta\mathbf{K})\phi_\mu(\mathbf{p} - \beta\mathbf{K}) \mathbf{h}_{\mathbf{K}-\mathbf{p}}^\dagger \mathbf{h}_{\mathbf{K}'-\mathbf{p}}.\end{aligned} \tag{1.13}$$

The summed terms in Eq. (1.13) go to zero in the limit that the spacing between excitons is much smaller than their Bohr radius. In other words, we can think of one electron pairing with only one hole. In the opposite, high density limit, we wind up with a plasma of unbound electrons and holes where the particles cannot bind due to screening and therefore may not form bosons, at least in the context of the Coulomb interaction. As a side note, this limit is not contradictory to the necessary density to achieve a BEC of excitons, since the relevant limit that is required in that case is that the interparticle spacing must be comparable to the deBroglie wavelength of the exciton, and this can always be made to occur at low density if the temperature is sufficiently low.

When analyzing the dipole moment of the exciton, we find that it differs from that of free electron-hole pair. Because the electron and hole are bound, the electron and hole are correlated, which changes the oscillator strength for the particular type of crystal. Because angular momentum must be conserved, spin ± 1 excitons of both the light and heavy hole band can be created or destroyed in a single-photon process. The radiative rate is directly related to the spatial overlap of the electron and hole wave functions. Quantum confinement to 2D, provided by the quantum well, increases the optical dipole moment by forcing an larger spatial overlap of the electron and hole in the $1s$ state [23]. Because of the difference in overlap between the light hole with the conduction-band electron and heavy hole with the conduction-band electron, along with the different effective masses of the light and heavy hole, the heavy-hole exciton couples more strongly to the electric field than the light-hole exciton [29].

1.1.3 Photons and Microcavities

Microcavities play a vital role in coupling photons to excitons in the context of forming a polariton. To understand this, we will first look at the quantized light-matter interaction beginning with the photon itself. We can write the second-quantized electric field, $E(\mathbf{x})$, in terms of the photon creation and annihilation operators, $\mathbf{a}^\dagger$ and $\mathbf{a}$, as

$$\mathbf{E}(\mathbf{x}) = \sum_{\mathbf{k}} \sqrt{\frac{\hbar}{2\epsilon_0 V \omega}} (\mathbf{a}_{\mathbf{k}} e^{i\mathbf{k}\cdot\mathbf{x}} - \mathbf{a}_{\mathbf{k}}^\dagger e^{-i\mathbf{k}\cdot\mathbf{x}}). \tag{1.14}$$

Looking at the form of term in the Hamiltonian (1.8) that couples photons to excitons, $-\boldsymbol{\mu} \cdot \mathbf{E}(\mathbf{x})$, where $\mathbf{E} = -\partial \mathbf{A}/\partial t$, we see that the strength of the interaction depends on two things: the dipole moment $\boldsymbol{\mu}$, which is a parameter of the material/exciton, and the electric field. The magnitude of the electric field scales inversely proportional to the square root of the volume. By decreasing the volume of the photon mode, we can significantly increase coupling of the photon to the exciton.

Microcavities, the most popular of which are Fabry-Perot cavities, provide a good way to reduce the mode volume of a range of photon modes. Fabry-Perot cavities are composed of two highly reflecting plane mirrors placed a fixed distance apart. The end mirrors are usually either metallic or Bragg mirrors. Bragg mirrors have an added benefit over metallic mirrors because they can be made to have a reflectivity as high as 99.999% with no absorption. We opted to use the Fabry-Perot cavity with Bragg mirrors for our samples. Fig. 1.3 shows a scanning electron microscope (SEM) picture of the rear Bragg reflector from one of our samples.

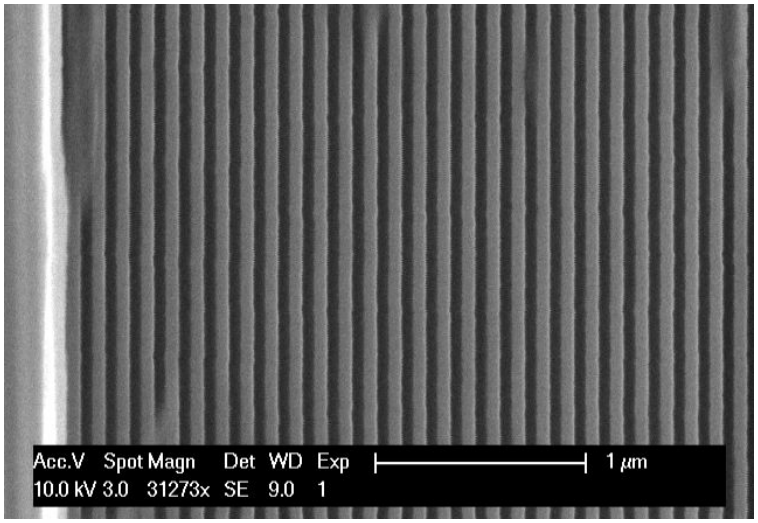

Figure 1.3: Scanning Electron Microscope image of the rear set of Bragg layers in our microcavity structures. The vertical stripes with lighter contrast are the AlAs, while the darker contrast lines are $Al_{0.2}Ga_{0.8}As$.

A schematic representation of how a Bragg reflector works is given in Fig. 1.4a. Essentially, part of the light traveling from n_1 to n_2 is reflected, while another fraction is

transmitted. Since $n_1 > n_2$ the reflected wave does not experience a phase shift. After the wave travels through n_2 a distance of $\frac{1}{4}\lambda$, it is reflected off of the next boundary, this time picking up a 180° phase shift. As it travels back into n_1 the total optical distance it has traveled is $\frac{1}{2}\lambda$ more than the wave that was initially reflected at the n_1-n_2 boundary. This distance plus the 180° phase shift the wave picked up under reflection causes both reflected waves to constructively interfere, enhancing the reflection. This set of layers of two contrasting indices of refraction, each optically $\frac{1}{4}\lambda$ thick, is known as a distributed Bragg reflector (DBR). These reflectors can be stacked to achieve an almost 100% reflection coefficient. The coefficient of reflection is only limited by the smoothness of the boundaries between the layers which is a product of manufacturing quality and the total number of layers. We have already discussed how epitaxial growth methods can make these structures with the precision of an atomic monolayer.

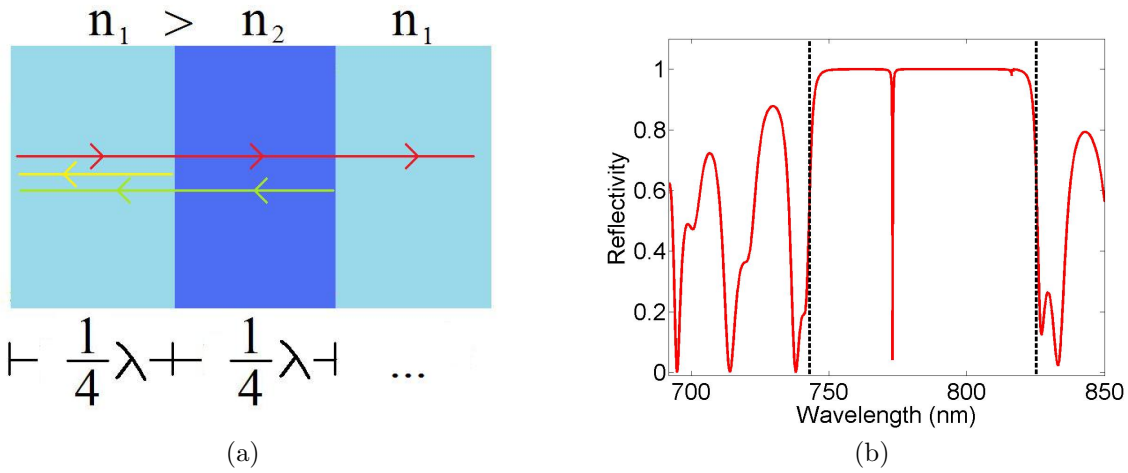

(a) (b)

Figure 1.4: (a) Illustration of how the $\frac{1}{4}\lambda$ Bragg layer creates a highly reflected wave. (b) Calculated reflectivity of two Bragg stacks arranged in a Fabry-Perot geometry. The region between the two vertical dashed lines is known as the stop band. The dip inside the stop band is the cavity resonance.

Figure 1.4b shows how the DBR has a nearly unity reflectivity for a large range of wavelengths. The area between the vertically dashed lines in Fig. 1.4b is known as the stop band, and later will become very important when we consider creating carriers inside the

microcavity.

The dispersion relation for a photon in a Fabry-Perot cavity is

$$E_P(\mathbf{k}_\parallel) = \hbar\omega = \frac{\hbar c}{n}\sqrt{\mathbf{k}_\parallel{}^2 + \mathbf{k}_\perp{}^2}, \tag{1.15}$$

where we have separated the motion of the photon into two directions: the perpendicular direction, in which the mirrors pin the photon mode, and the in-plane direction in which the photon can freely propagate. Because of the confinement of the photon by the mirrors in the perpendicular direction, this equation becomes quite similar to the energy equation for a relativistic massive particle,

$$E(\mathbf{p}) = c\sqrt{\mathbf{p}^2 + m_0^2 c^2}. \tag{1.16}$$

To first approximation we can treat the mirrors as perfectly reflecting, which implies

$$k_\perp = \frac{m\pi}{nL_{\text{eff}}}. \tag{1.17}$$

Here, m is the m^{th} harmonic of the cavity and L_{eff} is the effective optical length of the cavity, which is approximately the distance between Bragg reflectors times the index of refraction. This is approximate because there is an evanescent wave into the Bragg mirrors (true even if perfectly reflecting.) If we insert Eq. (1.17) into Eq. (1.15) and compare this to Eq. (1.16) we can easily extract an expression for the effective mass of the cavity photon:

$$m^* = \frac{n\hbar k_\perp}{c}. \tag{1.18}$$

To maintain a long lifetime for the photon in that cavity, highly reflective mirrors are required. The model of a microcavity system is exactly analogous to the system of a damped harmonic oscillator. The Q factor becomes higher with lower damping/loss and the modes supported by the cavity become spectrally narrower. The Q factor is expressed as

$$Q = \frac{\omega}{\delta\omega} \tag{1.19}$$

where $\delta\omega$ is the spectral full width at half maximum (FWHM) of the cavity resonance and ω is the resonant frequency. The lifetime of a photon in the cavity is then given in terms of the Q factor by

$$\tau_c = \frac{Q}{\omega_c}. \tag{1.20}$$

Physically, Q represents the number of round trips of a photon makes in the cavity during the photon's lifetime. Enhancing the reflectivity of the cavity mirrors increases the Q factor, thereby increasing the lifetime of a photon in the cavity. As will be discussed next, the photon lifetime is the governing factor of the polariton lifetime.

1.1.4 Polariton Properties: The Strong-Coupling Regime

The polaritons studied in these experiments are quasi-two-dimensional in nature, which is due to the fact that both the excitons and the photons have a common axis of confinement, as seen in Fig. 1.5. The excitons are formed inside of finite-barrier quantum wells with relatively high barriers, so that their center-of-mass envelope wave function can be treated as approximately that of the infinite barrier quantum well. The purpose of the quantum wells is to increase the oscillator strength of the exciton and therefore enhance its coupling to light. Two sets of Bragg mirrors arranged in a Fabry-Perot configuration confine the photons along the same direction as the excitons. Of course, polaritons can exist without exciton or photon confinement; however, in these structures the strength of the photon-exciton interaction is greatly increased over that of the bulk material.

The term in the Hamiltonian which couples the photons to the excitons is $-\boldsymbol{\mu} \cdot \mathbf{E}(\mathbf{x})$. Near resonance, i.e. $E_P \approx E_X$, and by invoking the rotating wave approximation, the full second quantized form of the photon-exciton interaction Hamiltonian takes on this form:

$$H = \sum_{\mathbf{k}} E_P(\mathbf{k}) \mathbf{a}_{\mathbf{k}}^\dagger \mathbf{a}_{\mathbf{k}} + \sum_{\mathbf{k}} E_X(\mathbf{k}) \mathbf{X}_{\mathbf{k}}^\dagger \mathbf{X}_{\mathbf{k}} + \sum_{\mathbf{k}} \Omega(\mathbf{k}) (\mathbf{a}_{\mathbf{k}} \mathbf{X}_{\mathbf{k}}^\dagger + \mathbf{X}_{\mathbf{k}} \mathbf{a}_{\mathbf{k}}^\dagger). \tag{1.21}$$

where Ω is the exciton-photon coupling strength. Note that we've neglected terms that don't conserve energy (see the full derivation in Appendix A.3). To a good approximation, when

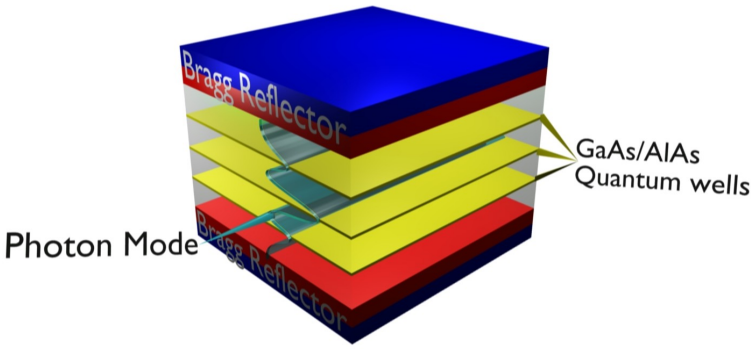

Figure 1.5: Our polariton samples consist of a $3/2\lambda$ planar microcavity and uses DBRs for the cavity mirrors. Three sets of four 70 Å GaAs quantum wells are placed at the antinodes of the optical cavity.

working with relatively small $\mathbf{k}$, we can treat $\Omega(\mathbf{k}) = \Omega$ as constant. When written in the single particle basis, the Hamiltonian becomes

$$H = \begin{pmatrix} E_X(\mathbf{k}) & \Omega \\ \Omega & E_P(\mathbf{k}) \end{pmatrix}. \tag{1.22}$$

While this gives a good single particle picture, it doesn't mean that Eq. (1.21) is necessarily diagonalized in the high density limit, as one expects the same single particle form of the Hamiltonian from the Mollow triplet [30]. However, a Bogoliubov-like transformation allows us to diagonalize the Hamiltonian, Eq. (1.21), as

$$\begin{aligned} \xi^L_{\mathbf{k}} &= \chi(\mathbf{k}) X_{\mathbf{k}} - C(\mathbf{k}) a_{\mathbf{k}} \\ \xi^U_{\mathbf{k}} &= C(\mathbf{k}) X_{\mathbf{k}} + \chi(\mathbf{k}) a_{\mathbf{k}}. \end{aligned} \tag{1.23}$$

This transformation only diagonalizes Eq. (1.21) when the exciton behaves as a boson and $[\mathbf{X}_\nu, \mathbf{X}^\dagger_\mu] = \delta_{\nu,\mu}$. These new operators ξ^U_k and ξ^L_k are known as the polariton destruction operators. The L and U denotes lower or upper polaritons, respectively. It is also important to note that these new creation operators independently satisfy the commutation relation

for bosons is **X** is a boson. These operators create polaritons which become a superposition of both a photon and an exciton state. Under such a transformation, Eq. (1.21) becomes

$$H = \sum_{\mathbf{k}} E_L(\mathbf{k}) \xi_{\mathbf{k}}^{L\dagger} \xi_{\mathbf{k}}^{L} + \sum_{\mathbf{k}} E_U(\mathbf{k}) \xi_{\mathbf{k}}^{U\dagger} \xi_{\mathbf{k}}^{U}. \tag{1.24}$$

An important parameter to introduce is the detuning. It is defined as the difference between the photon energy and the exciton energy:

$$\Delta_{\mathbf{k}} \equiv E_P(\mathbf{k}) - E_X(\mathbf{k}). \tag{1.25}$$

The dispersion relations for the polariton are a function of this detuning parameter as well as the strength of the coupling, Ω, between the exciton and photon. The transformation, Eq. (1.23), that gives us our diagonalized Hamiltonian requires that the new dispersion relations of the upper and lower polariton are

$$E_{\binom{U}{L}} = \frac{E_P(\mathbf{k}) + E_X(\mathbf{k})}{2} \pm \frac{\sqrt{\Delta_{\mathbf{k}}^2 + 4\Omega^2}}{2}. \tag{1.26}$$

$E_P(\mathbf{k})$ is given by Eq. (1.15) and $E_X(\mathbf{k})$ is given by Eq. (1.12). The coefficients $C(\mathbf{k})$ and $\chi(\mathbf{k})$ also become functions of the detuning. These coefficients are known as the Hopfield coefficients [13] and are a measure of the percentage that the polariton branches are photonic and excitonic. These percentages are given by

$$\begin{aligned} |\chi(\mathbf{k})|^2 &= \frac{1}{2}\left(1 - \frac{\Delta_{\mathbf{k}}}{\sqrt{\Delta_{\mathbf{k}}^2 + 4\Omega^2}}\right) \\ |C(\mathbf{k})|^2 &= \frac{1}{2}\left(1 + \frac{\Delta_{\mathbf{k}}}{\sqrt{\Delta_{\mathbf{k}}^2 + 4\Omega^2}}\right). \end{aligned} \tag{1.27}$$

Figure 1.6 shows the calculated polariton states near resonance. This plot shows the level repulsion that one gets from diagonalizing a Hamiltonian like Eq. (1.6). It corresponds to an actual change of the detuning with position on the sample as discussed in section 2.1. Notice that on the negative detuning side of the curve, the lower polariton approaches the energy of the unperturbed photon and behaves as a photon, while on the positive detuning side of the curve the energy approaches the exciton energy and its nature becomes excitonic. At zero detuning, or resonance, the lower polariton becomes a 50%-50% superposition of a photon and an exciton and is energetically shifted exactly Ω below the unperturbed photon

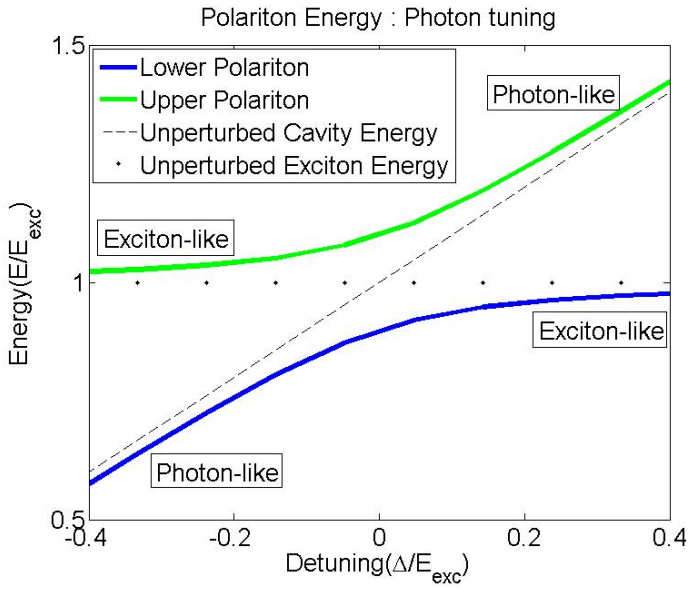

Figure 1.6: Shows the new eigenstates of the strong-coupling Hamiltonian as a function of detuning. The new states are the Lower Polariton (blue line) and the Upper Polariton (green line). Here we are varying the cavity photon energy to change the detuning. At large negative detuning the lower polariton behaves like a photon while the upper polariton behaves as a exciton. At large positive detunings, the upper and lower polaritons swap character. At zero detuning, resonance, both the upper and lower polariton are a 50%-50% mixture of photon and exciton.

and exciton states. This energy splitting at resonance is known as the Rabi splitting. The polariton is said to be in strong coupling when the intrinsic linewidths of the photon and exciton are narrower than the Rabi splitting [31]. For our samples the Rabi splitting is ∼15 meV and the intrinsic linewidths of our photons and excitons are < 1 meV. Our polaritons are therefore in the strong coupling.

Since the photon has a much lighter effective mass than the exciton, about 4 orders of magnitude, the dispersion relation of the exciton can be treated relatively constant. This causes the detuning, $E_P - E_X$, to change drastically and therefore the polariton's character becomes a function of $\mathbf{k}$. Even though the detuning is changing in $\mathbf{k}_\parallel$, the effective mass of the polariton can be calculated near $\mathbf{k}_\parallel = 0$ using

$$m_{\text{eff}} = \frac{\hbar^2}{2\dfrac{\partial E}{\partial(k^2)}}. \tag{1.28}$$

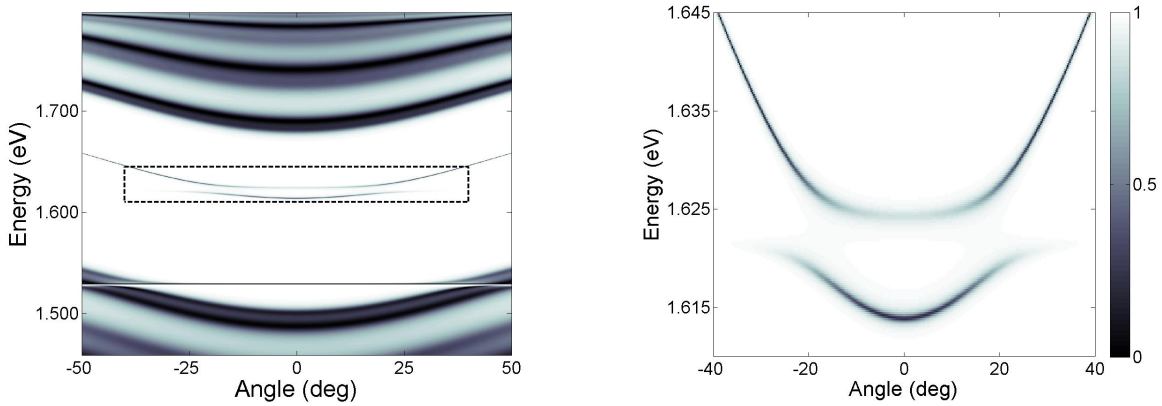

Figure 1.7: (a) shows the calculated reflectivity for the microcavity structures that we used for some of these experiments. The broad region of high reflectivity is known as the stop band. (b) is an expanded view of the boxed in area of (a) and shows the behavior of the polariton as a function of angle (momentum) and energy; i.e. the dispersion relation.

Later on, in Chapter 2, we will discuss how there is a one-to-one mapping of the momentum of a polariton to the emission angle relative to the normal of the sample. This is very

useful for measuring the momentum for a given polariton. Figure 1.7a is a transfer-matrix simulation of the polariton branches as a function of angle (or momentum). Figure 1.7b is strongly, negatively detuned at $k = 0$ so that the resonance is pushed out in momentum space to an angle of $\sim 20°$. A useful fact that can be seen in Fig. 1.7a is that the stop band is also a function of angle. We will exploit this in several different experiments.

Fig. 1.8a shows the measured value of the lower polariton dispersion relation and its effective mass as a function of detuning. Notice that at strong negative detunings it approaches the photon mass and at strong positive detunings, it approaches the exciton mass. In the region we'll typically be working, near zero detuning, the effective mass is about $7 \times 10^{-5} m_e$. We will return to discuss how the data, to compare to the theory, was measured in section 2.2.2.

A tunable effective mass is not the only interesting property of the polariton. The lifetime of the polariton is given by the weighted average of the exciton and photon lifetime:

$$\frac{1}{\tau} = \frac{|\chi|^2}{\tau_X} + \frac{|C|^2}{\tau_P}. \tag{1.29}$$

where χ and C are the Hopfield coefficients discussed above. The lifetimes, τ_X and τ_P, do not include the radiative components of the exciton lifetime since radiative interactions conserve the number of polaritons. The photon lifetime, τ_P, is dictated by the time it takes a photon to escape the cavity. τ_X represents the lifetime it takes for the exciton to recombine through non-radiative processes such as transitions to interband impurity states. The exciton lifetime via nonradiative processes is not very well understood, but it is very long compared to other timescales, and we can treat it as infinite.

Finally, another interesting point to make about polaritons is that we can change the strength of the particle-particle interaction by changing the detuning. As one would imagine, on the photonic side of resonance where lower polaritons take on a mostly photonic nature, they are very weakly interacting. As we tune to the excitonic side of resonance, the cross-section increases until it approaches that of the exciton. A varying cross-section, in combination with a tunable mass and lifetime, gives us a plethora of interesting mechanisms to study the fundamental nature of BEC in these systems.

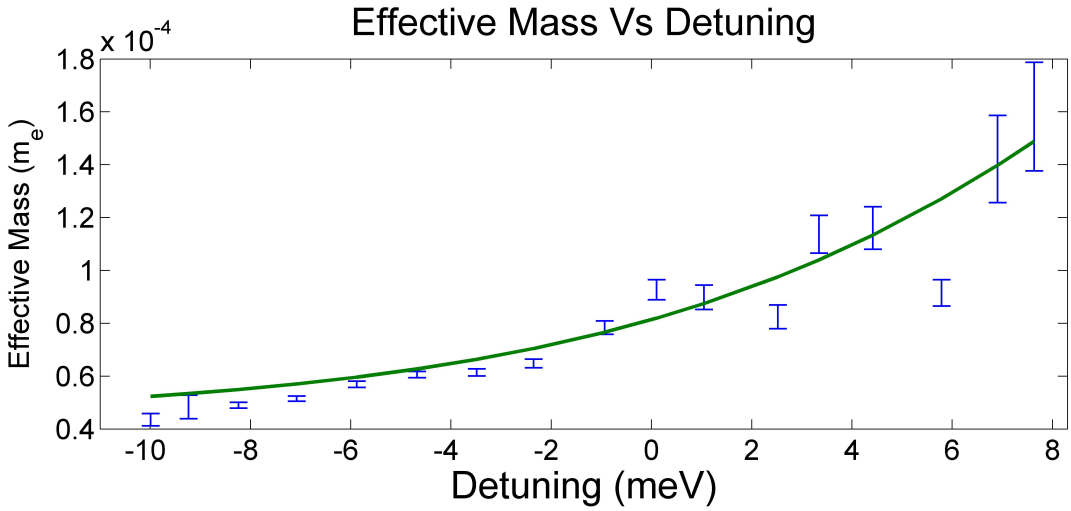

(a)

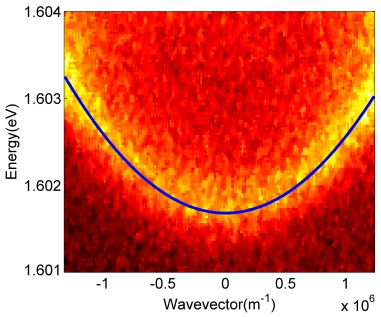

(b) Photonic.

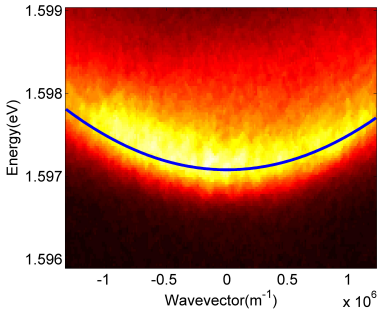

(c) Resonant.

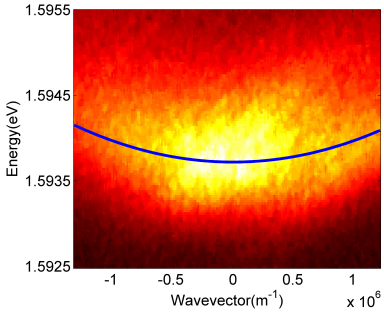

(d) Excitonic.

Figure 1.8: As the detuning of the lower polariton changes, so does the effective mass. (a) shows this effect. The error bars on the data points are the 95% confidence bounds to the fit of a parabola to the measured dispersion data. The solid green curve is a theoretical model with no tuning parameters. (b), (c), (d) are examples of the measured dispersion relation with a fitted parabola showing the deduced effective mass.

1.2 SPONTANEOUS COHERENCE OF POLARITONS

1.2.1 A Quantum Transition

Most basically stated, quantum statistical effects only become relevant when two identical particles have wave functions that spatially overlap and the particles become truly indistinguishable. The simplest quantitative approximation for this condition is to equate a particle's DeBroglie wavelength, λ, with the interparticle spacing. If we have a 2D thermal ensemble then the DeBroglie wavelength is approximately

$$n_c^{-1/2} \approx \lambda = \frac{h}{p} = \frac{h}{\sqrt{2mk_BT_c}}, \tag{1.30}$$

where h is Planck's constant, m is the particle's mass, k_B is Boltzmann's constant, n is the density, and T is the temperature. Rearranging,

$$T_c = \frac{n_c h^2}{2mk_B}. \tag{1.31}$$

This simple calculation gives a hint about the regime in which quantum effects start to change the nature of the ensemble. With a polariton mass of about $7 \times 10^{-5} m_e$ and a temperature of $\sim$10 K, we calculate an estimated density of 2×10^3 cm^{-2} polaritons to observe polaritons in the quantum regime. The temperatures and densities that we need to observe the onset of quantum statistical effects are readily achievable in a semiconductor microcavity sample. Amazingly, even in room-temperature experiments at $T \approx 292$ K, polaritons have critical densities low enough to see the onset this quantum transition [32]. This is due to the extremely light mass of the polariton.

1.2.2 Bose-Einstein Condensation

One of the most complete and encompassing definitions of BEC was given by Penrose and Onsager [33]. Here I will follow the review of A.J. Leggett [34]. We begin by considering the second-quantized single-particle density matrix, defined as

$$\rho(\mathbf{x}, \mathbf{x}') = \langle \psi^\dagger(\mathbf{x})\psi(\mathbf{x}')\rangle. \tag{1.32}$$

We know that, since $\rho(\mathbf{x}, \mathbf{x}')$ is Hermitian, it is diagonalizable in some basis, with the general decomposition

$$\rho(\mathbf{x}, \mathbf{x}') = \sum_i n_i \chi_i^*(\mathbf{x})\chi_i(\mathbf{x}'). \tag{1.33}$$

In the weakly interacting case, $\chi_i(\mathbf{x})$ would represent the single particle eigenstates; however as the particle-particle interactions are included, this need not be the case. We can then define three cases in terms of these eigenstates:

1. If all of the eigenvalues, n_i, are of order unity, then the ensemble of particles is said to be normal, or not Bose-condensed.
2. If there is one eigenvalue of order N, where N is the total number of particles in the system, and the rest are of order unity, then the ensemble of particles is said exhibit simple BEC.
3. If there are two or more states with the eigenvalue of order N, then the state is one of a fragmented BEC.

The ansatz first used by Bogoliubov is that the field operator for a single massively occupied state $\mathbf{k} = a$, otherwise known as simple BEC, can be treated approximately as [35]

$$\Psi(\mathbf{x}) = \sqrt{n_a} e^{i\mathbf{a}\cdot\mathbf{x}} + \sum_{k\neq a} e^{i\mathbf{k}\cdot\mathbf{x}} \mathbf{a}_k, \tag{1.34}$$

where we've explicitly replaced the $\hat{\mathbf{a}}_a$ operator with the c-number $\sqrt{n_a}$. This field operator gives rise to the term Off Diagonal Long Range Order (ODLRO) [36] as seen in the density matrix. To see this, we can look at Eq. (1.32) with Eq. (1.34) inserted for the field operator:

$$\rho(\mathbf{x}, \mathbf{x}') = n_a e^{i\mathbf{a}\cdot(\mathbf{x}-\mathbf{x}')} + \sum_{k\neq a} \langle \Psi_k(\mathbf{x})\Psi_k^\dagger(\mathbf{x}')\rangle. \tag{1.35}$$

While the term with the sum is an incoherent superposition of Maxwellian-like particles, for which correlations only exist over short ranges, the first term is nonzero even as $|\mathbf{x} - \mathbf{x}'|$ approaches infinity. This situation is known as OLDRO [34]. The off-diagonal elements of $\rho(\mathbf{x}, \mathbf{x}')$, i.e. $\mathbf{x} \neq \mathbf{x}'$, do not go to zero as they do for a gas above T_c, the critical temperature. I will use the words "coherence" and OLDRO synonymously.

In a two-dimensional ideal gas with uniform potential, the density of states actually makes BEC unfavorable. Since we are dealing with a weakly interacting system of particles, it is straightforward to show that the chemical potential μ is always negative except at $T = 0$ where it becomes zero, which means that the ground state has a large, but not macroscopic occupation number (simply given by Bose statistics: $(e^{\beta(\epsilon-\mu)} - 1)^{-1}$, where $\epsilon = 0$ for the ground state.) Explicitly, μ takes the form

$$\mu = k_B T \ln\left(1 - e^{-\frac{2\pi\hbar^2 n}{m k_B T}}\right). \tag{1.36}$$

This raises the question as to whether or not it is truly possible to see BEC in 2D. There is a 2D phase transition known as the Kosterlitz-Thouless transition [37] in which domains of coherence appear, but there is no formation of ODLRO. However, one can change the density of states of the system by applying a trap, and in the case of a harmonic potential in the limit of large volume, the conditions on condensation become identical to those of the 3D case [38]. It may be argued that the trap strictly forbids us from taking the thermodynamic limit, but this argument is unreasonable since one can never truly take the thermodynamic limit of any real system, including a BEC of cold atoms.

1.2.3 Superfluidity and Vortices

Assuming that it is possible to write the ground state wave function as we did in Eq. (1.34), then the more general form $\psi_0(\mathbf{x}) = \sqrt{n_0} e^{i\theta(\mathbf{x})}$,where n_0 is the condensate density, can be used for the macroscopic state. This is known as the order parameter and is generally responsible for superfluid motion. If we can write the many-body wave function in such a way then, using the definition of current density, the superflow has an associated velocity

$$\mathbf{v_s} = \frac{\hbar}{m} \nabla\theta. \tag{1.37}$$

Hence, we say that the flow is a potential flow because the curl of the velocity field is zero, i.e.,

$$\nabla \times \mathbf{v_s} = 0. \tag{1.38}$$

If the wave function is to be continuous and differentiable, that implies that the phase change around a closed loop must be an integer value of 2π. If $\Delta\theta$ (the phase difference around a closed loop in space) is not zero, the amplitude of the superfluid wave function must be zero at the center of the vortex to avoid the unphysical aspect of having infinite angular momentum. These quantized radii are too small to physically observe in most cases involving superfluid polaritons. Instead, a technique using an interferogram method, as illustrated in Fig. 1.9, can be employed. In such experiments we can look for fork-like dislocations in the interferogram to measure the presence of vortices [39].

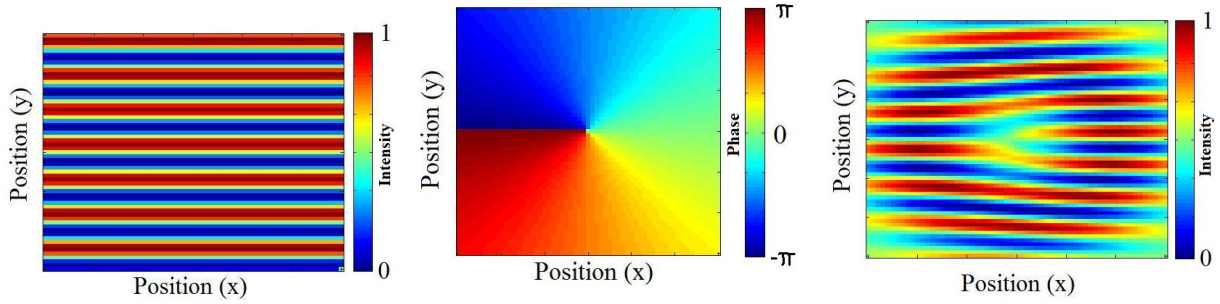

(a) Planewave interferogram (b) Phase twist (c) Interferogram of a Vortex

Figure 1.9: (a) shows what a normal interferogram looks like for two plane coherent waves. If one of the images being interfered has a vortex, then there is an associated phase twist as in (b). (c) is an interferogram when one of the images has a vortex. Notice the fork-like dislocation that arises in the interferogram at the center of the vortex.

2.0 EXPERIMENTAL METHODS

This chapter is designed to introduce non-experimentalists to the optical techniques used in these experiments. With the exception of this section and Sections 2.1 and 2.2.2, it can be skimmed over by those generally knowledgeable in optical experiments.

There are three main experimental design stages to take into account when configuring experiments on polaritons:

1. **Creating Polaritons:** Creating polaritons for the purpose of detecting the spontaneous formation of coherence can be done by two means: electronic carrier injection [40] or optical excitation. Because of the Bragg reflectors on either side of the cavity, electronic injection is hardly feasible since the layers of these reflectors act as barriers, preventing carriers from entering the cavity; in turn, this prevents the formation of any significant population of polaritons. Instead, for these experiments we rely on optically exciting carriers directly inside the cavity.

   Optically exciting carriers is not without challenges. It is difficult to generate polaritons by this method because the cavity is surrounded by highly reflective mirrors. To do so requires either pumping the sample directly at the energy of the polariton branch, i.e., resonantly, or pumping the higher-energy edge of the stop band where the mirrors have low reflectivity. When probing for spontaneous formation of coherence, resonant pumping is not desired since the polariton gas is already imprinted with the coherence of the excitation source (usually a laser). We typically opt for non-resonant excitation so that residual coherence from the source will be lost when the carriers scatter among themselves and with lattice phonons while cooling down to the polariton energy.

   Figure 1.4b shows the calculated reflectivity spectrum for the microcavity structure,

which has been verified experimentally for several angles of incidence. The broad region with nearly unity reflectivity is the stop band. The quantum-well exciton and cavity resonance must be designed to fall in this range of energy. For incoherent excitation, we use an excitation wavelength at one of the dips in reflectivity at short wavelength (high photon energy). This generates hot electrons and holes which then fall into the exciton and polariton states by phonon emission. We used a stabilized diode laser or a Ti:Sapph oscillator for the excitation.

2. **Manipulating Polaritons:** One of the interesting parameters to vary in polariton experiments is the detuning (see Eq. (1.25)). By changing the detuning, one can change many parameters of the polariton, such as the lifetime, scattering cross-section, and effective mass; although, not all of these parameters can be changed independent of one another. All of these parameters play an important role in the thermalization and the formation of coherence. No other experiments in the field of BEC, including atomic condensates, can claim the ability to tune all of these parameters. The next section (2.1) will discuss one of the methods we use to change the detuning.

   The density of the polaritons is a function of the number of carriers that can be produced inside of the cavity. Often, this is limited by the maximum power of the excitation laser. There is however, a limit for the maximum excitation density when the valence band of the semiconductor becomes depleted. This is known as phase-space filling. When this happens, the medium becomes optically transparent, preventing the formation of additional polaritons. Also, exciton screening effects at high density can prevent the formation of excitons.

   These experiments are performed inside of a cryostat, allowing the temperature of the sample to be controlled. The temperature of the sample is not a direct measurement of the polariton ensemble though, since polaritons typically only undergo a few phonon scattering events over the course of their lifetime. Although in the new long-lifetime samples discussed in Chapter 4 the particles can scatter many more times.

3. **Measuring Polaritons:** When measurements are made on polaritons, they are made by detecting the annihilation of the polariton by means of a photon escaping the microcavity. Conveniently, many parameters of the polariton gas are preserved in the information

carried off by this photon. The energy of the polariton is conserved under the creation of this external photon so that we may use a spectrometer to measure the polariton's energy. The in-plane momentum is also conserved [41] (for a more in depth discussion see Section 2.2.2). Finally, the phase coherence of the polariton's wave function is maintained in the escaping photons, making it possible to easily measure first- and second-order coherence correlation functions of the ensemble.

2.1 SAMPLES AND DESIGN

The microcavity samples used in these experiments were designed using an optical transfer matrix simulation (see, eg., Ref. [42]) with material parameters taken from Ref. [43]. The samples were grown by Loren Pfeiffer and Kenneth West at Princeton using molecular beam epitaxy (MBE) with the precision of a single atomic layer. They consist of two components: the microcavity and several sets of quantum wells. GaAs/AlAs alloys were chosen because these two materials have the same lattice symmetry and approximately the same lattice spacing. The lattice spacing is relevant because a difference in this quantity will generate strain at the interface between these two materials. During the growth, this strain can propagate through the structure [44] and grow into dislocations which inhibit the mobility of polaritons and destroy the quality of the DBRs, as mentioned earlier, DBR stands for distributed Bragg reflector.

The mirrors and spacer layers of the cavity need to be fashioned from a material which is transparent to light at the polariton wavelength. This prevents unnecessary absorption which would heat the sample and lower the overall lifetime of the polaritons. The DBRs in the mirrors and the majority of the cavity are composed of $Al_{0.2}Ga_{0.8}As$ and AlAs. $Al_{0.2}Ga_{0.8}As$ has a bandgap equating to roughly 690 nm making it transparent to longer wavelengths. AlAs has an even higher bandgap than $Al_{0.2}Ga_{0.8}As$. The distance between the two mirrors was chosen to be resonant with the quantum-well exciton energy. The $n = 3$ mode of the cavity was used to meet this criteria while still leaving a significant volume to include the quantum wells.

With a 61 Å width, the GaAs quantum wells have excitons in the lowest confined state with an energy corresponding to ∼770 nm optical wavelength. Four quantum wells were placed at each of the three antinodes of the cavity where the electric field is strongest in order to enhance the exciton-photon coupling, since the coupling strength of excitons to the photon field goes as $-\boldsymbol{\mu} \cdot \mathbf{E}$. The quantum wells are so narrow when compared to the wavelength of light that four quantum wells could be placed at each of the antinodes without a significant variation of electric field over the wells.

In the quest to achieve a long polariton lifetime in conjunction with long diffusion lengths, two different samples were produced. The first sample was produced to maximize sample quality by limiting the number of layers in the DBRs (16 layers in the front and 20 in the rear). Each additional layer of material adds additional strain because AlAs and GaAs have a slightly different lattice constants. Beyond that, longer growth times introduce more impurities into the sample through unavoidable contamination inside of the growth chamber. Because there were fewer DBRs in the mirrors, the reflectivity of the mirrors was such that polariton lifetime at resonance was 4 ps.

The second sample that we designed was precisely the same as the previous sample with the exception that the number of layers in both the front and rear DBRs was doubled (32 layers in the front and 40 layers in the rear). This sample required more than 30 hours of continuous growth time. Over this length of time, growth rates of the different materials varied about 2% adding an additional disorder to the sample. The performance of these samples still greatly exceeded the above-mentioned samples and achieved a polariton lifetime of ∼100-300 ps, as will be discussed in several later Section 5.1.

Because these samples were grown using MBE techniques, they include important features from the growth process. One of the most valuable features is that the rate of growth of material is not constant across the diameter of the substrate wafer. This causes a radial variation in thickness, transitioning from thicker toward the center of the wafer to thinner near the edge. This gives the option to continuously vary the detuning (defined in Section 1.1.4) simply by spatially scanning across the sample. Since the cavity's energy changes $\propto 1/L$, and the exciton's square-well confinement energy changes much less rapidly as $E_{\text{gap}} + \text{const.}/L^2$, the detuning (1.25) varies across the sample; that produces a lower polariton which is more

exciton-like toward the center of the wafer and more photon-like toward the outer edge of the wafer.

2.2 OPTICAL SETUPS

2.2.1 Real Space Imaging

Real-space imaging of the polariton gas is usually done with one small numerical aperture (NA) lens as in Fig. 2.1. The magnification of the imaging setup is chosen such that the spatial features of the polariton gas map roughly to the size of the Charged Coupled Device (CCD) chip that is used to detect the light. If spectral resolution is desired, the image may be formed on the entrance slit of a spectrometer, taking care not to exceed the f-number of the spectrometer. The spectrometer will throw away one axis of spatial information, trading it instead for energy resolution.

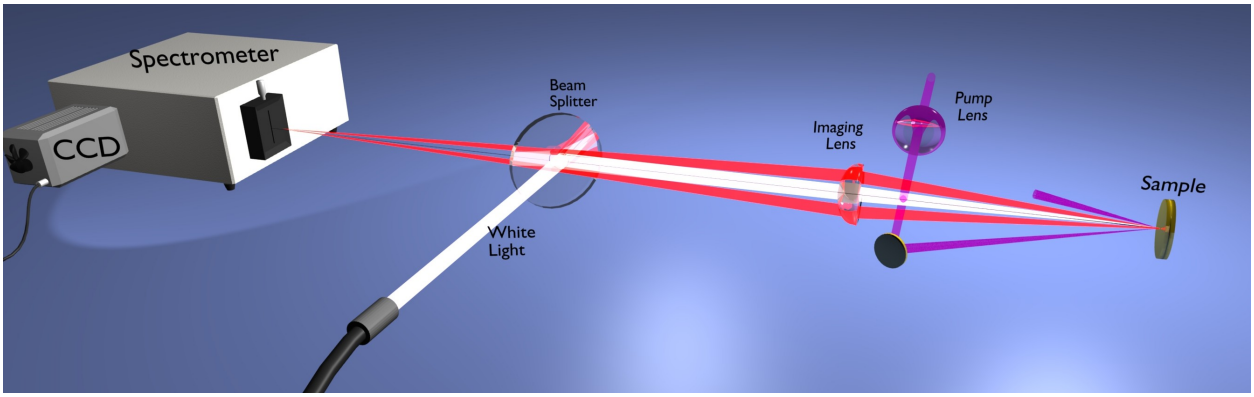

Figure 2.1: Real-space imaging detection system used for white-light reflectivity and PL measurements on polaritons.

There are generally two types of imaging methods we use to resolve the polariton: photoluminescence (PL) and white-light reflectivity. PL requires that we excite the sample and and measure the emission from that state through processes that emit photons. This light is then spectrally filtered and imaged onto a CCD. PL measurements are used when a high

density of polaritons are excited. The other method, white-light reflectivity, is used to measure the single particle spectrum of polaritons. It requires a spectrally broad, incoherent light source to be bounced off of the sample, usually at normal incidence. The state being measured will absorb a section of the white light such that, when the reflected light is imaged onto a spectrometer, the absorbed portion of light corresponds to the actual state. Since this absorption can be rather small, few polaritons are created, and it allows us to roughly determine the single particle energy states. The white light is first filtered through a long-pass filter to prevent any absorption by the frequency components above the stop band. This prevents an occupation of the polariton state which would emit PL and change the reflectivity signal.

2.2.2 Momentum Space Imaging

The far-field angular distribution of the PL from the sample gives the momentum distribution of the polaritons, since the generalized Snell's law requires that the in-plane momentum of the polaritons be conserved when they convert to photons outside the system. This in-plane momentum maps to the angle of photon emission in the Fraunhofer far-field limit. The higher the in-plane momentum of the polariton is when it decays, the larger the angle of emission of a photon will be relative to the normal of the sample. If we measure the intensity, $I(\theta)$, and energy, $E(\theta)$, we find all the information about the occupation and density of states $N(\mathbf{k})$ such that we can determine the thermodynamic state.

2.2.2.1 Diffuser Plate Method If a diffuser plate (frosted glass) is placed in the far field of the emission from a polariton sample, the plate acts as a screen. The criteria for locating the far field in this case is to place the diffuser plate a distance away from the polariton sample which is much longer than the size of the polariton gas. This screen is then imaged onto a CCD or CCD/spectrometer combination with a lens giving information about intensity vs energy vs momentum or intensity vs x-momentum vs y-momentum. Figure 2.3 is an example of such a setup.

In image coordinates, the position along the diffuser then corresponds to the angle that

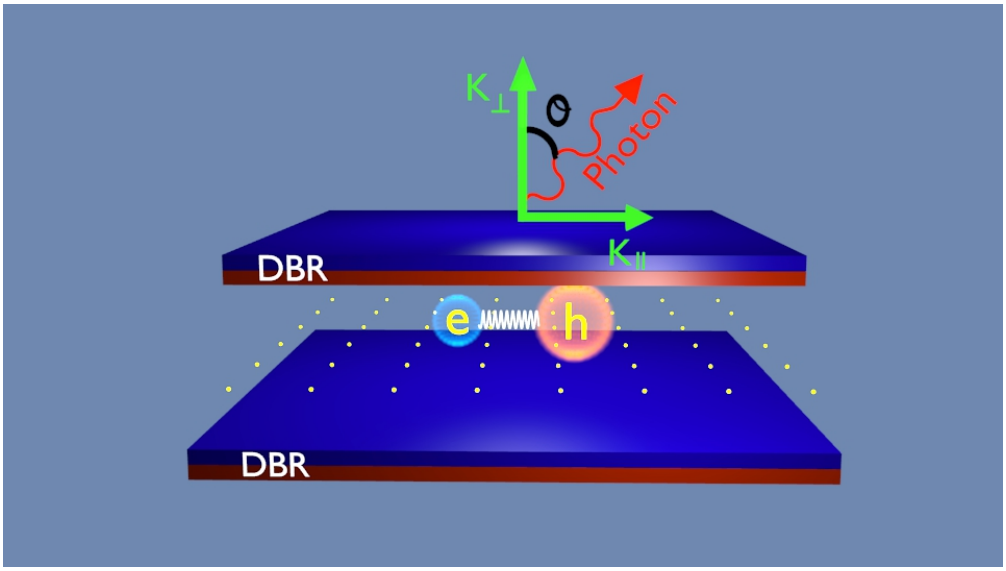

Figure 2.2: When a polariton decays, a photon is emitted from the cavity. The emission conserves both energy and in-plane momentum. By measuring the intensity (number of photons) of the emission as a function of energy and angle, we can determine the thermal state.

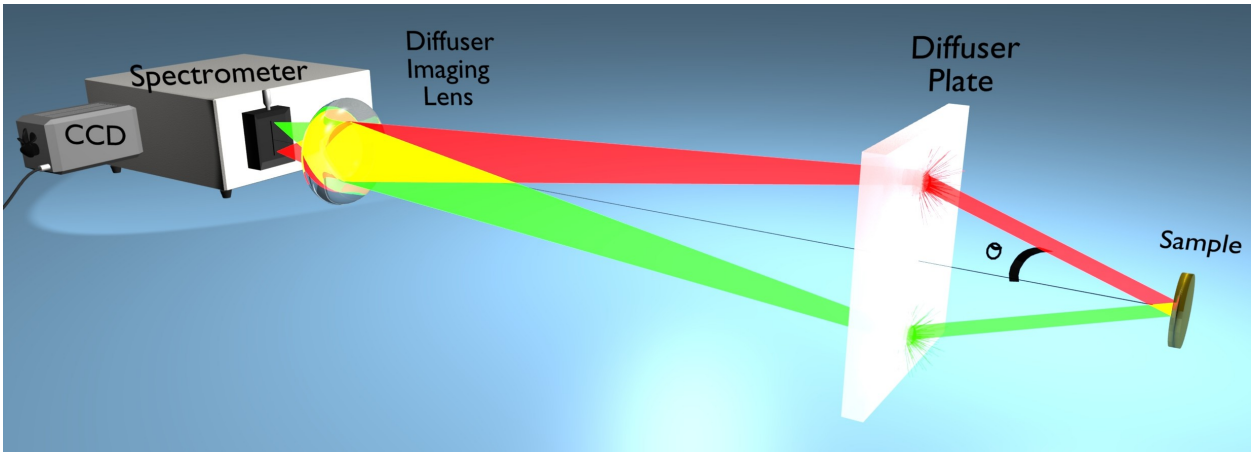

Figure 2.3: A setup using a diffuser plate to measure information about momentum space. The diffuser plate maps angle to position by scattering light creating a new object to image onto a spectrometer.

the light was emitted. By knowing the distance the diffuser plate is way from the source, the angle as a function of position is known. The diffuser creates problems, however, when the emitted light intensity is low. This is because the ideal diffuser scatters light into 4π steradians, and not all of that light is collected by the lens; hence the observed signal is very weak. Also, interference from the rough surface causes "speckle" with an uneven patter. This can in principle be removed by averaging over several plate positions. The angular resolution of this method is also limited

2.2.2.2 Fourier Imaging Lenses Instead of the diffuser plate system, we usually opted to use a lens system to project the far-field emission onto the entrance slit of a spectrometer. This allows either energy vs. momentum images as direct data in first-order transmission through the spectrometer, or 2D momentum-space images in zero-order transmission through the spectrometer. This system is very fast since all momentum-space data is taken in parallel by the CCD camera. Figure 2.4 shows how this is done optically.

The $k = 0$ point of the angle-resolved luminescence measurements was found by bouncing a laser from the surface of the sample to find the angle which gave exact retroreflection. This method had an uncertainty of $\pm 10^3$ cm^{-1}, or about 0.2°. The $E(k)$ dispersion of the polaritons at low density is known from the Rabi splitting; this was checked in many previous calibrations of k-space data. The mapping of the measured angle to $k_\parallel$ in cm^{-1} could therefore be done using a fit of this dispersion relation to the low-density angle-resolved data. This mapping was also checked by a physical measurement of the angle of the rays using an adjustable iris.

2.3 STABILIZED LASER DIODE

The Titanium:Sapphire (Ti:Sapph) oscillator usually is the laser of choice for optically exciting polaritons because of its versatility in wavelength-tuning range and high output power. However, fluctuations in pump intensity manifest themselves as fluctuations in polariton density. Ti:Sapph lasers are notorious for mode hopping and the consequent intensity fluc-

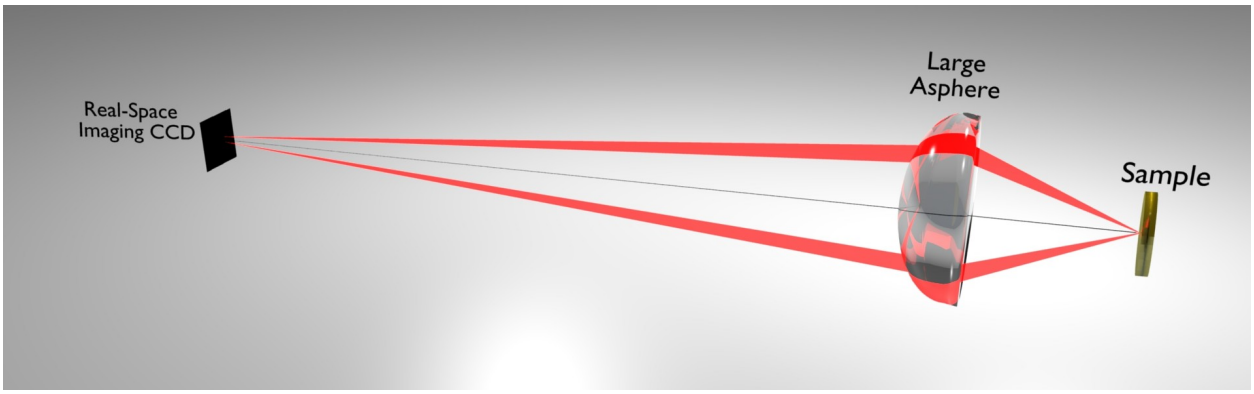

(a)

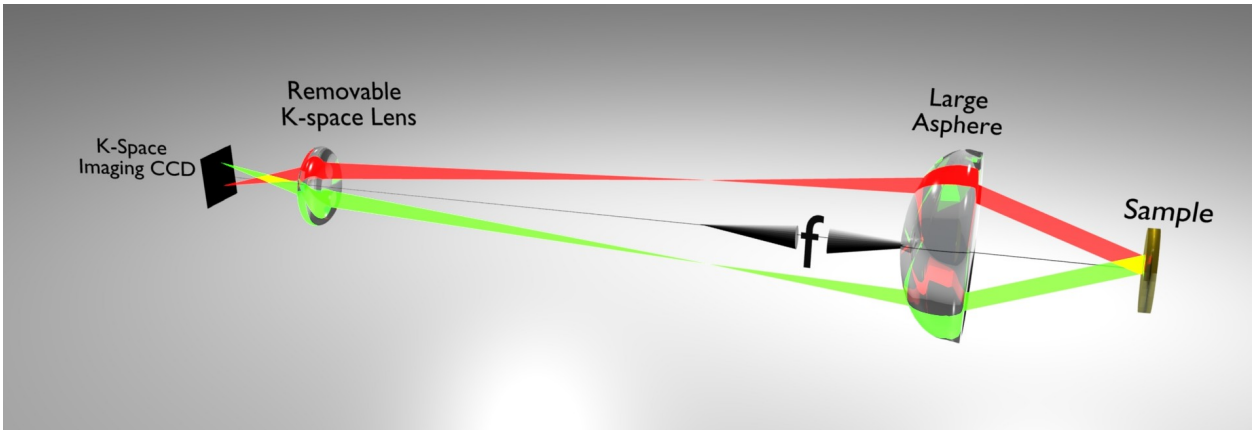

(b)

Figure 2.4: Depiction of an optical setup used to measure 2D momentum space and real space. The removable lens seen in 2.4b is used to switch between real-space imaging and k-space imaging. In the momentum-space setup, the removable lens is imaging the Fourier plane of the large asphere onto the CCD. The large asphere is used because we want to maintain a large N.A. while still maintaining a large working distance and minimizing spherical aberrations. This is because the sample is placed inside of a cryostat with a long working distance.

tuations, which arise from the nature of the cavity geometry and gain medium. If these temporal fluctuations are short compared to the time necessary to make a measurement, the density dependent interaction of polaritons tends to wash out important indicators of Bose-Einstein Condensation, such as spectral narrowing and coherence time [45]. A different type of pump laser is therefore desirable and a grating-stabilized laser diode was chosen to replace the Ti:Sapph laser. This system itself also has drawbacks such as limited wavelength-range tunability and low output power.

A typical experiment involves exciting the sample at an energy just above the edge of the stop band (defined in Section 1.1.3) of the Bragg reflector where there is a dip in the reflectivity. This allows for maximum light transmission and absorption by the quantum wells inside of the microcavity, as well as a decoherence of the hot carriers as they cool down to become polaritons. For a laser FWHM spot size of 20 μm, a threshold power of 30 mW is necessary for BEC (see Chapter 3.3). Only one type of diode laser is commercially available that has a wavelength range near this desired wavelength and also with enough power to reach this critical density, namely the OptNext^{TM} brand with a operating wavelength of 705 nm.

Figure 2.5 is a schematic for the frequency-stabilized system we used. In this setup, the laser diode itself is a laser cavity. When the cavity lases, its emission impinges on a grating that is positioned directly in front of this output. The grating, blazed for the particular wavelength of the laser and arranged in a Litrow configuration [42] for maximum efficiency, has a first-order diffraction peak that reflects back into the laser diode. This essentially creates an extended cavity where the wavelength-resolved light that is fed back into the laser diode is reamplified, creating a frequency-stabilized cavity. Since gratings (even blazed ones) never couple 100% of the incident light into the first order, the zeroth order light, or reflected light, from the grating is now the output coupler of the extended cavity. The laser diode also has an internal photodiode that senses the output power of the laser. If this power deviates from the setpoint, an external controller modulates the laser-diode input current to restore the setpoint output intensity. In this way the diode is both intensity- and frequency-stabilized. The temperature of the cavity is maintained by means of a Peltier cooler which can also be used to temperature-tune the output wavelength of the diode laser

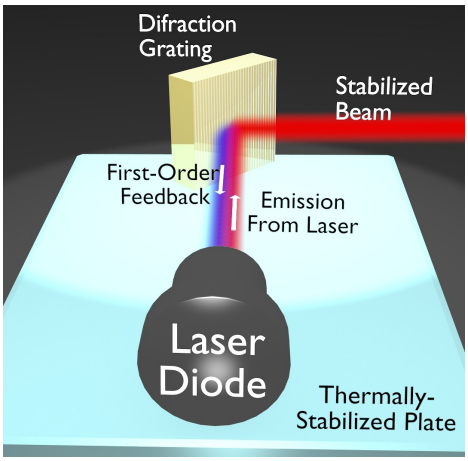

Figure 2.5: Frequency-stabilized laser diode in a Litrow configuration. The emission from a laser diode is spectrally resolved by a diffraction grating, in a Litrow arrangement, and fed directly back into the diode, effectively extending the cavity of the laser while also selecting a single mode of the laser. A percentage of the light is coupled out of the extended cavity by means of the zero-order grating reflection.

by approximately ± 5 nm.

2.4 TIME-RESOLVED EXPERIMENTS

Time-resolved experiments of polaritons are limited to time scales on the order of the polariton or exciton lifetime. With the lifetime of polaritons typically being about 10 ps and the phonon scattering time being approximately the same, one must be able to resolve events less than, or on the order of these scales. Pump-probe measurements provide a resolution of 10 fs but are hard to implement because the spectral width required to achieve such a temporal resolution is about 2 orders of magnitude wider than the spectral width of the polariton. Hence, we used a device known as a streak camera to provide information on the polaritons in the time domain.

The relevant components of the streak camera are pictured in Fig. 2.6. Photons emitted

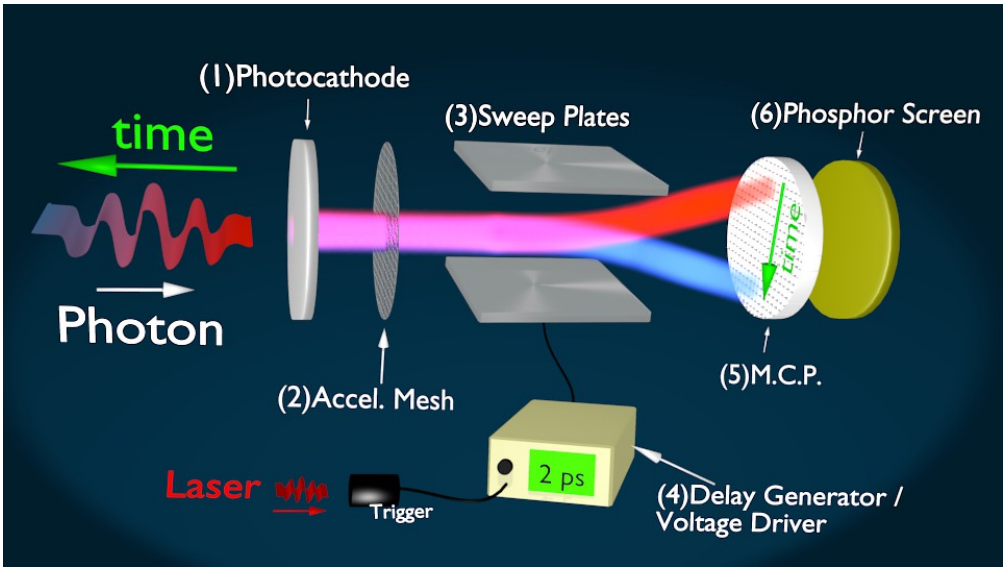

Figure 2.6: A depiction of the components of the streak camera. The resulting information is a time-resolved image in which one axis of spatial information is transformed into temporal information. The streak camera has a resolution of up to 2 ps. The remaining axis may represent position, momentum, or energy.

from the polariton gas are either directly imaged onto the photocathode, or are first spectrally resolved with a spectrometer and then imaged onto the photocathode. In the figure, the photon and electron beams are colored; a red color represents an event which happens at an earlier time, while a blue color represents events which happen later. The photocathode is biased with a high voltage such that one photon can eject one electron with a quantum efficiency of approximately 60%. These electrons are then accelerated by a wire mesh through a large, positive potential. Afterwords, the electrons pass through the sweep plates. These plates are biased with a 2 kV time-varying potential, inducing an large electric field in between these two plates. The electrons are accelerated in the vertical direction by varying amounts. The signal to the sweep plates is controlled by a delay generator which uses the excitation laser as a clock ($\sim$76 MHz) to synchronize events on the streak camera with polariton events. Once the electron beam passes through the sweep plates, they strike a micro-channel plate (MCP). The purpose of the MCP is to intensify the electron beam, without losing spatial resolution. The MCP has a voltage bias just like the photocathode except it has hundreds of small channels to guide the electrons as they cascade to the other side. On the other side of the MCP, these amplified electron beams strike a phosphor screen, exciting it and causing it to luminescence. The phosphor luminescence can then be imaged onto a CCD where the final image is acquired. The vertical axis of the image represents events in time, while the horizontal axis either contains spatial information or spectral information, depending on whether or not a spectrometer was placed in front of the photocathode.

3.0 STRESS TRAPPING OF POLARITONS

Our experiments have shown several effects indicative of Bose-Einstein condensation in polaritons in GaAs-based microcavity structures when a harmonic potential trap for the two-dimensional polaritons is created by applied stress [1]. These effects include both real-space and momentum-space narrowing, first-order coherence, and onset of linear polarization of the PL above a particle density threshold. Similar effects have been seen in systems without traps, raising the question of how important the role of the trap is in these experiments. In this chapter I present results for both trapped conditions and resonant untrapped conditions in the same sample. I find that the results are qualitatively different, with two distinct types of transitions [10]. At low density in the trap, the polaritons remain in the strong-coupling regime while going through the threshold for onset of coherence; at higher density, there is a different threshold behavior which occurs with weak coupling which can be identified with lasing; this transition occurs both with and without a trap [11].

One question that arises is, "how effective is the trap at confining polaritons that have a short lifetime?" By using stress under the right conditions, it is possible to create an asymmetric trap for polaritons; one which is harmonic in both dimension, but cigar-shaped and similar to those used in certain atomic condensates experiments [46]. If the polariton truly forms a condensate in the ground state of the trap, then the momentum distribution should go from one which is rotationally symmetric when the particles behave as a classical gas and there is no BEC, to one which exhibits the symmetry as the ground state of the trap [46]. We investigate this phenomenon and report preliminary results which confirm this effect.

As a secondary effect of applying the stress trap, the effect of electron-hole exchange is enhanced in polariton states. We find an energy splitting of the lower polariton to be over 700

μeV due to the exchange effect, which is almost an order of magnitude larger than splittings previously measured in quantum dots and quantum wells [47, 48]. These measurements of exchange are unique because the exchange energy splitting is much greater than the narrow linewidths of our polaritons.

3.1 CREATING THE STRESS TRAP

In many of the polariton experiments that we have performed, a stress trap was applied to the sample. Figure 3.1a is an example of the stressing configuration that we have used to create such a trap. A pin was used to apply pressure to the back of the sample. While the sample is clamped around the edges, the bottom of the sample is unconstrained. This condition allows the portion of the sample directly underneath the pin to change the crystal symmetry similar to the uniaxial stress, shown in Fig. 3.1b. As will be discussed below, the hydrostatic shift of the conduction band ($-a_c(\epsilon_{xx} + \epsilon_{yy} + \epsilon_{zz})$ or $-a_c\delta V$) is largely the dominant mechanism which changes the exciton's energy. Therefore, if the applied stress increases the overall volume of the crystal, the energy is lowered. Although, as illustrated in Fig. 3.1b, the volume of a unit cell is reduced by the compression along the direction of the applied uniaxial stress, the free expansion of the unit cell in the perpendicular direction can compensate for this, producing an overall expansion of the cell.

The microcavity sample is typically grown on a GaAs substrate which is approximately 500 μm thick. In order to create a reasonably sized trap for polariton confinement, we first must etch this substrate to roughly 125 μm thick. A rule of thumb deduced from numerical simulations and a few experiments is that the FWHM of the trap is roughly equivalent to the thickness of the sample [49]. While making the sample thinner than 125 μm would in general create a more useful trap, the sample becomes exceedingly difficult to manipulate and handle.

To create a stress-trap minimum, a pin is used to apply pressure to the substrate side of the sample. The tip of the pin's point has a diameter of roughly 50 μm. Varying forces, of the order of magnitude of $\sim$1 N, are applied to the pin in order to deflect the sample. The

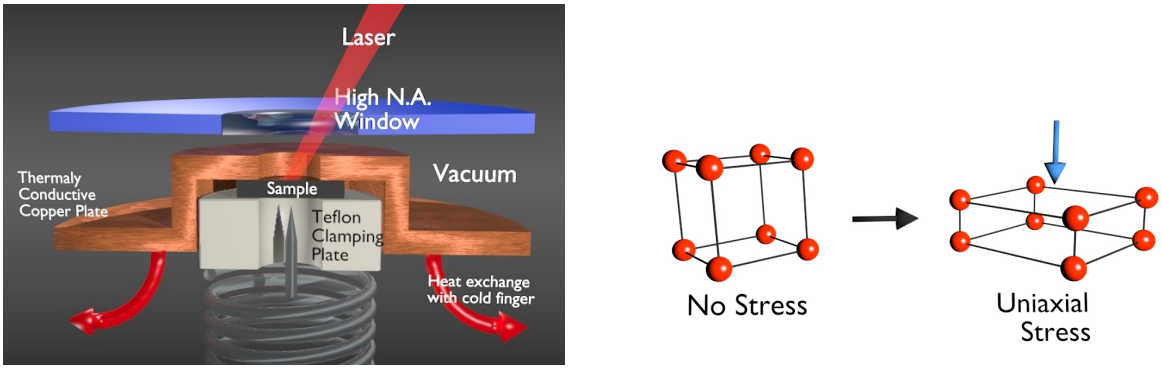

(a) (b)

Figure 3.1: (a)Example of a stressing apparatus used to apply stress to our samples. This was configured for a microscope cryostat with a high NA in order to collect data for a large range of momentum. (b)Cartoon image of how a uniaxial stress changes the crystal geometry and thereby changes the Bloch functions.

magnitude of this force depends on the thickness of the sample and the depth of the trap that is desired. A pictorial version of the boundary conditions used is shown in Fig. 3.2. If the bottom of the sample were constrained for no motion, unlike 3.2b, then the strain would create an anti-trap due to an overall hydrostatic compression of the lattice [50].

Using the boundary conditions shown in Fig. 3.2, a steady-state solution for strain can be calculated. The Christoffel wave equation, which models strain dynamics in solid-state media is:

$$\rho \ddot{u}_i(\mathbf{x}) = f_i + \sum_{jlm} C_{ijlm} \frac{\partial u_l}{\partial x_j \partial x_m}, \tag{3.1}$$

where ρ is the mass density, f_i are body forces, including those at the boundaries, C_{ijlm} is known as the compliance tensor and is the 3D, volume-normalized version of the spring constant in Hooke's law, u_l is the displacement of the crystal with respect to a particular direction, and x_j represents the physical dimensions of space. This equation was numerically solved under the boundary conditions in Fig. 3.2 by iterating forward in time, beginning from an unstrained state, and including a damping, dissipative term. Even though our samples are a complex structure of GaAs, AlGaAs and AlAs, all three materials share approximately

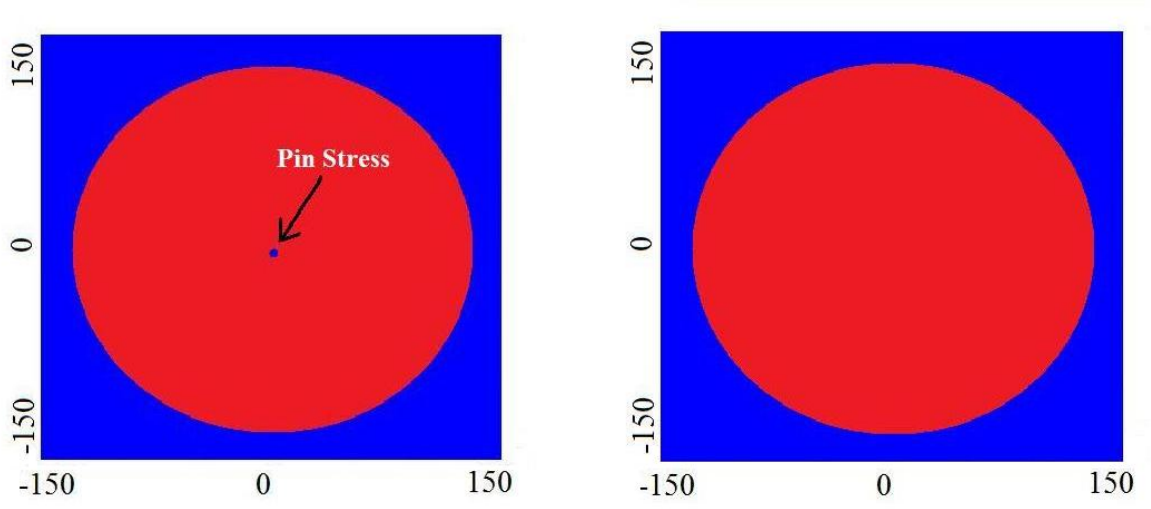

(a) Top BCs

(b) Bottom BCs

Figure 3.2: (a) The outside blue color represents fixed boundary conditions created by the clamping of the top and bottom plates, while the red color represents free, unconstrained boundary conditions. The small blue spot in the center is the pin contacting the sample. (b) Bottom boundary conditions with the same color representation as (a) with the exception of the stressor pin (see Appendix B for more details.)

the same compliance tensors; the elements of the compliance tensor, C, deviate by 5% at most. Thus we can treat the material as approximately one of uniform GaAs in order to perform the stress-strain analysis. Once the displacements(u_l) are determined, they can be used to calculate the strains through the relation:

$$\epsilon_{ij} = \frac{1}{2}\left(\frac{\partial u_i}{\partial x_j} + \frac{\partial u_j}{\partial x_i}\right). \tag{3.2}$$

These calculated strains can then be inserted into the Luttinger-Kohn/Pikus-Bir Hamiltonian (see Appendix C) in combination with accounting for the correct wavevectors due to the quantum wells. This Hamiltonian is given by:

$$H_{LK,PB} = -\begin{pmatrix} P+Q & -S & R & 0 \\ -S^\dagger & P-Q & 0 & R \\ R^\dagger & 0 & P-Q & S \\ 0 & R^\dagger & S^\dagger & P+Q \end{pmatrix}, \tag{3.3}$$

with the basis $\mid 3/2;3/2\rangle$, $\mid 3/2;1/2\rangle$, $\mid 3/2;-1/2\rangle$ and $\mid 3/2;-3/2\rangle$ (See Eq. 1.4). The parameters are given by:

$$\begin{aligned} P &= \frac{\hbar^2\gamma_1}{2m_e}\left(k_x^2+k_y^2+k_z^2\right) - a_v(\epsilon_{xx}+\epsilon_{yy}+\epsilon_{zz}) \\ Q &= \frac{\hbar^2\gamma_2}{2m_e}\left(k_x^2+k_y^2-2k_z^2\right) - \frac{b}{2}(\epsilon_{xx}+\epsilon_{yy}-2\epsilon_{zz}) \\ R &= \sqrt{3}\frac{\hbar^2}{2m_e}\left[-\gamma_2\left(k_x^2-k_y^2\right)+i2\gamma_3 k_x k_y\right] - \frac{\sqrt{3}b}{2}(\epsilon_{xx}-\epsilon_{yy}) - id\epsilon_{xy} \\ S &= \sqrt{3}\frac{\hbar^2\gamma_3}{2m_e}\left(k_x-ik_y\right)k_z - d(\epsilon_{xz}-i\epsilon_{yz}), \end{aligned} \tag{3.4}$$

where the γ_i's are the Luttinger parameters, a_v is the hydrostatic deformation potential, and b and d are the shear deformation potentials (see Ref. [23]). This gives us the change of energy and character of the valence band. This, in conjunction with the shift in the conduction band,

$$H = -a_c(\epsilon_{xx}+\epsilon_{yy}+\epsilon_{zz}), \tag{3.5}$$

where a_c is the conduction band hydrostatic deformation potential, gives us our new exciton energy. Figure 3.3a shows the results of this model applied to a 140 Å quantum well.

We can then calculate the new polariton states from these shifted exciton states from Eq. (1.22), while also keeping in mind that the exciton oscillator strength can change due to light- heavy-hole mixing. Under the strain deformations given by our stressing apparatus, the S terms found in the off-diagonal elements of the Pikus-Bir Hamiltonian are negligible, while the R terms which couple the light and heavy holes are large. Also, the $P+Q$ and the $P-Q$ terms along the diagonal of the Pikus-Bir Hamiltonian force the light and heavy hole closer in energy with increasing stress (initially, these light- and heavy-hole states were separated by the quantum well confinement.) When R is roughly the size of the splitting between these two states, they mix. The new polariton Hamiltonian with two types of oscillators becomes:

$$H_{LK,PB} = -\begin{pmatrix} E_{HH1} & 0 & \Omega_1 \\ 0 & E_{LH1} & \Omega_2 \\ \Omega_1 & \Omega_2 & E_{phot} \end{pmatrix}, \tag{3.6}$$

where E_{HH1} (E_{LH1}) is the heavy-hole (light-hole) energy, Ω_1 is the heavy-hole Rabi energy, Ω_2 is the light-hole Rabi energy which is different from Ω_1. These results are shown in Fig. 3.3b.

3.2 SPLITTING OF POLARITON STATES WITH STRESS

In general, strain allows for the possibility of a reduced symmetry of the lattice. This reduction in symmetry possibly gives rise to light- and heavy-hole mixing. The Pikus-Bir Hamiltonian accurately describes the effects that strain has on the electronic band structure of semiconductors such as energy band shifts and valence-band mixing. It does not, however, include any interaction between valence- and conduction-band states such as electron-hole exchange. Strain mixing, coupled with the mixing due to electron-hole exchange, can lead to significant changes in the exciton's ability to couple to the photon field. While energy splittings in the exciton states due to mixing and anisotropic exchange [51, 52] tend to be 150 μeV [47, 48] or smaller [53] in quantum wells, the energy splitting of polaritons can be around 700 μeV [54] and even higher, partially due to the fact that the relative oscillator

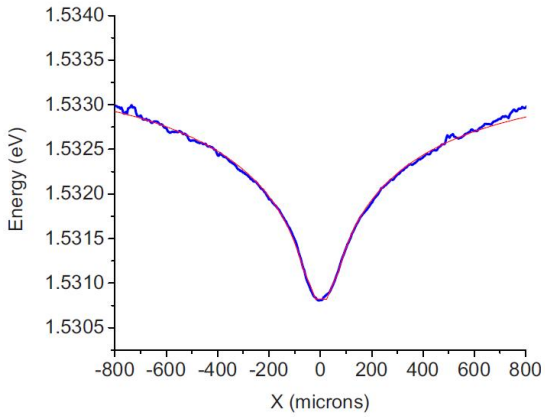

(a) Exciton

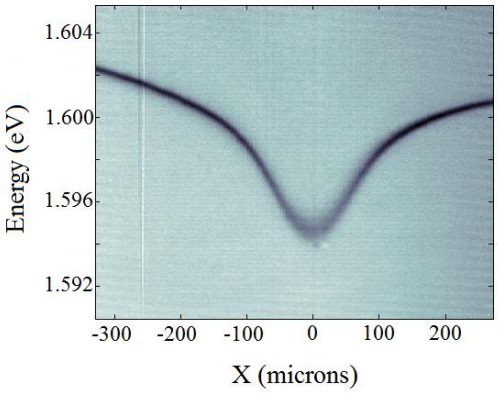

(b) Polariton

Figure 3.3: (a) P.L. emission (blue curve) and fit using the Pikus-Bir model(red curve) to a exciton gas in a 140 Å quantum well under the same stress geometry as Fig. 3.1a. (b) Polarized reflectivity measurement of the lower polariton state under similar stress conditions as (a).

strength of the exciton states also changes under exchange. When electron-hole exchange is taken into account, the degeneracy of the lower polariton is broken, splitting it into two energy-resolved, linearly polarized states.

3.2.1 Theory of Electron-Hole Exchange

To deduce the electron-hole exchange term from first principles we begin, following the methods of Hanamura and Haug [55], with the interaction term from Eq. (1.1). The interaction energy is written in terms of the electron Fermi field operators, with spin now included, as

$$H = \frac{1}{2}\sum_{s,s'}\int d\mathbf{x}\int d\mathbf{x}'\frac{e^2}{4\pi\epsilon\left|\mathbf{x}-\mathbf{x}'\right|}\psi_s^\dagger(\mathbf{x})\psi_{s'}^\dagger(\mathbf{x}')\psi_s'(\mathbf{x}')\psi_s(\mathbf{x}), \tag{3.7}$$

where

$$\psi_s(\mathbf{x}) = \frac{1}{\sqrt{V}}\sum_{n,\mathbf{k}}\langle u_{n,\mathbf{k}} \mid \mathbf{x}, s\rangle e^{i\mathbf{k}\cdot\mathbf{x}}\mathbf{b}_{n\mathbf{k}}, \tag{3.8}$$

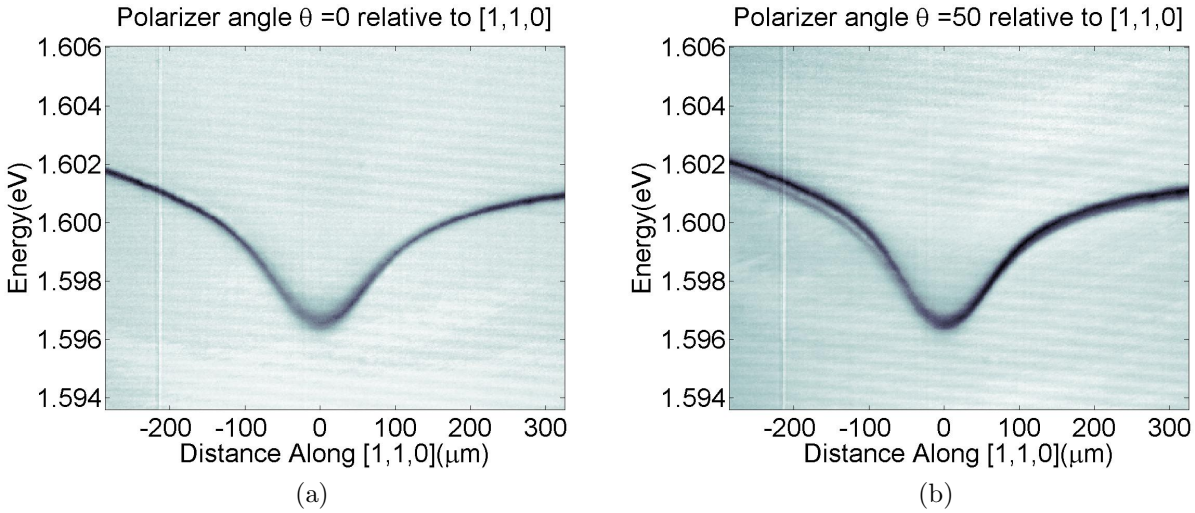

Figure 3.4: (a),(b) and (c) are reflectivity measurements taken with a polarizer positioned before the sample. The angle is referenced from the [1,1,0] plane of the crystal. Notice how both (a) and (c) show only one individual state each, while two states are visible in (b).

in which $\langle u_{n,\mathbf{k}} \mid \mathbf{x}, s\rangle$ is the spin-s projection of the Bloch cell function for an electron with the band index n and momentum $\mathbf{k}$, and $\mathbf{b}_{n\mathbf{k}}$ and $\mathbf{b}^\dagger_{n\mathbf{k}}$ are the fermionic annihilation and creation operators. Substitution gives

$$\begin{aligned} H = \sum_{n,,\mathbf{k}} \mathbf{b}^\dagger_{n\mathbf{k}} \mathbf{b}^\dagger_{n'\mathbf{k}'} \mathbf{b}_{n''\mathbf{k}''} \mathbf{b}_{n'''\mathbf{k}'''} \sum_{s,s'} \int d\mathbf{x} \int d\mathbf{x}' e^{-i(\mathbf{k}\cdot\mathbf{x}+\mathbf{k}'\cdot\mathbf{x}'-\mathbf{k}''\cdot\mathbf{x}''-\mathbf{k}''\cdot\mathbf{x}'')} \\ \times \langle \mathbf{x}, s \mid u_{n,\mathbf{k}}\rangle \langle \mathbf{x}', s' \mid u_{n',\mathbf{k}'}\rangle \langle u_{n'',\mathbf{k}''} \mid \mathbf{x}', s'\rangle \langle u_{n''',\mathbf{k}'''} \mid \mathbf{x}, s\rangle \frac{e^2}{4\pi\epsilon \left|\mathbf{x}-\mathbf{x}'\right|}, \end{aligned} \tag{3.9}$$

where the summation over $\{n, \mathbf{k}\}$ stands for summation over all bands n and momenta $\mathbf{k}$. We make the long-wavelength approximation that all $\mathbf{k}$'s are small compared to the Brillouin zone, which means that the plane-wave terms are nearly constant over a unit cell. We write $\mathbf{x} = \mathbf{X} + \mathbf{y}$, where $\mathbf{X}$ is the position of a cell and $\mathbf{y}$ is the position inside a cell, and take the lowest order of the $\mathbf{k}\cdot\mathbf{p}$ expansion for the Bloch cell functions, to write

$$\begin{aligned} \frac{1}{V} \int d\mathbf{x} e^{-i(\mathbf{k}-\mathbf{k}''')\cdot\mathbf{x}} \langle \mathbf{x}, s \mid u_{n,\mathbf{k}}\rangle \langle u_{n''',\mathbf{k}'''} \mid \mathbf{x}, s\rangle \approx \\ \frac{1}{N} \sum_{\mathbf{X}} e^{-i(\mathbf{k}-\mathbf{k}''')\cdot\mathbf{X}} \frac{1}{\Omega} \int_\Omega d\mathbf{y} \langle \mathbf{y}, x \mid u_{n,0}\rangle \langle u_{n''',0} \mid \mathbf{y}, s\rangle, \end{aligned} \tag{3.10}$$

where N is the number of unit cells and Ω is the volume of a unit cell. This yields the approximate result

$$\begin{aligned} H = \sum_{\{n,\mathbf{k}\}} \mathbf{b}^\dagger_{n\mathbf{k}} \mathbf{b}^\dagger_{n'\mathbf{k}'} \mathbf{b}_{n''\mathbf{k}''} \mathbf{b}_{n'''\mathbf{k}'''} \sum_{\mathbf{X},\mathbf{X}'} e^{-i(\mathbf{k}\cdot\mathbf{X}+\mathbf{k}'\cdot\mathbf{X}'-\mathbf{k}''\cdot\mathbf{X}'-\mathbf{k}'''\cdot\mathbf{X})} \\ \times \sum_{s,s'} \frac{1}{\Omega^2} \int_\Omega d\mathbf{y} \int_\Omega d\mathbf{y}' \langle \mathbf{y}, s \mid u_{n0}\rangle \langle \mathbf{y}', s' \mid u_{n'0}\rangle \\ \times \langle u_{n''0} \mid \mathbf{y}', s'\rangle \langle u_{n'''0} \mid \mathbf{y}, s\rangle \frac{e^2}{4\pi\epsilon \left|\mathbf{x}-\mathbf{x}'\right|}. \end{aligned} \tag{3.11}$$

The denominator $|\mathbf{x} - \mathbf{x}'|$ must be treated with care. We break the sum over $\mathbf{X}$ and $\mathbf{X}'$ into two parts, one with $\mathbf{X} = \mathbf{X}'$ ("short range") and one with $\mathbf{X} \neq \mathbf{X}'$ ("long range"). The latter term is approximately

$$\begin{aligned} H = \sum_{\{n,\mathbf{k}\}} \mathbf{b}^\dagger_{n\mathbf{k}} \mathbf{b}^\dagger_{n'\mathbf{k}'} \mathbf{b}_{n''\mathbf{k}''} \mathbf{b}_{n'''\mathbf{k}'''} \sum_{\mathbf{X}\neq\mathbf{X}'} e^{-i(\mathbf{k}\cdot\mathbf{X}+\mathbf{k}'\cdot\mathbf{X}'-\mathbf{k}''\cdot\mathbf{X}'-\mathbf{k}'''\cdot\mathbf{X})} \frac{e^2}{4\pi\epsilon \left|\mathbf{x}-\mathbf{x}'\right|} \\ \times \sum_{s} \frac{1}{\Omega} \int_\Omega d\mathbf{y} \langle \mathbf{y}, s \mid u_{n0}\rangle \langle u_{n'''0} \mid \mathbf{y}, s\rangle \\ \times \sum_{s'} \frac{1}{\Omega} \int_\Omega d\mathbf{y}' \langle \mathbf{y}', s' \mid u_{n'0}\rangle \langle u_{n''0} \mid \mathbf{y}', s'\rangle. \end{aligned} \tag{3.12}$$

The sum over $\mathbf{X}$ and $\mathbf{X}'$ can be converted to an integral and resolved as

$$\frac{1}{2V}\frac{e^2/\epsilon}{|\Delta\mathbf{k}|^2}\delta_{\mathbf{k}+\mathbf{k}',\mathbf{k}''+\mathbf{k}'''}, \tag{3.13}$$

where $\Delta\mathbf{k} = \mathbf{k} - \mathbf{k}''' = \mathbf{k}'' - \mathbf{k}'$. For $n = n'''$ and $n' = n''$ this term gives the standard intraband Coulomb interaction, either between two carriers in the same band, or in the case of an electron and hole, the direct Coulomb interaction between an electron and hole that causes exciton formation. When $n \neq n'''$ and $n' \neq n''$, this is the long-range exchange term. The long-range exchange term vanishes in the long-wavelength limit assumed here due to the orthonormality of the Bloch cell functions; higher-order $\mathbf{k}\cdot\mathbf{p}$ expansion [16, 17, 18] of the Bloch cell functions will give a k-dependent term. On the other hand, the short-range term has a matrix element

$$\begin{aligned}\langle U_{n,n',n'',n'''}\rangle = \sum_{s,s'}\frac{1}{\Omega^2}\int_\Omega d\mathbf{y}\int_\Omega d\mathbf{y}'\langle\mathbf{y},s \mid u_{n0}\rangle\langle\mathbf{y}',s' \mid u_{n'0}\rangle \\ \times\langle u_{n''0} \mid \mathbf{y}',s'\rangle\langle u_{n'''0} \mid \mathbf{y},s\rangle\frac{e^2}{4\pi\epsilon\,|\mathbf{y}-\mathbf{y}'|},\end{aligned} \tag{3.14}$$

which can be nonzero for Bloch cell functions in different bands. To determine the exchange energy for an exciton, we use the Wannier exciton state, written as

$$\mid cv\rangle = \sum_{\mathbf{k}}\phi(\mathbf{k})\mathbf{b}^\dagger_{c\mathbf{k}}\mathbf{b}_{v\mathbf{k}}\mid 0\rangle. \tag{3.15}$$

This is just Eq. (1.10) with no center-of-mass momentum, where c and v are indices that pick out specific conduction and valence-band states, respectively, and $\phi(\mathbf{k})$ is the momentum-space wave function of the relative exciton motion (we assume that the center-of-mass motion of the exciton is negligible). The exchange energy is then given by

$$\begin{aligned}\langle ex \mid H \mid ex\rangle = \left[\langle 0 \mid \sum_{\mathbf{p}'}\phi^*(\mathbf{p}')\mathbf{b}^\dagger_{v,\mathbf{p}'}\mathbf{b}_{c,\mathbf{p}'}\right]\frac{\Omega}{V}\langle U_{cvcv}\rangle \\ \times\sum_{\mathbf{k},\mathbf{k}',q}\mathbf{b}^\dagger_{c,\mathbf{k}}\mathbf{b}^\dagger_{v,\mathbf{k}'}\mathbf{b}_{c,\mathbf{k}'+\mathbf{q}}\mathbf{b}_{c,\mathbf{k}-\mathbf{q}}\left[\sum_{\mathbf{p}}\phi^*(\mathbf{p})\mathbf{b}^\dagger_{c,\mathbf{p}}\mathbf{b}_{c,\mathbf{p}}\mid 0\rangle\right],\end{aligned} \tag{3.16}$$

where the sum over $\mathbf{X}(=\mathbf{X}')$ has been used to give a momentum-conserving δ function. When all the creation and annihilation operators are resolved into constraints on the momentum vectors, this becomes

$$\begin{aligned}\langle ex \mid H \mid ex\rangle &= -\left(\sum_{\mathbf{p}'}\phi^*(\mathbf{p}')\right)\frac{\Omega}{V}\langle U_{cvcv}\rangle\left(\sum_{\mathbf{p}}\phi^*(\mathbf{p})\right)+\left(\sum_{\mathbf{p}}|\phi^*(\mathbf{p})|^2\right)\frac{\Omega}{V}\langle U_{cvcv}\rangle \\ &= -|\phi(0)|^2\,\Omega\langle U_{cvcv}\rangle,\end{aligned} \tag{3.17}$$

where we have found the real-space exciton wave function through the Fourier transform $\phi(\mathbf{x}) = (1/\sqrt{V})\sum_{\mathbf{k}}\phi(\mathbf{k})e^{i\mathbf{k}\cdot\mathbf{x}}$; the second term in the first line of Eq. (3.17) is negligible since the wave function is normalized so this term is of order $1/V$ times the first term. The short-range exciton exchange energy is therefore proportional to the probability of the electron and hole in the exciton Wannier wave function being at the same place.

The matrix element, Eq. (3.14), for interband transitions relies on the spatial variation in the Coulomb potential to give a nonzero integral. However, the Coulomb interaction does not flip spin. Therefore, the exchange interaction applies only for electron and hole states with the same spin. Since the case of same spins corresponds to the spin-triplet case and the case of different spins corresponds to the spin-singlet state, in the case of pure spin states, we account for this with a factor $-\mathbf{S}_e\cdot\mathbf{S}_h$ [16].

3.2.2 State Mixing Under Stress

In the case when the conduction-band eigenstates are pure spin states but the valence-band eigenstates are not, as in GaAs, we cannot just worry about the diagonal terms $\langle ex \mid H \mid ex\rangle$ for the exciton energy; we must also worry about mixing terms $\langle ex' \mid H \mid ex\rangle$, where the exciton states can be different, and the resulting terms $U_{c'v'cv}$. The four relevant GaAs valence band states at zone center are given by Eq. (1.4). We must take the projection of the valence-band state onto the same spin state as the conduction-band state, for the eight exciton states given by the four valence states combined with the two conduction-band states. If we write the electron-hole exchange matrix in the same basis as the Pikus-Bir Hamiltonian (Eq. (3.4)), namely the eelctron and hole product states $\mid hole\rangle\otimes\mid elec\rangle$, i.e.,

$|\ 3/2\rangle\ |\uparrow\rangle$,$|\ 3/2\rangle\ |\downarrow\rangle$,$|\ 1/2\rangle\ |\uparrow\rangle$, $|\ 1/2\rangle\ |\downarrow\rangle$,$|\ -1/2\rangle\ |\uparrow\rangle$,$|\ -1/2\rangle\ |\downarrow\rangle$, $|\ -3/2\rangle\ |\uparrow\rangle$, $|\ -3/2\rangle\ |\downarrow\rangle$, we find

$$\begin{pmatrix} 1 & 0 & 0 & 0 & 0 & 0 & 0 & 0 \\ 0 & 0 & -\frac{4}{\sqrt{3}} & 0 & 0 & 0 & 0 & 0 \\ 0 & -\frac{4}{\sqrt{3}} & \frac{2}{3} & 0 & 0 & 0 & 0 & 0 \\ 0 & 0 & 0 & \frac{1}{3} & \frac{4}{3} & 0 & 0 & 0 \\ 0 & 0 & 0 & \frac{4}{3} & \frac{1}{3} & 0 & 0 & 0 \\ 0 & 0 & 0 & 0 & 0 & \frac{1}{3} & -\frac{4}{\sqrt{3}} & 0 \\ 0 & 0 & 0 & 0 & 0 & -\frac{4}{\sqrt{3}} & 0 & 0 \\ 0 & 0 & 0 & 0 & 0 & 0 & 0 & 1 \end{pmatrix}. \tag{3.18}$$

This is the same result as obtained using $\frac{1}{2}\mathbf{S}_e \cdot \mathbf{S}_h + \frac{1}{2}$, except for the multiplicative constant, for the case $a_x = a_y = a_z$, where the a_i's are exchange constants as shown later in Eq. (3.19). This shows that at a fundamental level, the electron-hole exchange splitting term is proportional to $\mathbf{S}_e \cdot \mathbf{S}_h$, not $\mathbf{S}_e \cdot \mathbf{J}_h$ [53], which does not give an equivalent matrix.

In a quantum well and under shear stress, the p states $|\ 1\rangle$,$|\ 0\rangle$, and $|\ -1\rangle$ are no longer the orbital eigenstates, as x, y, and z are no longer equivalent. The new eigenstates become $|\ x\rangle = \frac{1}{\sqrt{2}}(|\ -1\rangle - |\ 1\rangle)$, $|\ y\rangle = \frac{i}{\sqrt{2}}(|\ -1\rangle + |\ 1\rangle)$ and $|\ z\rangle = |\ 0\rangle$.

After manipulating the form of Eq. (3.18) to include any asymmetry introduced to the lattice through quantum-well confinement and strain, the form of the exchange interaction becomes

$$H_{exc} = -\sum_i a_i S_{h,i} S_{c,i} \tag{3.19}$$

where a_i are simply coefficients which can vary the asymmetry of the exchange process. Little is known about the details of these parameters, so they become fit parameters for us. This matrix is expanded in the basis of electron-hole product states and added to the Pikus-Bir/Luttinger-Kohn Hamiltonian expanded in the same basis. Figure 3.5 shows the results of such a calculation using the parameters a_i as fit parameters, taking into account the change of energy due to the Rabi splitting.

Until this work, the largest measured electron-hole exchange splittings, around 150 μeV, were much smaller than the linewidth of the exciton. Here, with linewidths of less than 250 μeV, we can extract the exchange splitting of 700 μeV with greater accuracy. The exchange-

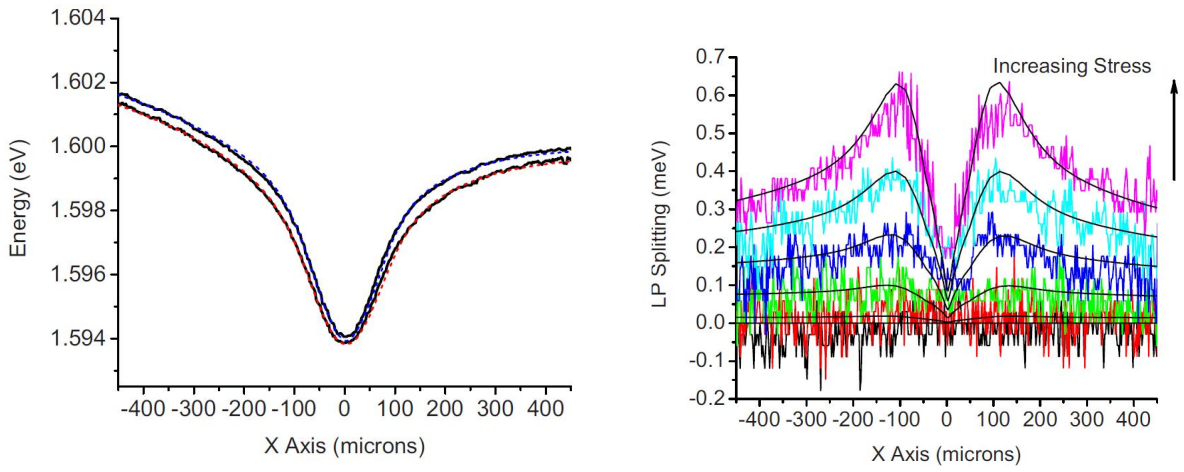

Figure 3.5: (a) The exchange model fit (red and blue, dashed curves), including the Pikus-Bir Hamiltonian, to PL data (black curves) for a fixed applied stress. (b) The measured exchange energy-splitting at several different values of applied stress with theory. The splitting becomes larger when more stress is applied.

energy splitting seen here is larger than those previously recorded because of the nature of how shear strain, coupled with electron-hole exchange, changes the exciton energy which then causes it to couple differently to the cavity. The stress traps created in these experiments tend to push the light-hole exciton closer in energy to the heavy-hole exciton (see Fig. 3.8), and the term R in Eq. (3.4) couples the light- and heavy-hole excitons when there is a shear strain. Such is the case on the sides of the stress trap. This causes a mixing that changes the oscillator strength of the light-hole ($|\pm 1/2\rangle$) and heavy-hole ($|\mp 3/2\rangle$) excitons and also produces linearly polarized states [56]. However, this is not enough to split the degeneracy of the lower polariton. Exchange, coupled with strain, does this, because exchange induces a splitting of the energy between the heavy-hole $|+3/2\rangle$ and $|-3/2\rangle$ state. This splitting changes the relative amount of mixing that the heavy- and light-hole excitons can achieve through the Pikus-Bir term, causing these states to have different oscillator strengths and hence splitting the upper- and lower-polariton energy. Without the strong coupling offered by the polariton, this exciton exchange splitting has not been measured under similar types

of stress experiments [57].

3.3 BOSE-EINSTEIN CONDENSATION, LASING AND THE ROLE OF THE STRESS TRAP

We have used stress to create a harmonic potential for polaritons in GaAs microcavities and have previously reported that the polaritons undergo spontaneous coherence in the trap [1]. Here I present results for both trapped conditions and resonant, untrapped conditions in the same sample. We find two distinct types of transitions. At low density in the trap, the polaritons remain in the strong-coupling regime while going through the threshold for onset of coherence; at higher density, there is a different threshold behavior, which occurs with weak coupling and can be identified with lasing; this transition occurs both with and without a trap. We will see that the transition at lower density can therefore be identified as a type of nonequilibrium Bose-Einstein condensation.

The polaritons used in these experiments had a short lifetime ($\sim$10 ps). In a typical experiment, a steady-state or quasi-steady-state population of polaritons is maintained by incoherent optical or electrical pumping. Questions therefore arise as to how well the phase transitions of these quasiparticles under different conditions can be described as Bose-Einstein condensation. Of course, the absolute time scale does not matter; what matters is whether the time scale for interactions of the particles is shorter than their lifetime, so that they can reach thermal equilibrium. At high density, polaritons can collide with each other on subpicosecond time scales, allowing the particles to approach equilibrium within their lifetime. If the density is too high, however, phase-space filling of the valence and conduction bands can set in, removing the strong coupling of the photonic and electronic states, which in turn means that one can no longer think of the system as elastically scattering bosonic particles and instead must view it as lasing of photons amid an incoherent electron-hole plasma.

In our experiments, we trapped polaritons in an in-plane harmonic potential created by applied stress using methods discussed in Section 3.1. A harmonic potential has the

advantage that it makes true Bose condensation possible in two dimensions [58, 59] and reduces the total number of particles needed for coherent effects by changing the density of states of the particles. In the limit of zero spring constant, i.e., flat potential, the condensate fraction vanishes [59, 60] but the superfluid fraction is nonzero [59]. As the spring constant of the trap is increased, the condensate fraction and the superfluid fraction both increase at a given temperature [59]; in other words, the total particle density needed for spontaneous coherence is reduced. The critical number of particles for non-interacting bosons in a 2D stress trap is [38]

$$N_c = \frac{m\pi^4}{3h^2\alpha}(k_B T_c)^2, \tag{3.20}$$

where α is the spring constant given in the energy relation $U = \alpha R^2$. The smaller the FWHM of the harmonic potential, the larger α becomes, and the required density to reach critical density drops for a fixed temperature.

When inhomogeneous applied stress is used to shift the excitonic states, a harmonic potential is produced in real space which gives a force that confines the polaritons. It has been argued for a similar system [3] that a random potential arising from disorder effectively also makes an in-plane trap which can confine the particles and allow true BEC. The random potential severely inhibits long-range motion of the particles, however. In our experiments with GaAs structures, the disorder is very low, and even the short-lifetime polaritons can move tens of microns and approach spatial equilibrium in a macroscopic trap.

Two goals in these experiments have essentially a philosophical motivation. One is to show that the coherence is truly spontaneous and not just mapping of the coherence of the pump laser to the coherence of the light emission from the microcavity states. It has recently been argued [61] that even when a coherent pump laser directly couples to the polariton states, the coherence of the polariton population still reflects spontaneous symmetry breaking and is not directly coupled to the coherence of the laser; others [62] have argued that the case of direct coupling of the laser to the polariton states can be treated entirely as a classical nonlinear process, transferring the coherence of the laser onto the polariton ensemble. One way to avoid any question of inherited coherence is to generate the polaritons through an inherently incoherent process, e.g., one that involves phonon emission.

A second goal is to show that the coherence truly involves the electronic states so that

we can term this type of transition "coherent matter", similar to a superconductor. This goal means that the system should remain in the strong-coupling regime, that is, that the eigenstates of the system retain a wave function that is a mixture of photon and exciton. If the system is not in strong coupling, it is essentially the same as a standard laser.

To accomplish the first goal, two methods of pumping can be used. One is to use a laser resonant in energy with the polariton states, but with very steep angle of incidence [63]. As discussed in Section 2.2.2, since the in-plane momentum $\mathbf{k}_{\|}$ must be conserved in both the absorption and emission process when carriers in the 2D plane couple to external photons, the high angle of incidence creates excitons with large in-plane $\mathbf{k}_{\|}$. It is then assumed that the excitons must emit many phonons before scattering down into low-$\mathbf{k}_{\|}$ states and converting into polaritons near $\mathbf{k}_{\|} \approx 0$, and the interaction with the phonons destroys all the original coherence from the laser. One drawback of this method is that the absorption near resonance in the microcavity is poor, and therefore very intense laser pulses must be used to produce enough polaritons to see coherence effects. A second method is to tune the pump laser to the first absorption maximum above the stop band of the cavity [1, 3]. In this case the carriers must emit many phonons to fall down into the polariton states, and therefore, just as in the high-incidence angle method, the emission of the phonons destroys the original coherence as seen in the lack of coherence of the polaritons below the threshold for BEC [1]. The strong absorption allows the use of much less intense continuous wave laser pumping. This is the method we use.

The main method of demonstrating the second goal, showing that the system is in the strong-coupling regime during the onset of coherence, is to monitor the shifts in the upper and lower polariton spectral lines. In the case of weak coupling, the splitting between the upper and lower polaritons at resonance will vanish, and the photon emission will occur at the energy of the cavity mode. Thus one expects that if the coherent photon emission occurs with photon energy near to the lower polariton energy and well below the bare cavity photon mode, and the upper polariton energy is relatively unshifted, then the system is still in the strong-coupling regime. As reported earlier [1], in our experiments using stress to produce an in-plane harmonic potential for the polaritons and incoherent cw pumping above the stop band as in the second method described above, we have observed a transition above a

critical pump intensity, which is indicated by spectral narrowing, first-order coherence, onset of linear polarization, and nonlinear gain of the output light. The upper and lower polariton states shifted less than 0.5 meV during this transition, compared to a Rabi splitting of 15 meV, consistent with strong coupling.

Figure 3.6a shows the emission at very low pump power. The spectral width is narrow, consistent with the low density and temperature of the polaritons. When the density is increased, the spectral width first broadens, as seen in Fig. 3.6b, as expected for collision broadening when the polaritons are at high enough density for substantial polariton-polariton scattering. At the critical threshold for coherence, the spectrum narrows (Fig. 3.6c). In addition to the collisional broadening, all of the spectral widths in these measurements are broader than the intrinsic line width for at least two reasons. One is that the multimode pump laser has fluctuations in power, which lead to shifts in the density-dependent blueshift of the line in time-averaged experiments. In the experiments of Love et al. [45], when an intensity-stabilized laser is used, very narrow line widths (0.05 meV) and long coherence times (150 ps) are recorded for this type of polaritonic transition. Another reason for the spectral broadening is spatial integration over the entire trapped region in these angle-resolved experiments, including contributions from polaritons over a range of densities.

When the pump power is increased even further, as seen in Figs. 3.6d and e, the emission broadens strongly and shifts strongly upward. This is consistent with high-density effects such as phase-space filling and strong polariton-polariton interaction leading to breakdown of the pure polariton picture and the onset of weak coupling. Finally, as shown in Fig. 3.6f, a second line narrowing is seen at the same spot in the sample. This corresponds to standard lasing. There are therefore two distinct transitions as seen in Fig. 3.6. The lower-power threshold can be identified with Bose condensation of polaritons in the strong-coupling limit, while the higher threshold can be identified with standard lasing in the weak coupling regime.

The experiments with trapped polaritons showed several effects associated with BEC, namely, 1) spatial condensation in the center of the trap, even when the laser generated the polaritons far from that point, 2) momentum-space narrowing into a bimodal distribution, 3) sudden occurrence of linear polarization, and 4) first-order coherence. Although these all indicate that the phase transition is analogous to BEC, an objection can be raised. The

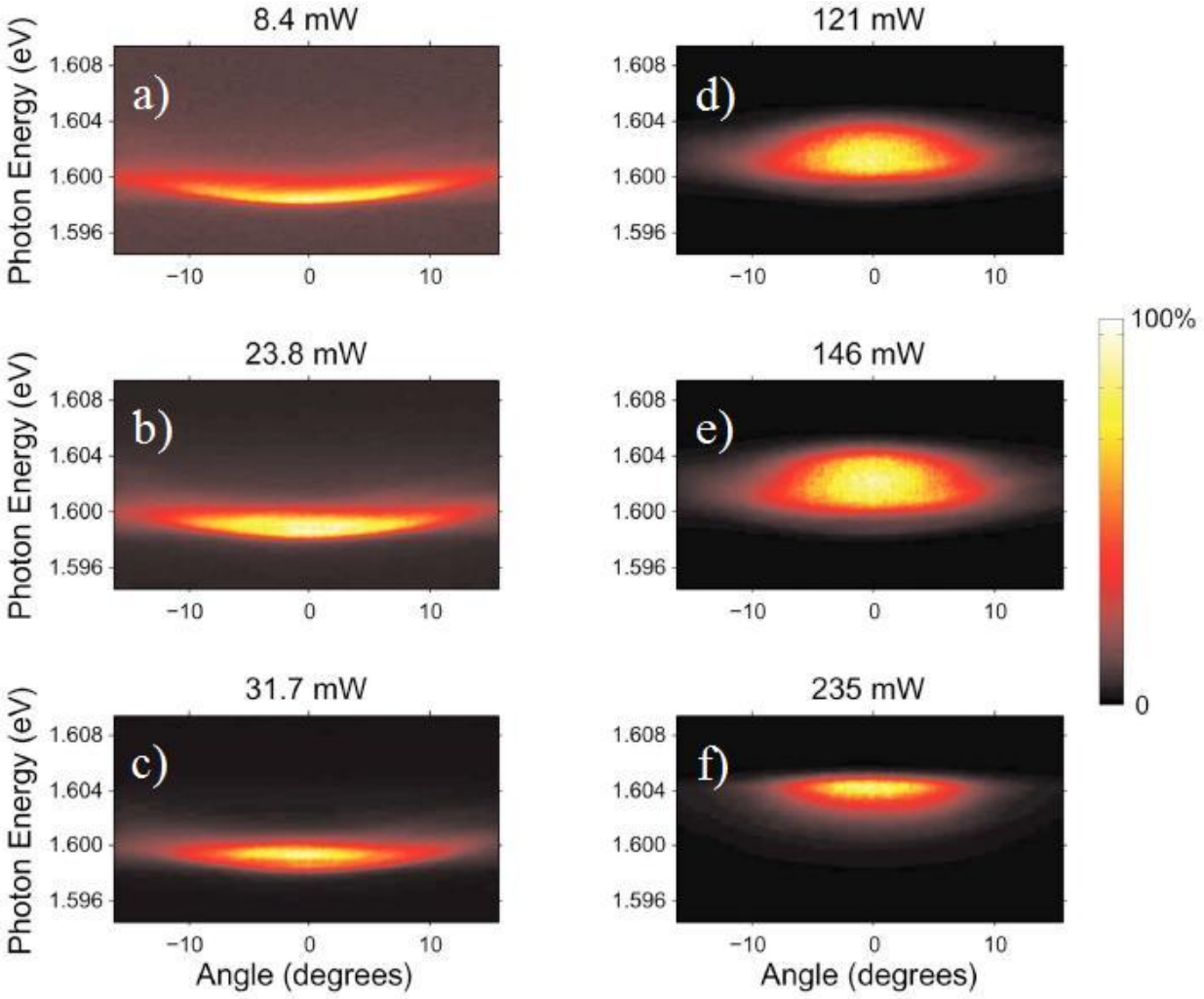

Figure 3.6: Angle-resolved and spectrally resolved emission from center of the stress trap in the microcavity structure for several different cw pump powers. The sample was in helium gas at 4 K and the polariton was resonantly detuned at the center of the stress trap; the laser focus spot size was 25 μm. These k-space images were acquired using the diffuser-plate method disussed in Section 2.2.2.1.

polariton densities at which these effects occurred is not so much less than the density at which a lasing transition can be seen without a trap in nearly identical GaAs-based structures [4]. Does the presence of the trap make such a difference, that the character of the phase transition is in the strong-coupling regime, when the particle density is only about a factor of 3 or 4 lower than the density at which a transition to standard lasing occurs in the weak-coupling regime when there is no trap? The answer, surprisingly, is yes.

A key way to learn about the nature of the transition is to see how the energy of the states varies as the detuning of the cavity is varied. If the system is in the weak-coupling regime, then the light-emitting state should be essentially the same as the cavity photon, and therefore the emission energy should follow the cavity photon energy as the detuning varies. This is what was observed in Ref. [4] and is what we observe when no stress is applied, as shown in Fig. 3.7. (As in Ref. [4], the cavity photon energy above the lasing threshold is red-shifted relative to the bare photon energy, presumably due to renormalization of the dielectric constant due to phase space filling.) When stress is applied to create the in-plane trap, however, we observe that the emitted photon energy at the threshold for coherence follows the lower polariton state as it shifts downward with stress due to the shift of the exciton state. This shows that the polaritons remain in the strong-coupling regime even above the threshold.

The squares in Fig. 3.8 show the energy positions of the polaritonic states in a microcavity, as the detuning between the exciton states and the cavity photon energy is changed by varying the applied stress, using the method discussed in Ref. [7]. The sample used for both Figs. 3.7 and 3.8 is the same as that used for Ref. [1] and is substantially the same as those used in Refs. [4] and [64], namely, a microcavity with three sets of four quantum wells at the antinodes of the confined optical mode in a microcavity with $Q \approx 3000$. The effective spring constant of the trap depends on the applied stress but was approximately 60 eV/cm^2 near zero detuning in these experiments, shallower than in Ref. [1] because a thicker substrate was used.

The positions of the lines in Fig. 3.8 are well fitted with a simple three-state coupling

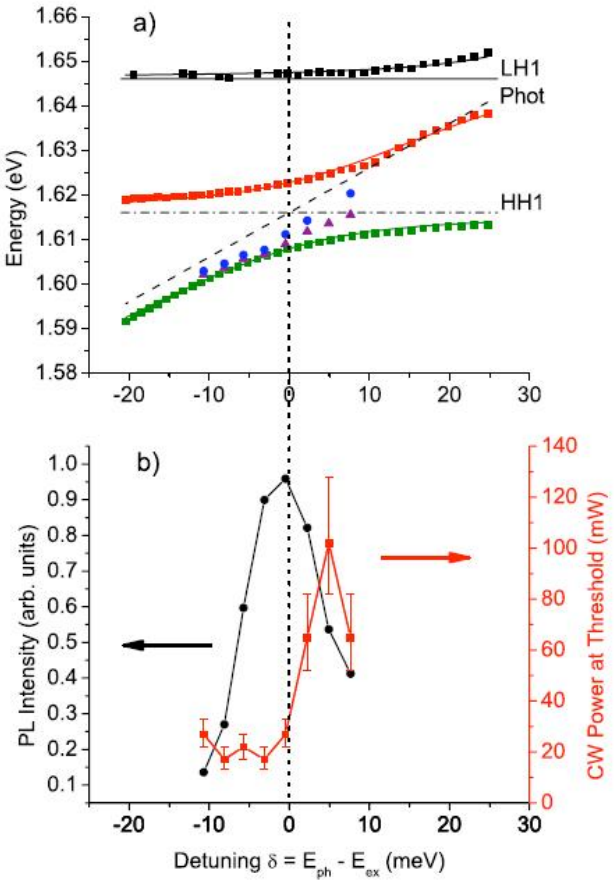

Figure 3.7: (a) Squares: energy of the reflection minima in the cavity as a function of detuning when no stress is applied, with the sample in helium vapor at T=4 K. The data are fit to the model of coupled states discussed in text using the exciton energies (HH1, LH1) and cavity photon energy (Phot) shown. Triangles: the photon emission energy when a laser excites the sample with power at the threshold for coherent effects, defined as the point of maximum linewidth before spectral narrowing occurs. Circles: the photon emission energy when the laser power is increased by a factor of 1.6 beyond the threshold power. (b) Circles, left axis: photoluminescence intensity of the lower polariton line for laser excitation density well below threshold (1.8 mW, spot size 35 μm). The intensity is maximum at resonance, $\delta = 0$. Squares, right axis: the laser power needed to reach the threshold for coherent behavior [corresponding to the power used for the triangles in (a)]. Laser wavelength was 714 nm at the top edge of the microcavity stop band; laser spot size was 25 μm.

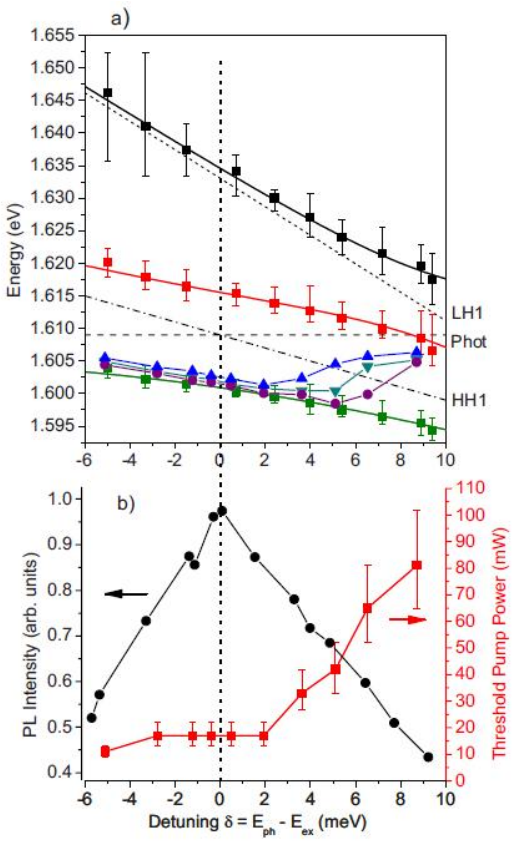

Figure 3.8: (a) Squares: energy of the reflection minima of the cavity as a function of detuning when stress is applied to vary the exciton energy while leaving the cavity photon energy unchanged (increasing stress=increasing δ). The data are fit to the model of coupled states discussed in text using the exciton energies (HH1, LH1) and cavity photon energy (Phot) shown. Circles: the peak photon emission energy when a laser excites the sample with power at the threshold for spectral narrowing. Inverted triangles: the photon emission energy when the laser excitation power is increased by a factor of 1.7 beyond the threshold. Upright triangles: 2.5 times the threshold. (b) Circles, left axis: photoluminescence intensity of the lower polariton line as a function of detuning for laser excitation density well below threshold (9 mW, spot size 85 μm). Squares, right axis: the laser power needed to reach the threshold for coherent behavior [corresponding to the power used for the circles in (a)]. Laser wavelength was 716 nm at the top edge of the microcavity stop band; laser spot size was 30 μm.

model, similar to Eq. (1.22), namely, the eigenvalues of the matrix

$$H_{LK,PB} = -\begin{pmatrix} E_{HH1} & 0 & \Omega_1 \\ 0 & E_{LH1} & \Omega_2 \\ \Omega_1 & \Omega_2 & E_{phot} \end{pmatrix}, \tag{3.21}$$

with $\Omega_1 = 7.5$ meV, $\Omega_2 = 6.0$ meV, $E_{phot} = 1.609$ eV, and E_{HH1} and E_{LH1} shifting with stress as shown in the dashed lines of Fig. 3.8. The shear term of the deformation-potential Hamiltonian acts to decrease the splitting of the heavy- and light-hole states in our stress configuration (See Appendix C) unlike the case of a homogeneous uniaxial stress. This splitting enters into the Hamiltonian (3.21) as a change of the energies E_{HH1} and E_{LH1}, which get closer together. The line positions are consistent with the reported masses [65] of the light and heavy holes, i.e., the heavy-hole exciton energy in the quantum wells, $E_{HH1} \propto (1/m_c + 1/m_h) = (1/0.067m_e + 1/0.33m_e)$, and light-hole exciton energy, $E_{HH1} \propto (1/m_c + 1/m_l) = (1/0.067m_e + 1/0.094m_e)$, with a well width of 61 Å. Both exciton states couple to the cavity mode when they are near resonance. At the resonance of the HH1 exciton state and the cavity photon, i.e., at zero detuning, the PL intensity has a maximum, as seen in Fig. 3.8b [66]. The FWHM of the PL intensity resonance around $k = 0$ is about 10 meV, the same resonance width seen in Fig. 3.7b, when there is no stress and the photon energy is tuned by varying the location of the laser spot on the sample.

Figure 3.8a also shows the energy of the photon emission when a laser pumps the sample under conditions similar to those in Ref. [1], i.e., the laser photon energy is tuned to the first absorption maximum above the microcavity stop band, and the laser is circularly polarized. The circles correspond to the photon energy when the excitation density is exactly at the threshold for coherent effects, which include line narrowing and a nonlinear increase in the emission intensity. The inverted and upright triangles correspond to laser powers which are higher than the threshold power by ratios of 1.7 and 2.5, respectively. These data show that even well above the threshold for the coherent effects, the lower polariton energy follows the exciton energy, not the photon energy, until the system is quite detuned. When it reaches detunings larger than $\delta = 4$ meV or so, the emission photon energy jumps up to near the bare cavity photon energy. At this same point, as shown in Fig. 3.8, the power needed to

cause coherent behavior increases rapidly. At this point we conclude that the system is in weak coupling.

There are thus two distinct transitions occurring in the same sample. The lower-power threshold can be identified with Bose condensation of polaritons in the strong-coupling limit and occurs only when the trap exists, while the higher threshold can be identified with standard lasing in the weak-coupling regime and occurs in the unstressed sample as well as in the stressed sample when it is detuned away from resonance.

This identification is supported by examining what happens at zero detuning when the pump power is increased. In this case we expect two transitions as the pump power is increasing at the same location on the sample. First, we expect to see the lower strong-coupling condensation transition, and then as power is increased, we expect to see the weak-coupling lasing transition kick in when the excitation density is comparable to that of the weak-coupling transition in the unstressed case. This is indeed what we see. Figure 3.9 shows the peak intensity, peak energy, and FWHM of the emission line as a function of pump power for the unstressed case at zero detuning, while Fig. 3.10 shows the same data for the case of the stress trap at zero detuning. The two cases are quite different. In the unstressed case shown in Fig. 3.9, the line narrowing and nonlinear emission do not occur until the emission line has shifted almost 4 meV, putting the system close to the weak-coupling regime. In the case with the stress trap, line narrowing occurs at much lower power, when the line shift is only about 0.5 meV. As seen in Fig. 3.10, the linewidth and shift remain around this plateau, and the intensity gain saturates until the density increases by a factor of 4, at which point the line broadens again, and the blueshift of the line jumps up several meV. A second threshold of line narrowing occurs along with a second range of nonlinear increase in the peak intensity, which we attribute to lasing in the weak-coupling regime. This second transition was not seen in the data of Ref. [1] because the maximum pump intensity was lower in those experiments. In both cases, the nonlinear gain region, which also corresponds to the region of narrowest linewidth, occurs over a range of density about a factor of 3 above the critical density. Above that, the light emission quickly begins to broaden and shift to higher energy.

The fact that the narrowing at the lower threshold is only about 25% in these data can

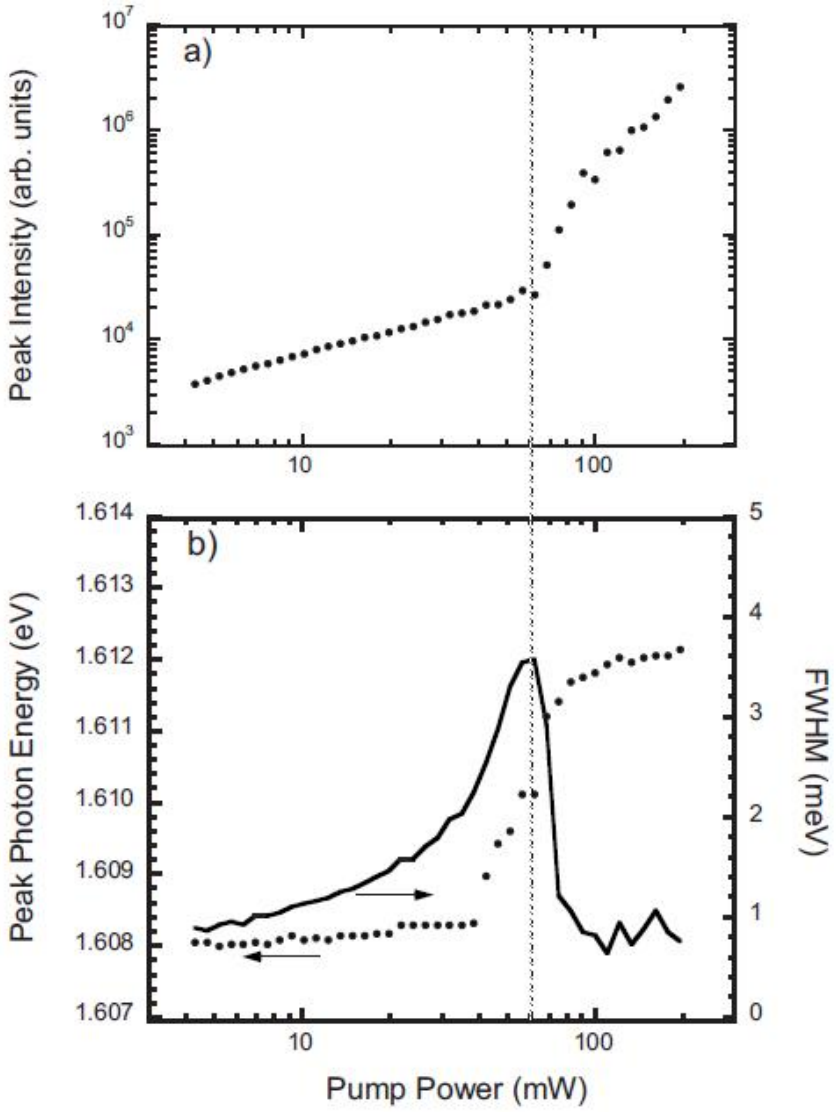

Figure 3.9: (a) Peak intensity of the emission from the lower polariton as a function of pump power when the system is at zero detuning when there is no stress trap. A location was chosen such that the exciton and cavity photon states are in resonance. All other conditions are essentially the same as those of Fig. 3.7. (b) Dots, left axis: peak photon energy of the emission for the same conditions as (a). Solid line, right axis: the FWHM of the emission spectrum under the same conditions. The acceptance angle for the PL detection was 0 ± 3^0. PL was integrated from the entire laser excitation spot, leading to spectral broadening of approximately 1 meV due to the spatial integration.

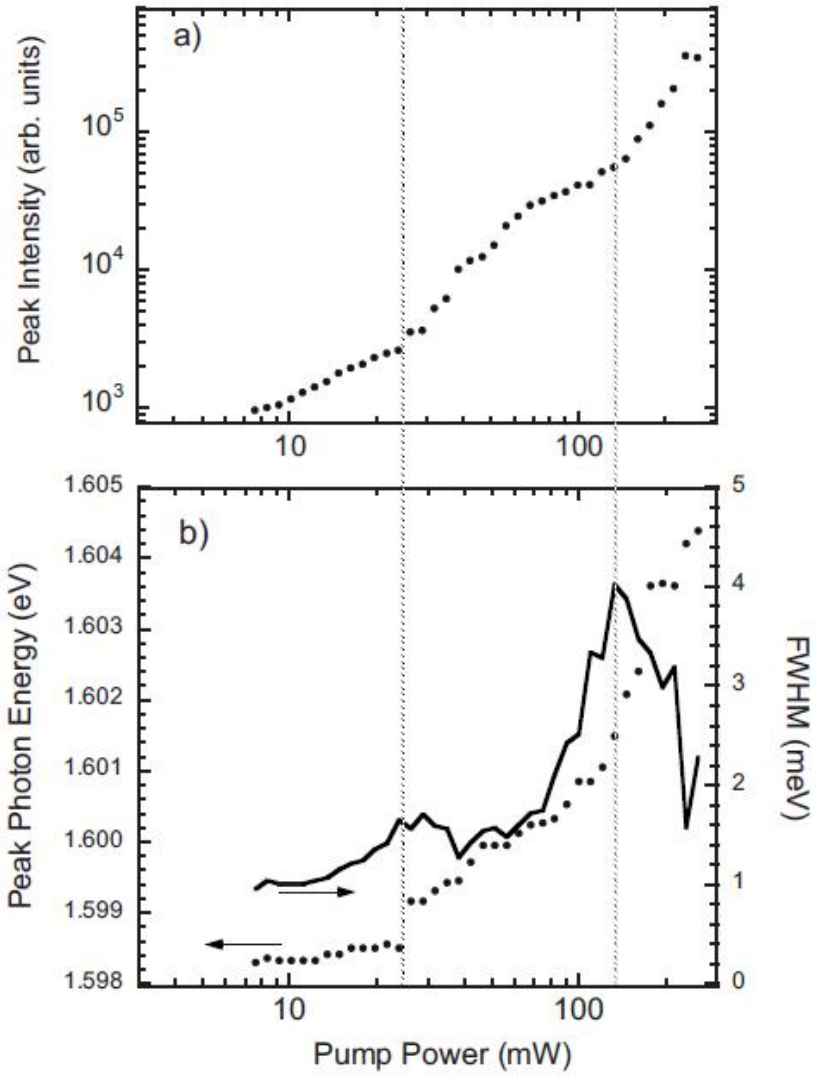

Figure 3.10: (a) Peak intensity of the emission from the lower polariton as a function of pump power when the system is at zero detuning when the polaritons are generated in a stress trap under the same conditions as those for Fig. 3.8. (b) Dots, left axis: peak photon energy of the emission for the same conditions as (a). Solid line, right axis: the FWHM of the emission spectrum under the same conditions. A different region of the sample was used so that the lower polariton energy at zero detuning in this case is around 1.5984 eV, as compared to 1.600 eV in Fig. 3.8. The acceptance angle for the PL detection and the region of spatial integration were the same as for Fig. 3.9.

be attributed to the effective spectral resolution of our system, which is about 1 meV due to two effects. One is spectral broadening due to spatial integration of the luminescence because in these measurements we collected luminescence from the entire trap, including the sides which have higher energy. The second is the fact that our pump laser was a multimode laser with significant fluctuations on nanosecond time scales. This caused a fluctuating shift of the line position which was recorded by our time-integrating detection system as a broadened line.

In conclusion, the lasing transition, in which the carriers are in a plasma state and the photons are weakly coupled to the carriers, and the polariton condensate transition, in which the photons and excitons are strongly coupled to make bosonic polaritons, are clearly distinguishable, even though both lead to emission of coherent light. The polaritonic coherence clearly occurs when the excitonic component of the polaritons is important, as seen by the shift of the lower polariton emission at the threshold with stress to follow the bare exciton state. The Rabi splitting between the upper and lower polaritons remains large, indicating that phase-space filling is not significant. In contrast, the lasing transition occurs when the splitting between the upper and lower polaritons has closed up so that the emission is near the bare cavity photon energy.

The trap plays an essential role in making the polariton condensate transition possible. If there is no trap, only the lasing transition can be seen in these samples. If there is a trap, both transitions can occur. The two transitions can occur at carrier densities which are less than a factor of 10 different. This should not be a surprise because the Mott transition, which in the context of semiconductor physics refers to the transition to an unbound electron-hole plasma, can have a sudden onset. Once a Mott transition occurs, only lasing of a plasma in the weak-coupling regime can occur.

The stress trap used in these experiments appears to reduce the critical threshold for polaritonic coherence enough to move it from above the Mott transition density to below it. As discussed above, the trap has a key role in making BEC possible in a 2D system; in a two-dimensional flat potential, fluctuations will destroy the condensate. Another effect of the trap which may play a role in these experiments is simply that the trap gives the excitons higher density by collecting them in the center of the trap. This effect was enhanced in the

experiments of Ref. [1], where a stiffer spring constant of the trap was used which gave much greater drift force for collecting the polaritons in the center of the trap. While the exciton density can also be increased by simply turning up the pump-laser power, increased laser power also leads to increased lattice heating. The trap helps to produce a colder, denser gas.

3.4 AN ASYMMETRIC TRAP

Some of the first experiments done on atomic BEC were done by confining the atoms in a elongated trap [46]. The equipartition theory for ideal classical gases states that the thermal energy distributes equally among all degrees of freedom with quadratic degrees of freedom. Hence, even in an asymmetrical trap one would expect the momentum distribution of a classical ensemble to be equally distributed among p_x and p_y. The general statement is [67]

$$\langle q_k \frac{\partial H}{\partial q_k} \rangle = \langle p_k \frac{\partial H}{\partial p_k} \rangle = \langle p_k^2 \rangle = k_B T \tag{3.22}$$

where p_k and q_k are generalized conjugate coordinates and $\langle\rangle$ represents the ensemble average. The Boltzmann momentum distribution, which is a Gaussian given by $f(\mathbf{p}) \propto e^{-\alpha(\mathbf{p}\cdot\mathbf{p})}$, implies that the ensemble-averaged momentum distribution would be circularly symmetric in the classical limit. Once the particles behave quantum mechanically as bosons however, the equipartition theorem breaks down and they begin to macroscopically populate the ground state of the trap. The momentum distribution of such a state then exhibits the same symmetry of the ground state of the trap. The effect was first shown by experiments in the elongated traps used by in Ketterle's atomic BEC group [46]. This section is dedicated to our attempts to observe such a clear-cut indicator of BEC of polaritons confined in an asymmetric trap.

Three methods were attempted in the quest to achieve an asymmetric trap for the polariton. The first two methods both employed changing the stress assembly geometry; and both experiments ended in the catastrophic failure of the sample, cleaving it in two.

The first of the two stress methods involved using a pin, of which the head was ground down to be flat, like a cleaver, rather than to a point as before. The error in this method

was due to the fact that the "cleaver" edge of the pin was not perfectly straight or flat and could not contact the sample at all points along its edge, creating large enough shear strains to cleave the sample.

The second method involved bringing a standard round tipped pin in contact above an asymmetrical hole, instead of a round hole like 3.2b shows. The hole was approximately ellipsoidal with the minor axis of the ellipse being comparable in size to the thickness of the sample, and therefore the FWHM of the trap. The alignment of this configuration was difficult because it was almost entirely impossible to see where the pin made contact with the sample. Occasionally the pin would touch down directly over the edge of the ellipse generating a shearing force large enough to shear the sample.

Considering the risks involved in using the above-mentioned strain methods to create an asymmetric trap, a third and quite simple method was exploited instead. Here we rely on the natural gradient of the cavity that was created during the growth of the sample (see the discussion in Section 2.1). When stressing the sample, the strain directly effects the exciton energies, but not the cavity-photon energies. The excitonic trap exhibits cylindrical symmetry; however, the cavity gradient remains unchanged. When polaritons form under these conditions, they feel both the potential from the trap and the cavity gradient. If they are formed with a negative detuning, the polaritons behave more like photons, and are influenced more heavily by the cavity gradient. By creating the stress trap far on the photonic side of resonance, the normally cylindrical confining potential becomes more elliptical because it is stretched out along the cavity gradient direction. Figure 3.11d is a energy contour plot of such a configuration. The cavity gradient in this figure is along the vertical direction.

The experiments were performed in a manner similar to those in the previous section. The polariton gas was created with a Ti:Sapph laser pumping the upper edge of the stop band. The focal spot was approximately 20 μm FWHM and the position on the samples was roughly $\delta = -4$ meV detuned. The BEC threshold densities were achieved with similar excitation powers of around 30 mW. Curves like those in Fig. 3.10 were reproduced and threshold was defined in the same way. Figures 3.11a-3.11c are 2D momentum space plots taken from this density series in the asymmetric trap. Below the threshold, as seen in Fig. 3.11a, the momentum distribution is rotationally symmetric as predicted by the equipartition theorem.

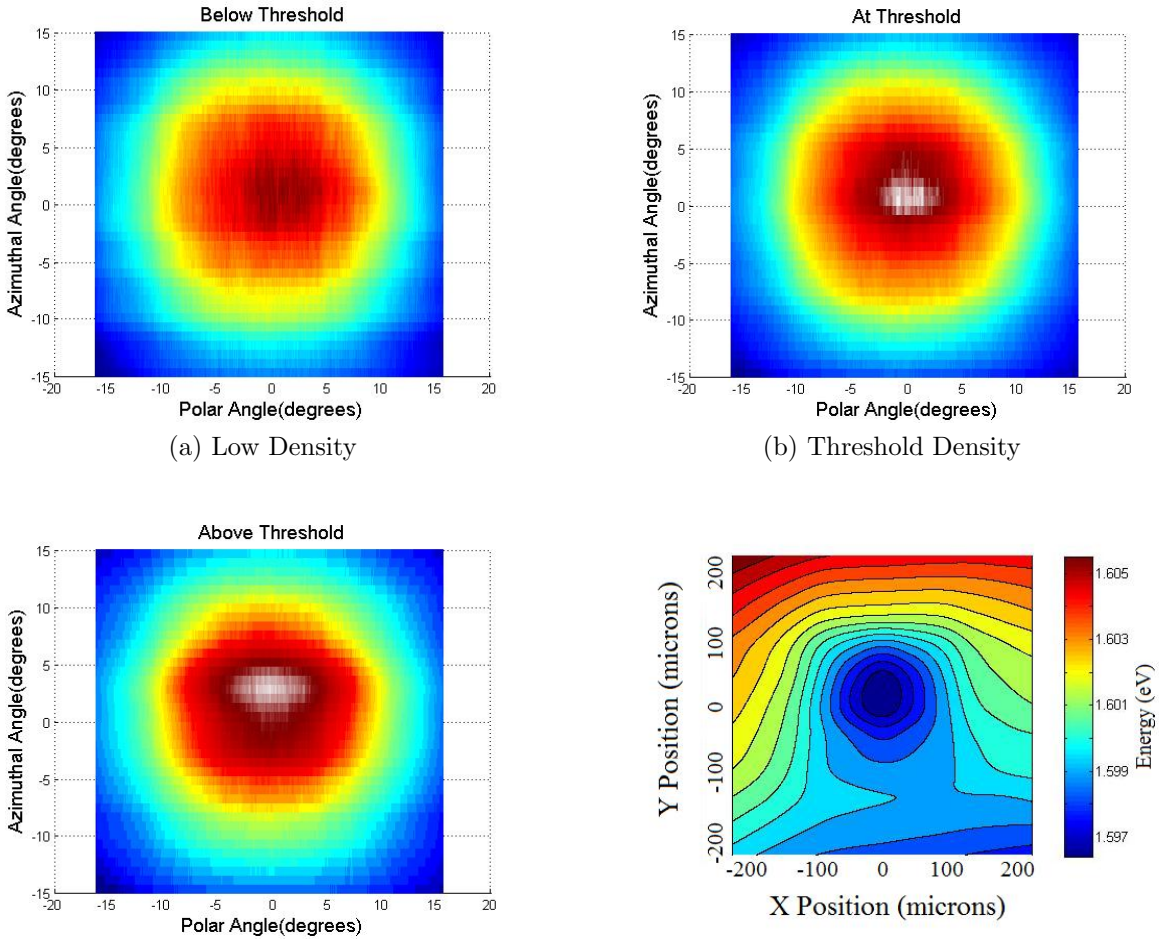

(a) Low Density

(b) Threshold Density

(c) Above Threshold

(d) Asymmetric Trap

Figure 3.11: (a)Below BEC threshold, the gas has a symmetric, 2D momentum distribution as predicted by the equipartition theorem. (b) The condensed fraction of the gas exhibits the symmetry of the ground state of the trap while the uncondensed fraction of the gas still exhibits the cylindrical symmetry in momentum space. (c) Well above threshold density, more polaritons participate in the condensate. There is an odd, unexplained shift in the azimuthal direction of the momentum distribution. (d) Measured 2D energy contour of the confining potential used in cases (a)-(c).

As the density is increased to the BEC threshold density, the nature of the momentum-space distribution changes, as seen in Fig. 3.11b. The color scale was enhanced to show that the background, uncondensed fraction of the gas still exhibits the same symmetry, while the Bose-condensed, white portion of the figure shows that it takes on the predicted momentum-space distribution one would expect for the given asymmetric trap. Figure 3.11c is a image of the highest-density momentum distribution that shows the same thing as Fig. 3.11b, but with a larger population in the condensate. However, there is a yet unexplained, overall shift of center of the distribution to a non-zero azimuthal momentum. This could possibly be explained by a net flow to lower energy of the polaritons in the trap due to pumping slightly off center.

4.0 BOSE CONDENSATION OF LONG-LIFETIME POLARITONS

Up to now the lifetime of the particles at low momentum and zero detuning in these experiments has been 1-2 ps [1, 3, 2, 4, 7, 10, 11], comparable to or just slightly longer than the collision time between the particles, which has led to the description of these systems as "nonequilibrium condensates". Here I report on experiments with new structures with extraordinarily long-lived polaritons. With lifetimes of over 100 ps, more than an order of magnitude longer than previously reported lifetimes, the particles live much longer than their average collision time and can come much closer to thermal equilibrium. At high density we see a sharp transition which is similar to the discontinuous behavior of a true equilibrium phase transition in the thermodynamic limit.

An additional motivation behind these new structures is that if the lifetime increases, then the density will increase proportionally (ignoring additional drift and diffusion.) The rate of population change can be modeled as

$$\dot{n} = -\bar{\Gamma} n + G, \tag{4.1}$$

where n is the polariton density, $\dot{n}$ is the time derivative of the density, $\bar{\Gamma}$ is the average decay rate of the polaritons, and G is the gain, given by the pumping rate. Ignoring condensation effects, the pumping rate is proportional to the laser excitation power. Solving this equation for steady-state gives

$$n_{\mathrm{s}} = \bar{\tau} G, \tag{4.2}$$

with the average polariton lifetime given by $\bar{\tau} = 1/\bar{\Gamma}$. Notice that for a laser with a fixed power, we can increase the polariton density by increasing the lifetime. Table 4.1 shows a comparison of the new microcavity samples to the old ones used in the aforementioned

experiments.

4.1 EXCITON-RESERVOIR TRAPPING AND BOSE CONDENSATION

Although 100 ps may also seem like a very short time, the absolute time scale is not important; what matters in any system is the ratio of the lifetime of particles to the collision time between the particles. When the lifetime is much longer than the collision time, equilibrium statistics apply to a very high degree of approximation. This is the case for atomic condensates [68], in which the atoms have a lifetime in the system of a few seconds, compared to typical interaction times of milliseconds. In past experiments with polariton condensates, the rate of collisions has been limited by an upper bound of the density of the polaritons; their density is limited by a Mott transition at high density to uncorrelated plasma [69, 70]. Numerical calculations [71] have shown that at densities below the Mott transition, the onset of high occupation of the polariton ground state seen in the experiments occurs due to the bosonic nature of the particles. While many of the canonical effects of Bose-Einstein condensation or superfluidity can be observed, the fact that the lifetime is not extremely long compared to collision time is probably the main reason that the discontinuous behavior associated with an equilibrium phase transition in the thermodynamic limit has not been seen. In particular, the onset of the transition has followed an"S-curve" (Fig. 3.10a) which resembles very closely the emission versus pump power for a standard laser (Fig. 3.9a). By contrast, the new results which I report, shown in 4.4a, have a completely different behavior, with two nonlinear regions.

The only difference between our new structures and the old structures is that the cavity formed by the distributed Bragg reflectors used to make the microcavities now has a quality factor (Q) of around 10^6, with a calculated cavity lifetime of 400 ps. Our previous experiments used a structure which was identical in design to this one, but with half as many layers in the DBR mirrors. The calculated cavity lifetime for that structure was 1.5 ps, with a Q of 4800. The high Q calculated for our new structure is also confirmed by the width of the lower polariton reflectivity peak, which is narrower than our instrumental resolution of 0.05

Original Cavity	Redesigned Cavity
DBR	DBR
Front: 16	Front: 32
Back: 32	Back: 40
Reflectivity	Reflectivity
Front = 0.98858	Front = 0.99987
Back = 0.99646	Back = 0.99999
Q factor	Q factor
Q = 4800	Q = 1×10^6
Cavity Lifetime	Cavity Lifetime
$\tau = 2$ ps	$\tau = 400$ ps

Table 4.1: Left Column: Simulated original optical cavity parameters based on transfer-matrix calculations. Right Column: Simulated redesigned optical cavity parameters based on transfer-matrix calculations.

nm. The lifetime of the polaritons in the new structure is at least 100 ps, as determined by the methods described in Chapter 5.1. Since everything else in the structures is the same as in the older samples, the difference in the curves in Fig. 3.10a and 4.4a, discussed below, can not be related to increased volume, which can lead to a sharper transition onset in standard lasers.

Figure 4.1 shows momentum space distributions of the polaritons at three densities, obtained by angle-resolving the photon emission from the polaritons, as discussed in Section 2.2.2. In this case the polaritons are generated on the photonic side of the resonant spot of the sample, but close enough to resonance that they have a significant excitonic component and a large shift from the cavity photon energy; the upper dot-dashed curve shows the calculated energy of the bare cavity photon. The solid parabola gives the unrenormalized dispersion of the polaritons according to $E = E_0 + (\hbar\mathbf{k})^2/2m$, where $\mathbf{k}_\parallel$ is the in-plane momentum of the polaritons and E_0 is the low-density, zero-momentum energy of the resonance.

Because the thickness of the sample changes with position, this gives rise to an effective potential gradient. This is due to the in-plane cavity mode energy changing with cavity thickness, as discussed in Section 2.1. Over the small ranges we are focusing on, this force $(-\partial U/\partial x)$ is relatively constant. This potential gradient, therefore produces an acceleration of the polaritons such that, $\partial\mathbf{p}/\partial t = -\partial U/\partial x \approx 13$ meV/mm, as measured from Fig. 4.2a.

As seen in Fig. 4.1a, the cold polaritons at the very bottom of the momentum distribution show a distinct tail to the right. This corresponds to acceleration to higher momenta at the same energy, trading potential energy for kinetic energy. In Fig. 4.1b, we see that this constant-energy tail becomes dominant at higher polariton density. We interpret this constant-energy tail as the accumulation the polaritons in a single, coherent energy state due to the bosonic nature of the polaritons, which becomes more important at high density.

The momentum-space profile seen in Fig. 4.1b is consistent with numerical solution of a Gross-Pitaevskii equation [72, 73] for a polariton condensate when polariton-polariton interactions are negligible[1], effectively solving the single-particle Schrödinger equation. The potential profile used for this numerical solution is shown as the dotted line in Fig. 4.2a, and the real-space solution is shown in Fig. 4.2c, for a series of particle lifetimes. Although there

[1]These calculations were done by Mark Steger at the University of Pittsburgh.

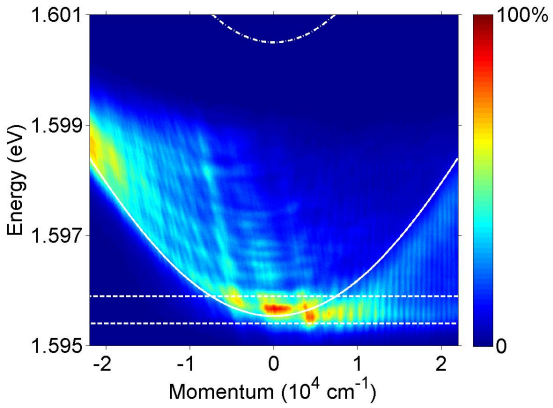

(a) Below Threshold

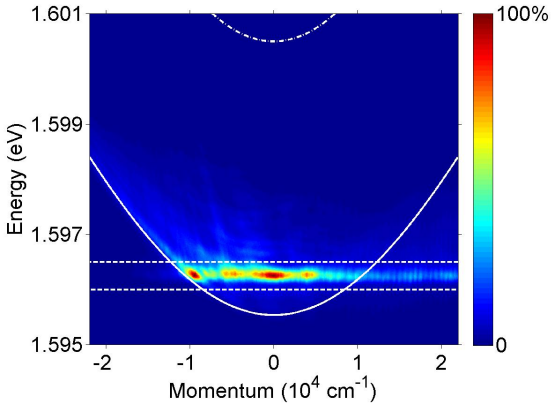

(b) Bose-enhanced

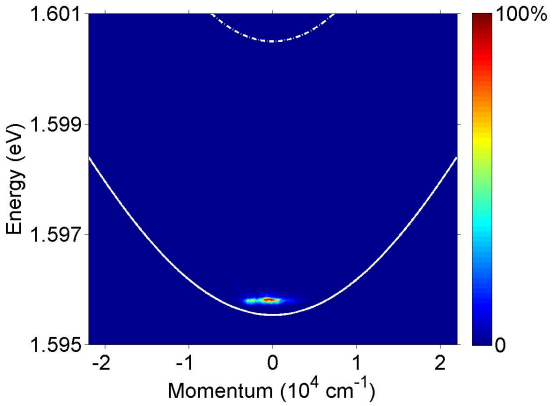

(c) BEC

Figure 4.1: (a) Intensity of the polariton photon emission for polaritons at low density (3 mW in a laser spot diameter of 10 μm) as a function of momentum and energy. (The fringing is an artifact of the detection system.) The laser excitation spot in this case was slightly to the photonic side of the resonant point on the sample. The solid parabola is the polariton dispersion relation. The smearing of the distribution toward the right corresponds to the average momentum gained by the particles in their downhill motion. The dot-dashed parabola is the bare cavity photon dispersion; the horizontal dashed lines give the spectral range of integration for the data of Figs. 4.4 (b). (b) The same plot when the polaritons are at moderately high density (45 mW in a laser spot diameter of 10 μm). The polaritons are sucked into a single state at constant energy. (c) The same plot for slightly higher excitation density (48.5 mW in a laser spot diameter of 8 μm.)

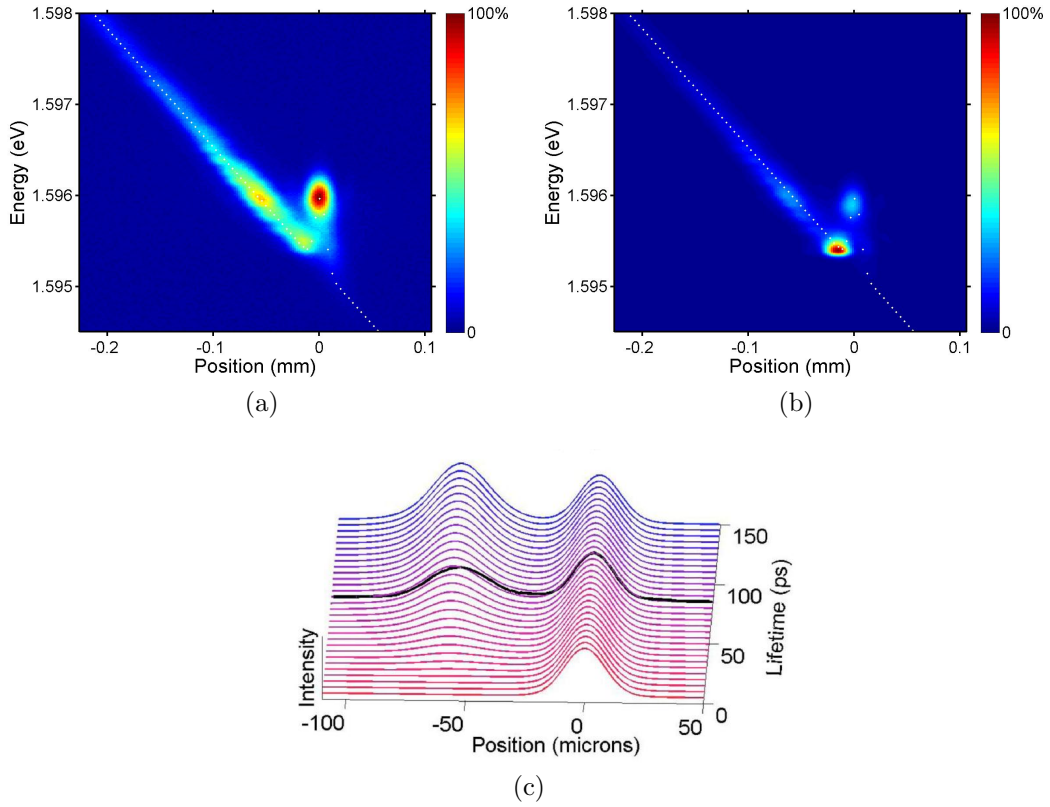

Figure 4.2: (a) Real-space image of the $\mathbf{k}_{\|} \approx 0$ emission near the laser spot, at high excitation density (48.5 mW in 8 μm diameter laser spot). Dotted line: Model of the potential energy profile felt by the polaritons at high density. The slope comes from the gradient of the cavity width, while the peak comes from the exciton cloud centered at the laser excitation spot, which repels polaritons. The exciton cloud is nearly static compared to the speed of the polaritons. (b) The same as (a) but for a location in closer to the center of the laser excitation spot. The intensities of (a) and (b) are normalized; the upper two spots in (b) correspond to the same absolute intensity as the upper two spots in (a). (c) Thin lines: the time-averaged square of the intensity of the wave function at $\mathbf{k}_{\|} \approx 0$ for the solution of the time-dependent, one-dimensional Schrödinger equation in the potential profile shown as the dotted line in (a), for a series of different polariton lifetimes. Heavy black line: the intensity profile of the data of (a) along a line of constant energy at 1.596 eV.

are phase fluctuations in the polariton state of Fig. 4.1b, as evidenced by the finite spectral width, a Gross-Pitaevskii solution is still valid for the collective wavelike behavior of the polaritons. The potential profile used for the model, shown as the dotted line in Fig. 4.2a, has a peak in the potential energy at the point of laser excitation. This is because the laser creates an exciton cloud, which I can call the exciton "reservoir", in addition to the polaritons. The excitons have much higher mass, about $0.3m_e$, so that within their lifetime they can only drift a few microns; they are essentially static as seen by the polaritons which have nearly four orders of magnitude lighter mass. The excitons in this quasi-static reservoir repel the polaritons, leading to a positive potential. This picture of the exciton cloud as a static potential barrier as seen by the polaritons has been demonstrated in previous experiments with polaritons in GaAs microcavities [74, 75, 76, 77, 78]. This positive potential is seen in the blue shift of the polaritons in Fig. 4.1b relative to their energy position at low density in Fig. 4.1a. The exciton cloud effectively makes a uni-directional trap for the polaritons, Fig. 4.2a, with the exciton cloud as one barrier and the cavity gradient as the other barrier. The data of Fig. 4.2a shows the spatially-resolved photon emission from the polaritons at

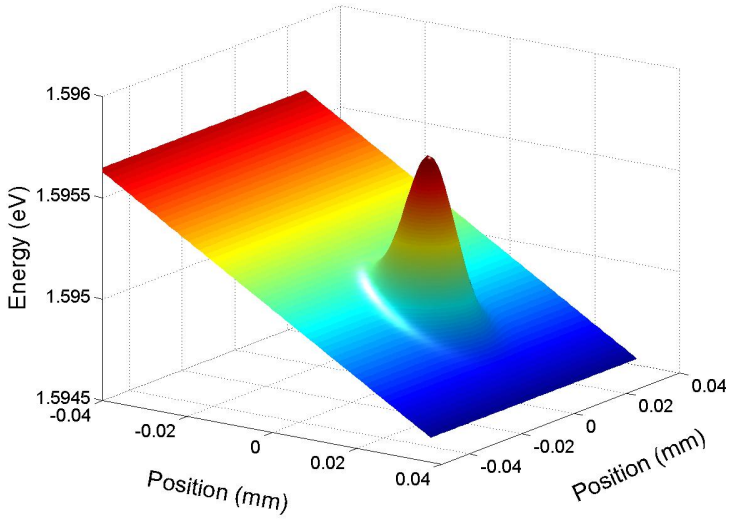

Figure 4.3: 2D real space potential profile felt by the polariton superfluid. The potential bump is due to the exciton reservoir, while the overall slope is due to the cavity gradient. Extrapolated from the same parameters as found in Fig. 4.2a

high density under similar conditions as those for the data of Fig. 4.1. As seen in Fig. 4.2a, when the potential energy barrier due to the exciton cloud is high, corresponding to high laser excitation power, the wave function has two distinct peaks at the same energy, which correspond to the turnaround points of a coherent mode oscillating in the uni-directional trap. Fig. 4.2c shows a series of solutions of the time-dependent Gross-Pitaevskii equation in steady state with polariton generation and decay, for the potential energy profile shown in Fig. 4.2a and generation of polaritons at the laser excitation spot. As seen in Fig. 4.2c, the fits of this theory to the data are sensitive to the lifetime of the polaritons; these curves indicate a lifetime of 85±5 ps. (This overall lifetime includes not only radiative decay but also depletion of the condensate due to motion in the perpendicular direction.) The same simulation gives a momentum-space distribution which extends to $\mathbf{k}_{\|} \approx -10^4$ cm^{-1}, consistent with the spread in momentum space seen in Fig. 4.1b. The spread in momentum is driven by the initial acceleration away from the point of creation of the polaritons, i.e., toward the left, with a potential drop of about 0.85 meV over a distance of about 5 μm. In the rightward direction, the particles continue to accelerate to higher momenta until they decay.

The remarkable thing about this high-density behavior is that the polaritons in the tail are in a single energy state despite the complications of the trap potential created by the tilted potential with a local maximum. This is seen both in the k-space data of Fig. 4.1b and in the spots at equal energy in real space for the $\mathbf{k}_{\|} \approx 0$ data of Fig. 4.2a. This indicates that the polaritons are acting as a single coherent wave function, with an increasing fraction of the particles in this state as density increases, as expected for a weakly interacting Bose gas. Acting as a single wave function which is robust against scattering processes is the hallmark of superfluidity. Although a true Bose-Einstein condensation phase transition is not possible in two dimensions, it is well known [59, 60] that superfluidity can occur, with phase fluctuations.

More remarkably, at higher density, a dramatic jump to a single-energy state at the bottom of the trap occurs. Fig. 4.1c shows k-space data at the highest excitation density we can create with our stabilized diode laser. Over a very narrow excitation-density range, the emission from this mode increases to dominate the total luminescence of the system.

The spectral width of this mode is limited by the resolution of our detection system. The energy of this state is lower than that of the state shown in Fig. 4.1b, and corresponds to the energy of a trapped mode, shown in Fig. 4.2b. As seen in this figure, the bright emission at high density does not come from the laser excitation spot; it comes from a region about 10 μm to the left, at the energy minimum of the uni-directional trap created by the wedge of the cavity and the exciton cloud. The fact that the energy of this emission is lower than the energy of the emission at lower pump powers shows that this emission is not standard lasing–as we and others have shown earlier [4, 10], standard lasing has been shown to occur in these structures at the cavity photon mode, which is much higher in energy, as indicated by the dot-dashed line in Fig. 4.1c.

As seen in Fig. 4.4a, the new data shows three regimes: a low density regime in which the particles act entirely as a classical gas, a middle regime in which Bose stimulated scattering gives enhanced occupation of the polariton states, and a third regime in which the the polariton gas jumps into a very coherent state with dramatically higher occupation. Figure 4.4c shows that the coherence of the polariton emission changes in a dramatic way when this upper transition occurs. Fig. 4.4b shows the fraction of the total emission from the polaritons in the ground state as a function of the laser excitation power. At the same threshold at which this occurs, the luminescence peak narrows dramatically, as shown in Fig. 4.4c. Spectral narrowing of the luminescence peak indicates increased coherence, according to the W-K theorem [16]. At high power the line width narrows to the limit of our spectral resolution. As discussed above, the nearly discontinuous behavior seen here is in sharp contrast to the smeared-out transition seen in previous high-density polariton experiments [3, 1, 79, 74] with much shorter particle lifetime; those experiments typically show an S-like onset curve with pump power spread over a factor of 2 or 3 for the transition, similar to that of a laser [80], as opposed to the sharp transition over few percent change of excitation density seen here. Because of the much longer lifetime in our structure, a transition which is much more akin to a true phase transition can occur. The total system is not in equilibrium, since there is a source, decay, and hydrodynamic flow out of the source region, but locally, the polariton gas can be much colder and more in equilibrium, since the particles can thermalize by scattering with each other and by phonon emission over much longer times.

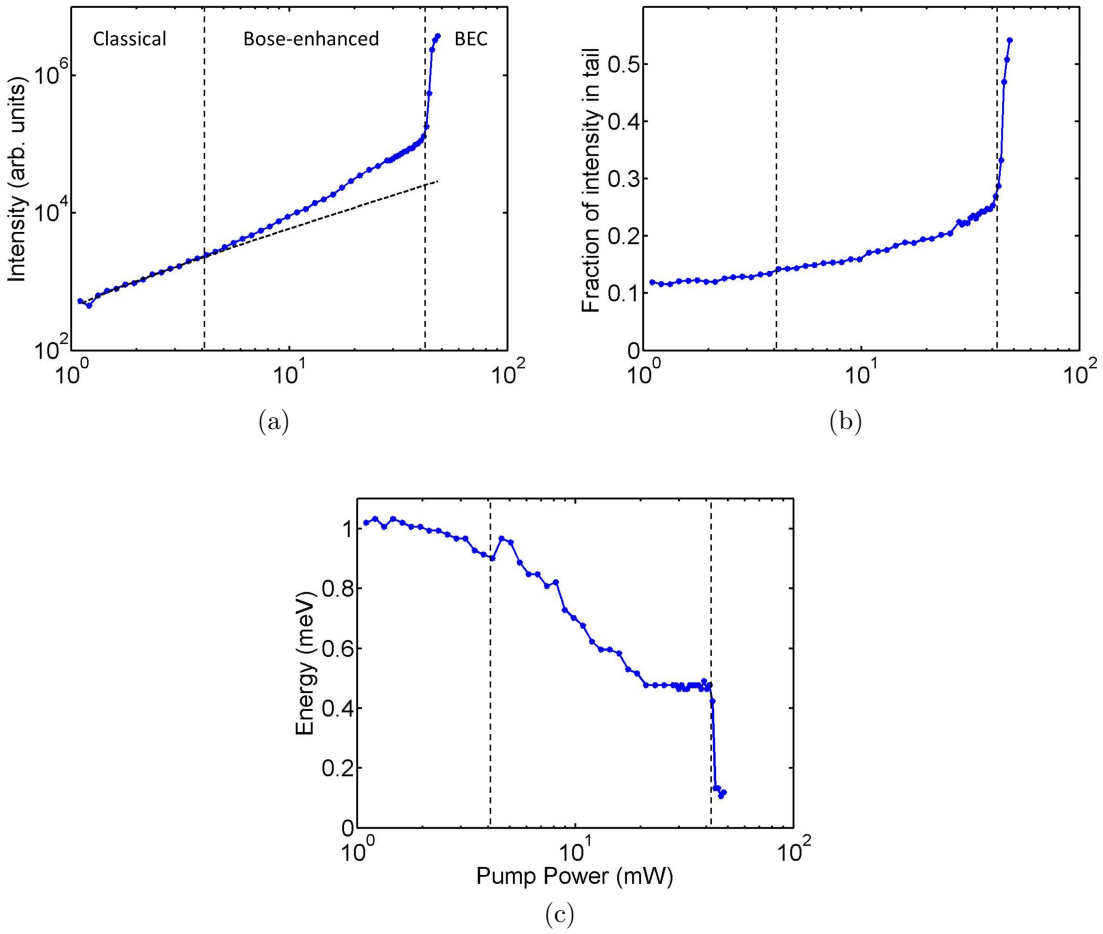

Figure 4.4: (a) Intensity of the photon emission peak at $\mathbf{k}_{\|}$(emission normal to the surface of the sample) as a function of excitation power, for a laser spot size of 8 μm diameter. Thin dashed line: linear dependence (slope = 1 on the log-log plot). (b) The total fraction of luminescence contained in a spectral range of 0.5 meV centered on the wavelength of the peak emission intensity, integrated over the same range of momenta as in Fig. 4.1, for the same data as used for (a). (c) The FWHM of the spectral peak, from the same spectra as used for (a). The spectral resolution for the experiment was 0.1 meV. The vertical dashed line in each case indicates the threshold pump power.

We interpret the middle density range as a regime in which Bose effects change the behavior of the polaritons, leading to nearly a single energy as seen in Fig. 4.1b, but not a true condensate. The existence of this regime is also in contrast to earlier experiments with short-lifetime polaritons which, as seen in Fig. 3.10, show linear behavior up to the threshold power at which increased coherence occurs. In the high-density regime seen here, the polariton gas much more resembles a true condensate with a strong degree of coherence.

Coherence times much longer than the lifetime of the polaritons have been reported in Ref. [45] presumably due to a collective phase memory of the polariton condensate. The structure discussed here may allow even longer coherence times. This opens up new physics in which the lifetime is much longer than the scattering time, so that drift can take the polaritons well away from the excitation region, and the coherence length of a superfluid can be long compared to the size of a trap. To do these measurements we plan to create a spatially confining trap for the polaritons in order to have an equilibrium density profile.

4.2 PERSISTANT PATTERNS IN LONG-LIFETIME POLARITON SAMPLES?

An interesting phenomenon associated with superfluidity is the possibility of the formation of persistent vortices. In polariton gases, vortices have been studied [39, 81, 82, 83, 84], but because of their small size of roughly 1 μm, spontaneous vortices are rarely imaged directly. Instead, a commonly used technique is to measure vortices through interferograms. Imagine instead, that a vortex which is small in real space, becomes large in momentum space. With vortices on the order of 1 μm in diameter, the wavevector length scales should be of the order of $1 \times 10^4\ cm^{-1}$ (from $\Delta x \Delta k \approx 1$.)

This may be the case in the 2D k-space images taken under the same conditions as the previous section's experiments with the long-lifetime samples. Figure 4.5 shows the 2D momentum-space distribution taken at different times, with the only experimental difference being variations such as pump-intensity fluctuations (these should be minimal since we are using a stabilized laser as discussed in Section 2.3) and temperature fluctuations. The amazing fact is that each of these pictures was taken with a 3 ms CCD integration time compared to single-polariton lifetimes of 100 ps. That indicates that the exhibited patterns are stable over at least 3 ms. The excitation densities were the same as those taken in Figs. 4.2b and 4.1c. The intensity is log scale to enhance the PL at high k, showing the polariton accelerating down the cavity's potential gradient.

One might imagine that this k-space pattern is caused directly by the excitation laser imprinting its far-field information onto the polaritons. However, this can be ruled out because we are pumping well above the edge of the stop band in energy, and also with a large in-plane momentum. In order for the carriers to cool down into the lower polariton branch, they must first emit over 160 meV of energy. Since this must be done through multiple collisions, or through the emission of phonons, any initial momentum distribution inherited from the laser should lost; and we see that this is indeed the case for the low density polariton distribution (see Fig. 4.1a).

Another hypothesis is that these states are simply laser modes with the far-field patterns similar to those of a cavity with cylindrical geometry. We know this is not the case. The

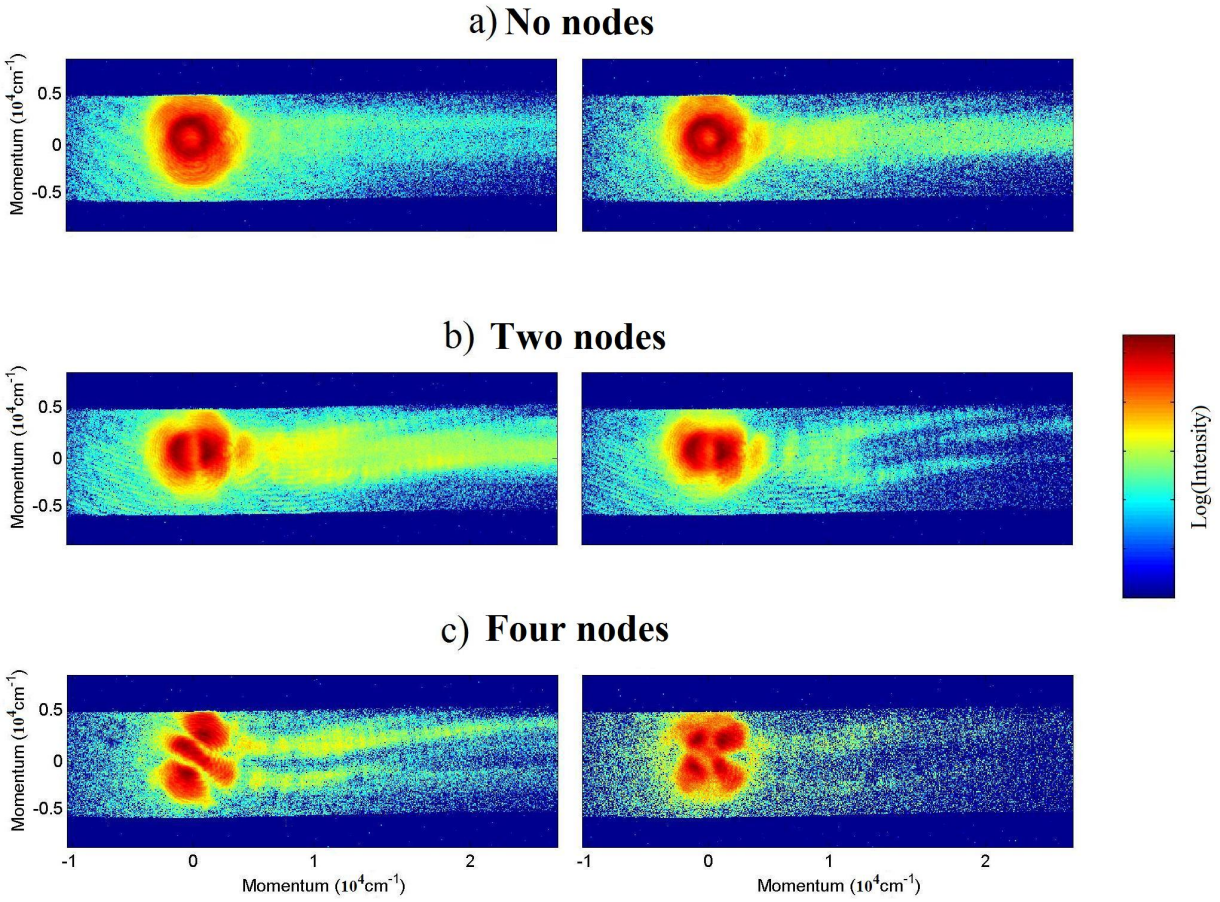

Figure 4.5: 2D Momentum Space images taken under the same conditions as 4.2b and 4.1c. (a) Momentum distribution corresponding to no nodes. (b) Momentum distribution wit two nodes. (c) Momentum distribution with four nodes.

polaritons cannot be thought of as lasing since the polariton luminescence is coming from a region of the sample where there is no population inversion, away from the exciton reservoir (see Fig. 4.2b). Secondly, our system does not exhibit the cylindrical geometry required to generate such modes. Figure 4.3 shows the full 2D potential that the polaritons experience. The luminescence is produced at the saddle point between the exciton reservoir potential and the cavity gradient; it is yet to be understood why there is a collection of particles in such a potential. The potential at this point clearly lacks the 2D cylindrical symmetry necessary to produce these types of far-field luminescence patterns.

Instead, as Fig. 4.5 is labeled, these k-space distributions may be due to a single vortex [39], or vortex-antivortex [81] bound pairs. A simple model of the calculated real-space and momentum-space distribution are shown in Fig. 4.6, for a wave function associated with a vortex-antivortex pair given by

$$\Psi(\mathbf{x}) = \sqrt{n(|\mathbf{x}-\mathbf{x_1}|)}e^{i|m|\theta} + \sqrt{n(|\mathbf{x}-\mathbf{x_2}|)}e^{-i(|m|\theta+\phi)}, \tag{4.3}$$

where n is the density that describes a vortex core, x_1 is the position of the first vortex, x_2 is the position of the second vortex, or antivortex, m is the winding number, and ϕ is an overall possible phase difference. The 2D XY model can be used to derive that vortices of opposite winding number are attractive and, below the K-T transition temperature, thermally favor vortex-antivortex bound states [37]. Then, if $x_1 \approx x_2$ as for a tightly bound pair, $|\Psi|^2$ becomes a standing wave in the polar angle θ, ($|\sin(\theta)|^2$), with two antinodes. When a vortex-antivortex bound state of winding number 2 forms, the resulting $|\Psi|^2$ is a standing wave with 4 antinodes. An overall relative phase ϕ rotates the standing wave pattern in coordinate space by $\phi/2$. These deviations in angle can be seen in Fig. 4.5 too. The following simple, qualitative function was used to model $n(r)$:

$$n(r) = Ae^{-\frac{(r-r_0)^2}{2\sigma^2}}, \tag{4.4}$$

where r_0 approximately represents the radius of the vortex and σ produces the size of the wave function. This approximation gives a single vortex that has a distribution in real space like Fig. 4.6a. This oversimplified vortex-antivortex pair calculation (Eq. (4.4) inserted into Eq. (4.3)) reasonably reproduces the momentum-space patterns observed in Fig. 4.5.

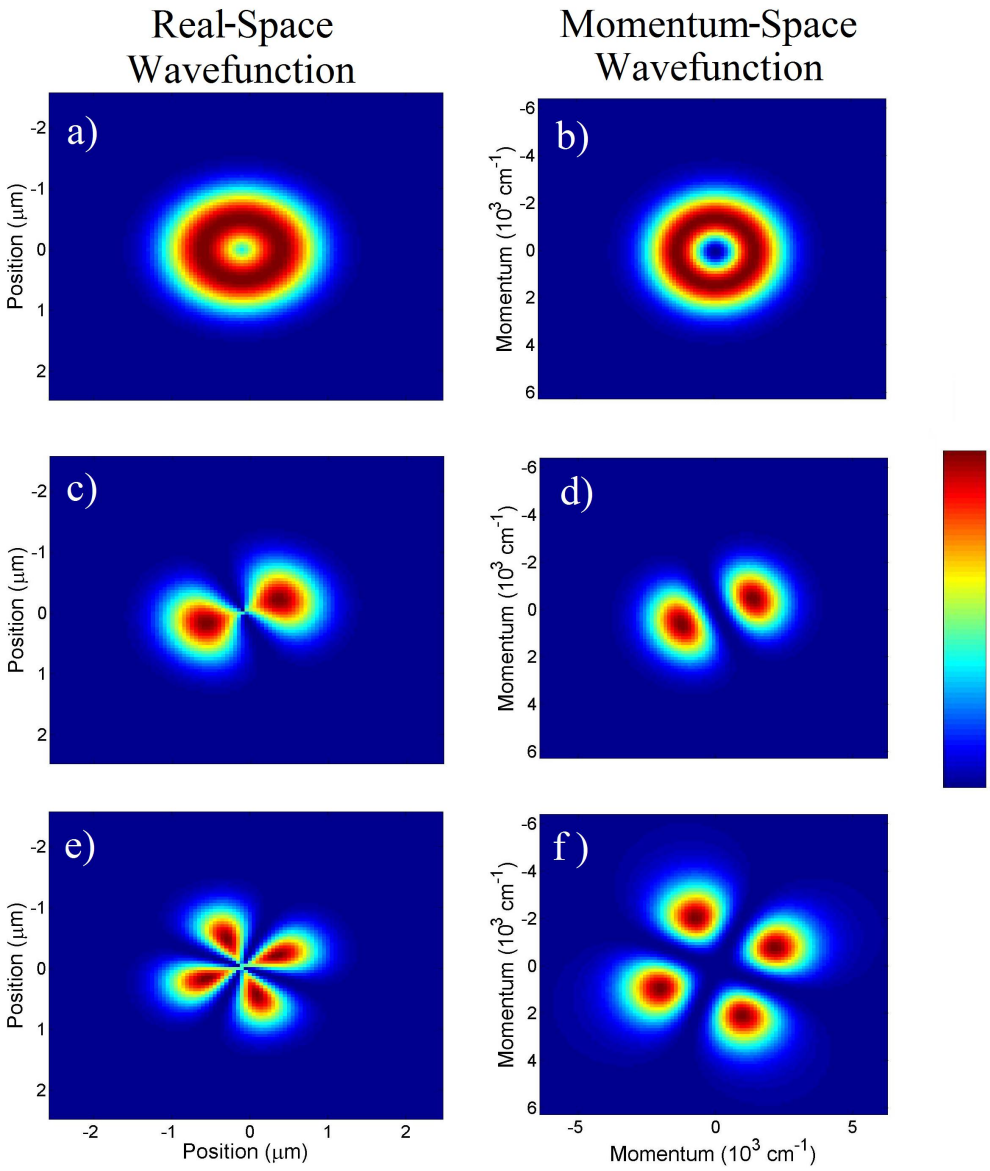

Figure 4.6: Calculated 2D real-space and momentum-space images reproducing 4.5. Column 1) Real-space wave function. Column 2) Momentum space wave function. (a) and (b)Single vortex. (c) and (d) Bound vortex-antivortex pair with winding number $m = 1$. (e) and (f) Bound vortex-antivortex pair with winding number $m = 2$. The bound vortices were modeled by Eq. (4.4) and were spatially separated by the diameter of their core, 0.2 μm.

One may also imagine that this phenomenon is simply a beating between two modes spaced very close in energy. This speculation leads to a very interesting conclusions. The intensity of two beating modes would be proportional to $\cos((\Delta\omega t)e^{-\Gamma t}$. First, there must be at least a 3 ms beating time ($2\pi/\Delta\omega$) between modes because this was the integration time taken for each k-space image. These beating modes must come from the unconfined dimension of the reservoir trap because the mode spacing in the confined direction has a 50 μeV level spacing, giving a 20 ps beating frequency. This also implies that there must be a relatively long decay time of the manybody wave function since the polariton lifetime is at most 300 ps, or over 7 orders of magnitude smaller than the measured decay times, and the images strongly show a definite profile. This implies that the coherence of the polariton gas is maintained through the polariton-polariton interaction, which is another indicator of BEC.

More investigations are still needed to determine the origin of these long lived k-space patterns.

5.0 LIFETIME, DRIFT AND DIFFUSION WITH LONG-LIFETIME POLARITONS

5.1 LIFETIME

We were interested in a precise measurement of the polariton lifetime in the redesigned microcavity. Polariton lifetime measurements from the long-lifetime samples are well suited for measurements on the streak camera since they are predicted to have a lifetime on the order of 100 ps.

These measurements were achieved by collecting PL from a small range of angles about the normal, corresponding to $k = 0 \pm 3°$. The samples were pumped with a Ti:Sapph laser configured to produce pulses of 5 ps and tuned very near to the lower polariton energy. To avoid direct reflection of the pump laser back into the streak camera, the pump laser was incident on the sample at an angle of 5°. This meant, however, that we were exciting polaritons at a different momentum than we were measuring, so the polaritons first needed thermalize before the emission could be detected. A full thermalization calculation [85] would be required to extract the exact lifetime data from these measurements, but a two-state lifetime model was used for an approximate solution.

$$\begin{aligned} \dot{n_1} &= -\bar{\Gamma}_1 n_1 \\ \dot{n_0} &= \bar{\Gamma}_1 n_1 - \Gamma_0 n_0 \end{aligned} \tag{5.1}$$

.

Here, n_1 is the density of the pumped state, n_0 is the density of the ground state, $\dot{n}_i$ is the time derivative of the density n_i, $\bar{\Gamma}_1$ is the average rate to scatter from the initial state

into the ground state and Γ_0 is the decay rate of the ground state. These equations can be integrated in closed form with the solutions

$$
\begin{aligned}
n_1(t) &= n_1(0)e^{-\bar{\Gamma}_1 t} \\
n_0(t) &= \frac{\bar{\Gamma}_1}{\bar{\Gamma}_1 - \Gamma_0} n_1(0) \left(1 - e^{-(\bar{\Gamma}_1 - \Gamma_0)t}\right) e^{-\Gamma_0 t}
\end{aligned}
\tag{5.2}
$$

,

with the initial condition $n_0(0) = 0$. The intensity measured by the streak camera is given by measuring the photons/second emitted from the ground state, or $\Gamma_0 n_0$. The results of these measurements are shown in Figs. 5.1 and 5.2.

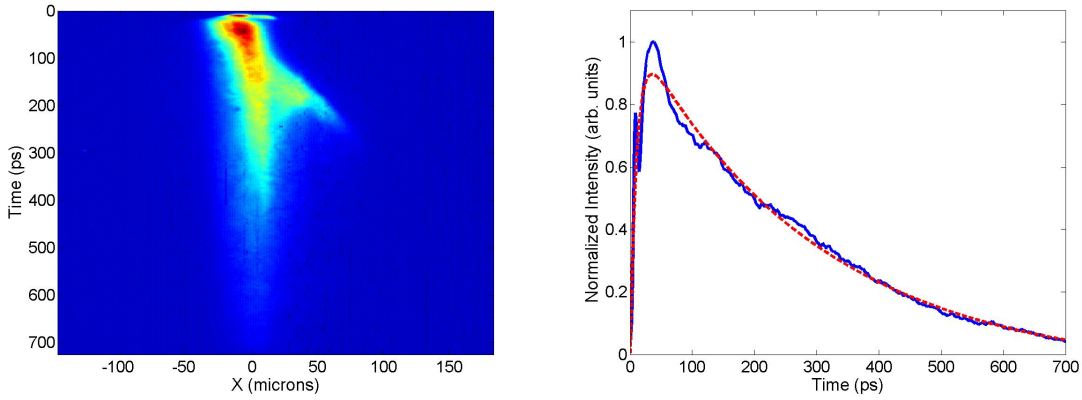

(a) (b)

Figure 5.1: (a) Time-resolved streak camera measurements of the lower polariton, $k = 0$ luminescence on the excitonic side of resonance. (b) Three parameter fit ($\bar{\Gamma}_1$,Γ_0 and $n_1(0)$) to the data in (a) using the model (5.2). The fit lifetime was 297 ps. The small peak near $t = 0$ is scattered laser light. This was used to set $t = 0$. In this picture the scattered laser light was slightly clipped by the field of view of the streak camera. The down-scattering time, $\tau_1 = 1/\Gamma_1$, from Eq. (5.2) was 10 ps.

Since the lifetime is given by the weighted fraction that the polariton is excitonic and photonic (see Eq. (1.29)), the lifetime changes with detuning and temperature. Figure 5.1 shows the time-resolved luminescence taken from a part of the sample where the lower

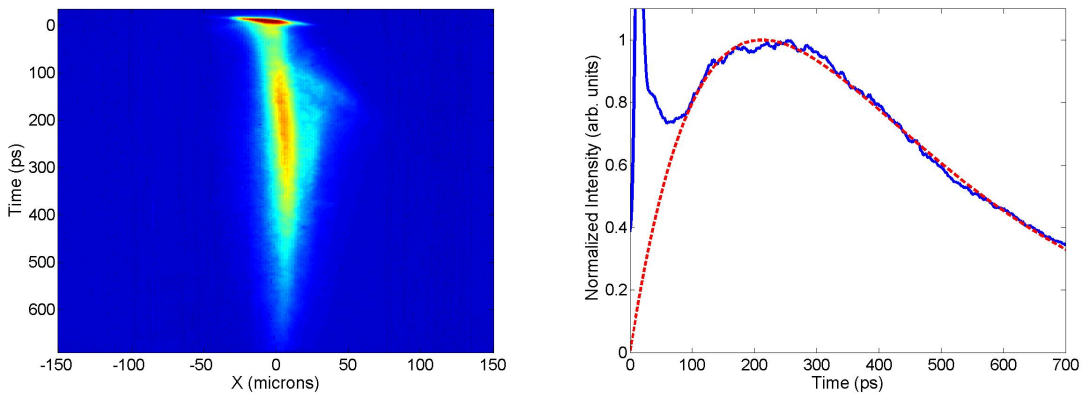

(a) (b)

Figure 5.2: (a) Time-resolved streak camera measurements of the lower polariton, $k = 0$ luminescence on the photonic side of resonance. (b) Three parameter fit ($\bar{\Gamma}_1$,Γ_0 and $n_1(0)$) to the data in (a) using the model (5.2). The fit lifetime was 211 ps. The tall peak near $t = 0$ is scattered laser light. This was used to set $t = 0$. The down-scattering time, $\tau_1 = 1/\Gamma_1$, from Eq. (5.2) was 212 ps.

polariton is more excitonic. The lifetime is longer than that of Fig. 5.2 where the lower polariton is more photonic. The two-level model that we used to fit the data is somewhat insufficient to describe the data even though the model fits the data relatively well. The time $t = 0$ was deduced from the measured scattered light that is visible in the upper portion of the luminescence in Figs. 5.1 and 5.2. Also, one can qualitatively note from these figures that the rise time for the photonic case is longer than for the excitonic case, which is intuitive because when polaritons are more excitonic, they will thermalize faster, thereby scattering into the ground state of the system faster than the case where the lower polaritons are more photonic. These measured lifetimes will be longer than the actual polariton lifetime since some of the polaritons can scatter up into the reservoir where their decay lifetime is much longer than the lifetime.

The average lifetime of the polaritons in a Maxwell-Boltzmann distribution is given by

$$\frac{1}{\tau} = \frac{1}{\tau_{\text{phot}}} \int e^{-(E-E_0)/k_B T} C^2(E) D(E) dE, \tag{5.3}$$

where τ_{phot} is the cavity photon lifetime, $C(E)$ is the Hopfield coefficient giving the fraction of the polariton state which is photonic, and $D(E)$ is the density of polariton states at energy E. $C(E)$ and $D(E)$ are calculated knowing the Rabi splitting of the polaritons and the cavity photon dispersion relation, assuming the excitons have constant energy. This calculation assumes that the excitons have negligible decay rate, which as discussed in earlier, is valid when the polariton lifetime is much less than 400 ps.

In Ref. [1], the cavity photon lifetime was 2 ps, which gave an average polariton lifetime of 16 ps at the effective temperature of the polaritons of 30 K. The average lifetime is longer than the cavity lifetime because the radiative rate of higher-k states drops due to their decreased photonic component, when the $k = 0$ state is at resonance.

5.2 DRIFT AND DIFFUSION

Away from the resonant point, on the negative detuning side, the lower polariton state becomes increasingly like a pure photon state, while on the positive detuning side, the lower

polariton state becomes increasingly like a pure exciton state. The shift of the lower polariton energy with detuning due to the gradient in the cavity width gives a spatial gradient of the potential energy felt by the polaritons. Figure 5.3 shows data from when the polaritons are created at a spot on the sample well on the photon-like side of the resonance (the upper image in Fig. 5.3a shows the profile of the excitation region). The spatial drift of the luminescence seen in this figure is at first surprising: the polaritons appear to drift uphill, to higher energy, also for hundreds of microns; uphill motion more than 1 mm has been observed in this structure.

This "uphill" motion can be understood if we recall that the laser which generates the polaritons is tuned to a photon energy well above the highest-energy polariton states; free electrons and holes are generated at very high kinetic energy and then lose energy by phonon emission, eventually entering the exciton and polariton states. Therefore polariton states with a broad range of momenta are occupied near the laser excitation spot. Some of these polaritons drop down to lower energy by phonon emission and polariton-polariton scattering, but some propagate in the plane, outward from the laser excitation spot. Those with momenta pointing in the direction of the uphill gradient of potential energy will trade their high momentum for higher potential energy until they eventually hit a place where the cavity photon energy exceeds their initial energy, and they have no more momentum to give up, as illustrated in Fig. 5.4. At this point of zero momentum, they couple into photons emitted normal to the cavity. These escaping photons are what we record for the data shown in Fig. 5.3b. Polaritons also travel downhill, but in this strongly photon-like region, they do not scatter down into low-momentum states which can emit photons detected by our real-space imaging system; only the exciton component of the polaritons gives a deformation-potential interaction with lattice phonons or elastic scattering with other polaritons.

This uphill motion of strongly photon-like polaritons is therefore essentially the same as photons created by a white light source and propagating in a high-quality wedged cavity. In the absence of significant scattering, photons in a wedged cavity will propagate with slower and slower group velocity until the cavity cutoff frequency exceeds the photon frequency, at which point they become evanescent waves and can reflect back to where they came from.

The long-distance propagation of the strongly photon-like polaritons gives us a direct

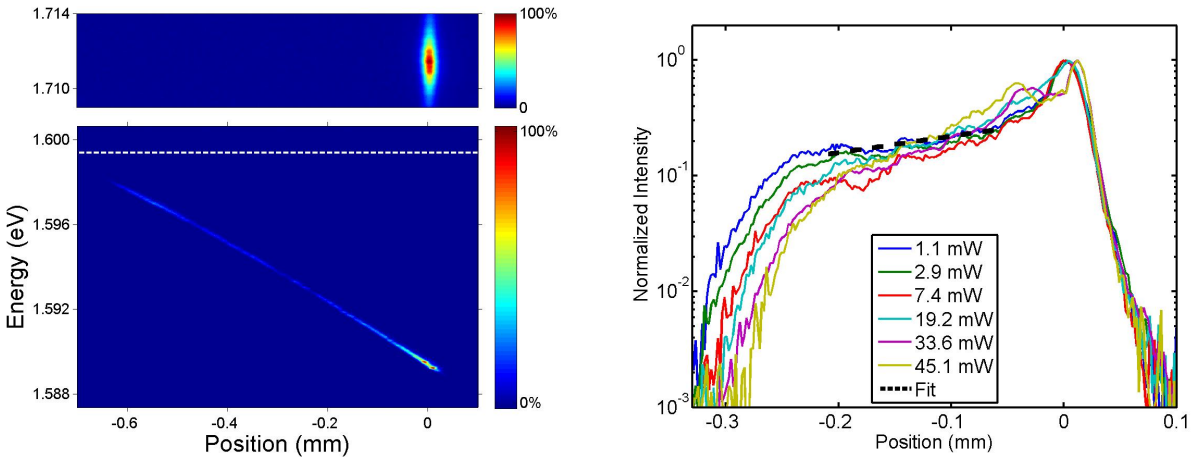

(a) (b)

Figure 5.3: (a) (Upper Image) Photon emission from hot carriers created by the laser excitation spot hitting the microcavity structure, at a spot on the sample with detuning $\delta = -6$ meV (the polaritons are mostly photon-like). This shows the spatial extent of the excitation region where the polaritons are generated. The laser photon energy is well above the polariton energy, at the third minimum in reflectivity above the microcavity stop band. The sample was cooled with helium vapor at 10 K. (Lower Image) PL from the lower polaritons under the same conditions, collected at a nearly orthogonal angle from the sample surface corresponding to nearly zero in-plane momentum of the polaritons. (The energy of the lower polaritons at the resonant point on the sample is indicated by the horizontal dashed line.) In this case the polaritons appear to drift uphill toward the resonant point. (b) The peak photon emission intensity from the polaritons for several different excitation densities, as labeled, for a laser excitation spot at a position on the sample with detuning $\delta = -6$ meV. All of the curves are normalized to the same maximum height. The dashed line corresponds to a single-exponential decay with decay length $l = 300$ μm.

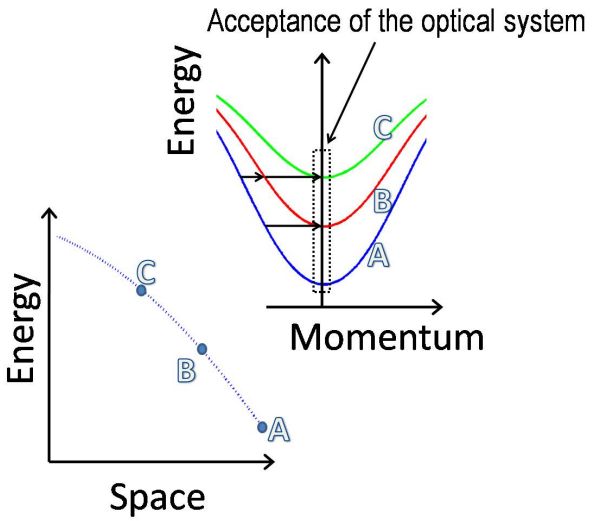

Figure 5.4: Illustration of the process by which the polaritons appear to move uphill. Polaritons in high-k states which escape the excitation region travel ballistically. As the cavity width shrinks, the effective k-vector drops until it reaches $\mathbf{k}_{\|} = 0$.

measure of the cavity lifetime, however. Since the polaritons have an effective mass $m \approx 10^{-4} m_e$, we can use the simple Newtonian formula for motion without scattering, $x = v_0 t + 1/2 a t^2$, where $a = F/m$, and F is the measured force given by the gradient of the potential, which here is 13 meV/mm. The initial velocity v_0 is found from the difference in energy between the point of photon generation by the pump laser and the point where the photon is detected. From the fit to the low-density data of Fig. 5.3b, the exponential decay length is approximately 300 μm. (The region near the laser spot at $x = 0$ is excluded since there is spatial structure due to trapping, discussed below, and the region past $x = 0.2$ mm is excluded because this is the strongly resonant region, in which the polaritons scatter much more efficiently due to their excitonic component.) The Newtonian calculation gives a travel time of 160 ps from the laser spot where the polaritons are generated to a spot 300 microns away. This calculation assumes that the photon-like polaritons travel ballistically; if they do not, then their lifetime must be even longer.

Figure 5.5 shows data for polariton motion when the polaritons have been created in a

region of the sample with positive detuning, far on the exciton-like side of the resonance (the upper image of Fig. 5.5a shows the profile of the excitation region). As seen in Fig. 5.5b, a small fraction of the polaritons leaves the excitation region and drifts over 500 microns down the potential gradient, past the resonant point. In this case, the polaritons can be seen moving to lower energy because the exciton component of the polaritons allows them to emit phonons to lose energy; both the polariton-polariton and polariton-phonon interactions come from the exciton part of the polariton. In previous work [10], some downhill drift of polaritons was also seen. In Ref. [86], downhill drift of up to 50 μm was seen in a cavity thickness gradient. In Ref. [1], drift of up to 40 μm was seen for a force of approximately 50 meV/mm created by a strain-induced shift of the exciton energy. This was enough to cause the polariton distribution created by the laser to shift to have a local maximum at the center of a harmonic potential trap, away from the center of the laser peak. The lifetime for the polaritons [1] with low momentum was approximately 16 ps at a temperature of 30 K, however, implying an average distance traveled with no applied force of 6 μm.

Returning for a moment to Chapter 4, the data of Fig. 4.1a are for relatively low excitation density. The light collected for Fig. 4.1a was integrated over about a 100 μm spatial range, so that light emitted by particles moving away from the laser generation spot was also included in the momentum-space data. As seen in this figure, the entire momentum distribution shows a smearing to the right, with nonzero average momentum. This comes about due to the acceleration of the particles in the spatial potential gradient, discussed above; the particles move with $dp/dt = F$ toward the rightward direction in momentum space. The smearing on the right side of the plot corresponds to particles initially moving downhill and accelerating; the smearing of the left side of the curve corresponds to slowing down of particles initially heading uphill; some of these particles eventually reach $\mathbf{k}_{\|} = 0$, and correspond to the emission seen in the spatially resolved data of Fig. 5.3. The average change of momentum seen in Fig. 4.1a, about 1.5×10^4 cm^{-1}, corresponds to the expected gain of momentum for the measured potential gradient for a scattering time of 75 ps, which implies a mean free path of about 60 μm. This is shorter than the scattering time deduced above from the long-distance "uphill" motion of the polaritons, because the polaritons have a much larger excitonic component in this case, which gives stronger interactions.

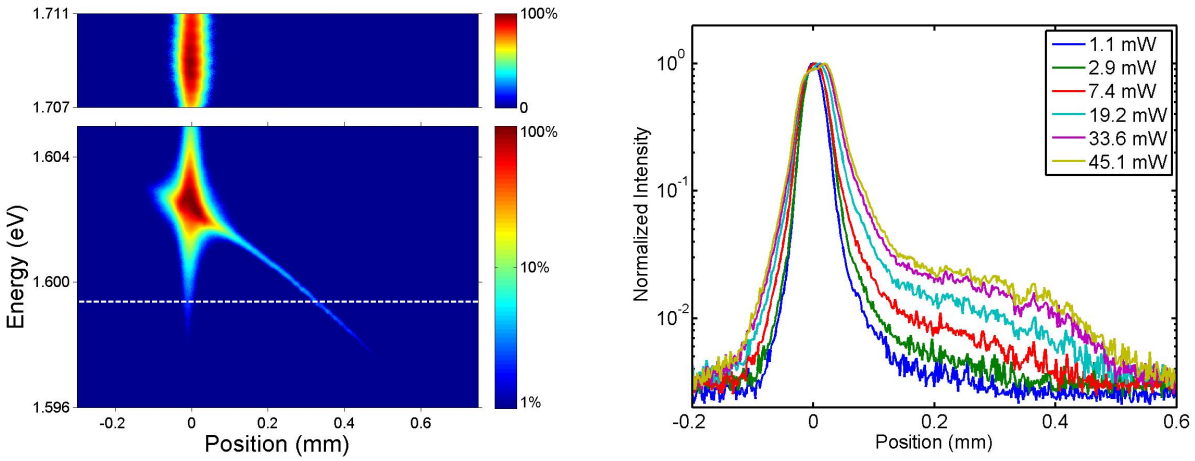

(a) (b)

Figure 5.5: (a) (Upper Image) Photon emission from hot carriers created by the laser excitation spot hitting the microcavity structure, for conditions the same as Fig. 5.3, but at a spot on the sample with detuning $\delta = +8.5$ meV (the polaritons are mostly exciton-like). (Lower Image) Photon emission from the lower polaritons under the same conditions. (The energy of the lower polaritons at the resonant point on the sample is indicated by the horizontal dashed line). The long tail to the right is due to polariton drift in the potential energy gradient. (b) The peak intensity of the photon emission from the polaritons for several different excitation densities, as labeled, for the same detuning as (a), $\delta = +8.5$ meV. All of the curves are normalized to the same maximum height.

We were able to use the lifetime measurement data and drift measurement data to put bounds on the polariton lifetime in these samples. In the lifetime measurements, we found lifetimes of 200-300 ps, which depend on the detuning. These measured lifetimes are overstated because they include an additional, slow process where the polaritons scatter to an extremely long-lifetime exciton reservoir. On the other hand, based on luminescence from polariton transport, we were able to measure a lifetime of 75-100 ps. These lifetime measurements are understated because they neglect scattering processes such as polariton-polariton, polariton-exciton, and polariton-photon scattering. From these experiments we can conclude that the polariton lifetime is 75 ps $< \tau <$ 300 ps depending on the detuning. This is still two orders of magnitude better than recent polariton lifetimes [74] while still maintaining a great enough polariton mobility to see the polaritons move a distance of over 1 mm.

6.0 CONCLUSIONS AND FUTURE DIRECTIONS

6.1 CONCLUSIONS

The motivation for this work was to study the BEC transition for polaritons. A large part of my work was aimed at determining what degree this transition can be distinguished from lasing. In the first set of experiments, this was done by showing that, as predicted, the trap plays an essential role by changing the density of states to something which is more favorable to observe BEC [11]. It was shown that when the trap was applied there were two distinct transition with increasing density; one which we associated with BEC and the other we associated with lasing [10]. When no trap was applied, only a single transition was seen, and this happened at an energy which was slightly red-shifted from the bare-photon state, and not at the polariton energy; this implied that this transition happens in the high-density, weak-coupling regime at densities where polaritons can no longer be considered as stable quasi-particles.

When high stresses were applied to the sample, light-hole heavy-hole mixing coupled with anisotropic exchange gave a fine structure to the upper and lower polaritons [54]. This phenomenon was modeled with a simple, short-range exchange mechanism leaving the exchange constants a_i as variables. The results, which nicely fit the data, were in good accordance to previously determined values of the anisotropic exchange constants for quantum wells which were similar to the ones used in our samples. The shift of the polariton condensate emission with stress further shared that they were in the strong coupling (BEC) regime.

The next experiments showed that when an asymmetric trap was used to confine polaritons, the Bose-condensed portion of the ensemble exhibited the same momentum-state

density one would expect to get from the ground state of the trap. The uncondensed fraction, still behaving classically, distributed itself symmetrically in k-space in accordance with the equipartition theorem. However, there remain some questions about the shift of the ground state emission away from $k = 0$.

In experiments that involved the long-lifetime samples, the intense $k \approx 0$ luminescence peak was coming from a spot on the sample away from where the pump laser was creating the polaritons. This eliminates the possibility of population inversion, which is necessary condition to achieve lasing. In these new samples, there is a dramatic transition from a classical gas to a quantum coherent one [12]. The transition is quite impressive when compared with other experiments in polariton BEC. First, there is a spectral narrowing and an increase in drift length, measured in both real space and momentum space, which are both associated with the increased coherence of a superfluid. At this point, the superfluid polaritons coherently scatter with the exciton reservoir, which in turn behaves as a 1D potential trap. When the gas is driven to even higher density, the energy drops and the spectral- and momentum-space distributions spontaneously transition to a state at $k = 0$ with an energy spectrum so narrow that it can't be measured by our detection system.

When this transition occurs, sometimes the 2D momentum distribution exhibits interesting patterns which can possibly be explained by the formation of vortex-antivortex pairs. The stability of these patterns is quite long since they persist for at least 3 ms, which is much longer than the polariton lifetime. Again, this transition is not lasing because the luminescence comes from a point on the sample slightly away from the excitation spot, such that population inversion does not exist. The mode pattern is consistent with one from a cylindrically symmetric potential, but the confining potential is clearly not cylindrically symmetric. Our initial explanation is that the polariton superfluid forms vortex-antivortex pairs, creating a type of standing wave pattern measurable in momentum space.

6.2 PROSPECTIVE EXPERIMENTS

6.2.1 Vortices

While many interesting phenomena of BEC have been observed, both through the course of this work and work by other groups, there are still a lot of interesting phenomenon that are predicted to exist. The preliminary results of superfluid vortex formation initiated in these studies, discussed in Section 4.2, is perhaps lacking in breadth, exhibiting only momentum-space features that are detectable. Taking these experiments to higher density and larger size, with an optical system that has better spatial resolution, should provide useful in determining the validity of these experiments.

6.2.2 Josephson Oscillations

Josephson oscillations are another interesting feature that has been predicted and shown to exist in some polariton experiments. These experiments are missing some key elements of nicely designed experiments, however, because they lack tunability. In some experiments, two adjacent defect traps were used to observe these oscillations [8]. This case is extremely undesirable because the stochastic nature of defects makes it almost impossible to find another defect system to precisely repeat these experiments. Other as-yet unpublished experiments in Josephson oscillations (J. Bloch, private communication) were performed in specially tailored micropillar systems. Because the process of creating the micropillars destroys the sample in the surrounding area and relies on an air gap to supply the barrier, these experiments are also limited. Only the width of the potential barrier can change, but changing the height of the barrier is impossible. We propose an experiment with a stress trap in the lifetime-enhanced samples, in which an exciton-reservoir potential barrier is created in the middle, splitting the trap into two sides. This would provide a confining potential that looks like Fig. 6.1. Creating a superfluid on either side of this barrier would generate the necessary system to observe Josephson oscillations with the added benefit of having an adjustable barrier between the two sides.

The exciton-reservoir trap is a long-lived potential because the only decay mechanism

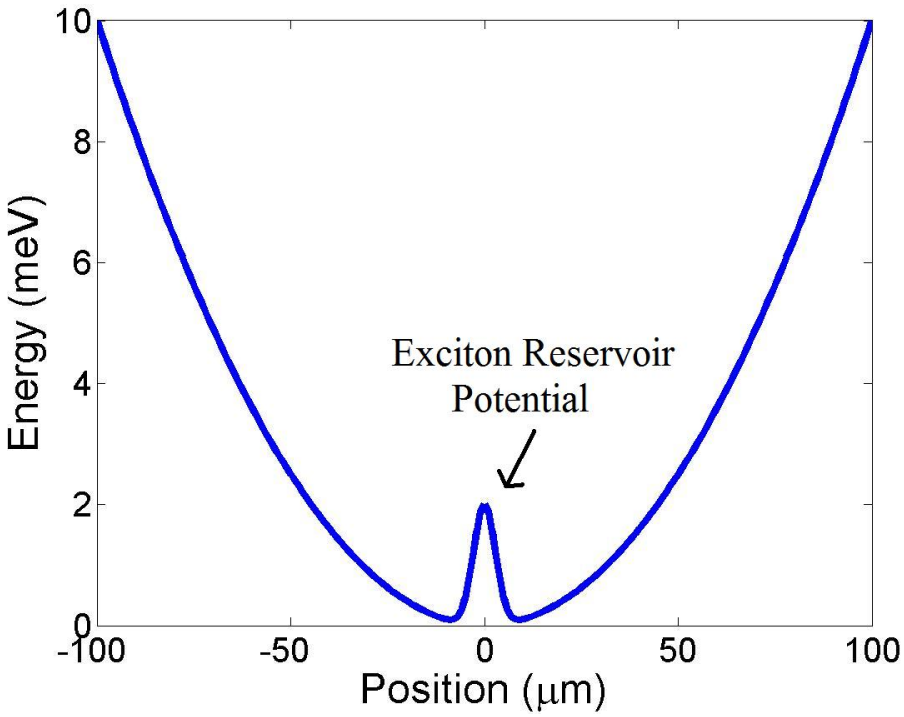

Figure 6.1: Potential for a Josephson oscillation experiment. Creating a superfluid on both sides of the exciton reservoir while varying the width and height of this barrier would provide tunability to the polariton Josephson oscillation experiments that was previously unavailable in polaritons.

that the exciton reservoir has is through the creation of polaritons. It is adjustable in both width, by changing the focus spot size, and height, by changing the pump intensity. Therefore, it is only useful in experiments where modifying the time-independent spatial potential is needed. It has one other interesting feature as it will also act as a source of polaritons.

6.2.3 Stark-Shift Potential

As we have seen, creating potentials to confine polaritons is an important tool for polariton manipulation and for enhancing the effects of BEC. However, up until now these potentials have been relatively static over the life of the polaritons. The stress trap doesn't change on any meaningful experimental time scales and the exciton reservoir trap lasts until the excess carriers decay away, with a reservoir lifetime of over 400 ps. Traps used by other groups, such as defect traps and micropillars, are permanently fixed. In a collaboration with Alex Hayat at the University of Toronto, we are investigating a way of manipulating polaritons using the AC Stark effect [87]. The potential created by means of the AC Stark effect only lasts as long as the incident laser pulse, which in these experiments is only 100 fs. Although these experiments have been performed on excitons before [88, 89], this was the first time the AC Stark shift has ever been observed in a microcavity polariton system. My part in this project was to provide a theoretical and practical basis on the performance of these experiments with the samples and available equipment.

The AC Stark shift comes about in the same way that the anti-crossing of the photon mode of a cavity with the exciton state forms, through the dipole coupling matrix. The AC Stark shift however, relies on an intense laser pulse to generate large, off-diagonal coupling instead of using the confinement of the cavity to create a large electric field. By splitting the electric field into a quantized part (the cavity photon) and classical part (the intense laser), i.e., ($\mathbf{E} = \mathbf{E}_{\text{class}} + \mathbf{E}_{\text{quant}}$), it is straight forward to arrive at the Stark shift Hamiltonian for

polaritons using a variation of Eq. (1.21):

$$H = \begin{pmatrix} E_X & \Omega & \mu\sqrt{I} \\ \Omega & E_C & 0 \\ \mu\sqrt{I} & 0 & E_P \end{pmatrix}, \tag{6.1}$$

where μ is the dipole moment of the exciton, I is the intensity of the laser, E_C and E_P are the cavity energy and laser energy respectively, E_X is the exciton energy and Ω is the Rabi coupling of the cavity photon to the exciton.

The experiments were performed at the University of Toronto by Alex Hayat and used a Ti:Sapph regenerative amplifier, which lacks substantial wavelength tunability, injected into the microcavity through a reflectivity minimum located energetically below the stop band. The amplifier, tuned to around 800 nm, was chosen to be well below the polariton energy, 774 nm, in order to prevent the excitation of a significant population of polaritons from this pulse, known as the pump. This pump was responsible for the Stark shift of the polaritons. The wavelength of the pump could not be tuned significantly so the angle of the laser was varied in order to hit the reflectivity minimum (see Fig. 1.7a) just below the stop band. The probe, a super-continuum white-light pulse generated from a sapphire crystal, was used to make reflectivity measurements of the polariton energy. A delay line was used to create a delay between the pump and the probe so that time-dependent effects could be measured. The differential reflectivity

$$\Delta R = \frac{I_{PPR}(\tau) - I_P}{I_{PR} - I_{BG}} \tag{6.2}$$

was measured. Here, I_{PPR} is the signal with both the pump and probe turned on, τ is the delay time, I_P is just the pump signal, I_{PR} is just the probe, and I_{BG} is the background signal. The calculated and experimental results are shown below in Fig. 6.2. As can be seen, Stark shifts of up to 0.5 meV have been achieved, providing the ability to manipulate polaritons on very reasonable time scales ($\sim$100 ps).

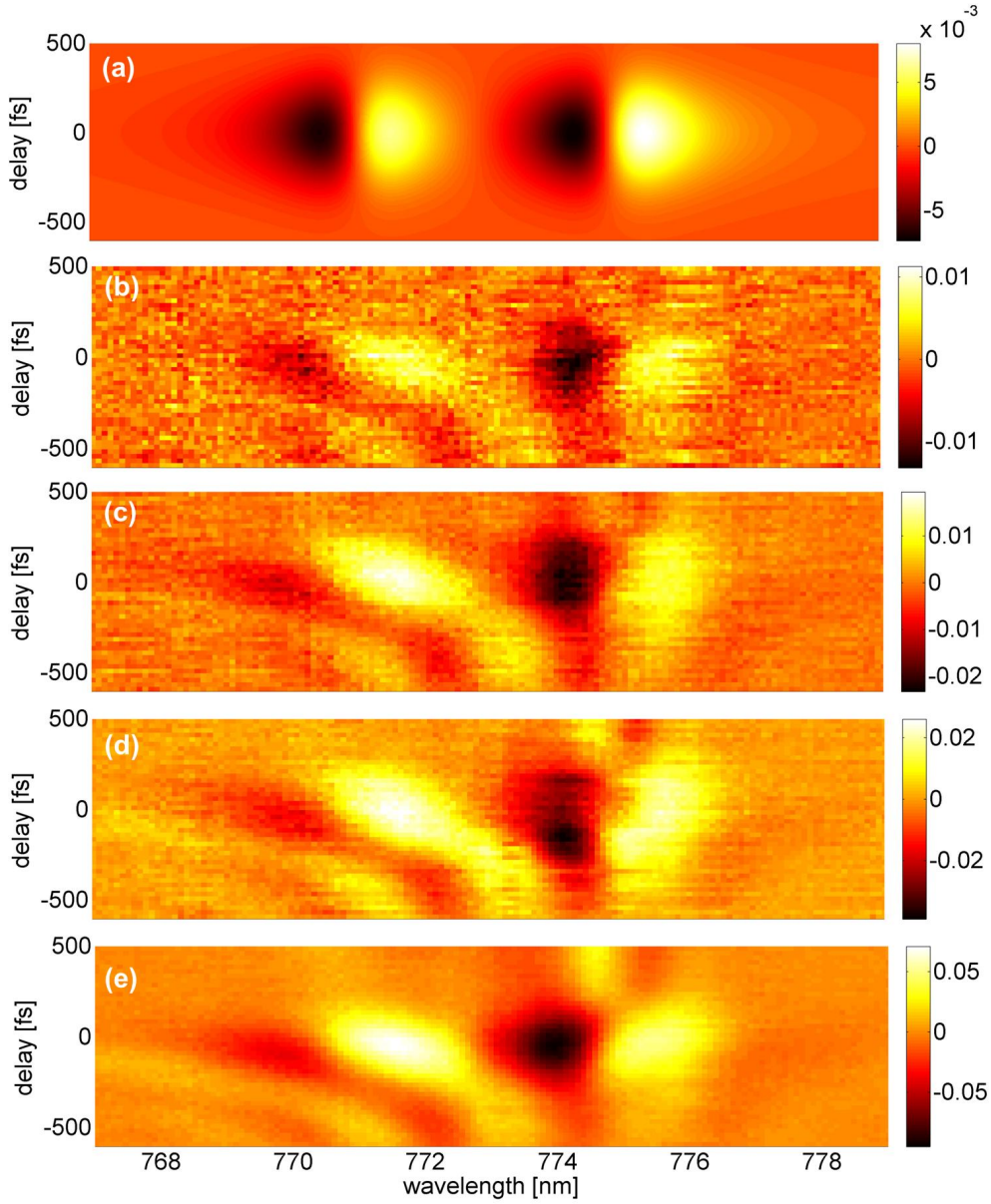

Figure 6.2: (a) Calculated differential spectra for various pump-probe time-delays for a pump fluence of 0.1 nJ/m^2. Measured differential spectra for various pump-probe time-delays for a pump fluence of (b) 0.2 mJ/cm^2 (c) 0.6 mJ/cm^2 (d) 1.2 mJ/cm^2 (e) 2.04 mJ/cm^2. From Alex Hayat et al. (submitted) [87].

6.2.4 Interfering Two Condensates

Another interesting experiment that was conducted with atomic condensates is the condensate interference experiment [90]. In this experiment, a condensate is created at the center of a trap. An external potential is then used to fracture the initial condensate into two spatially separated condensates. The two condensates are then brought back together and matter-wave interference fringes become visible via the interference of the two condensates.

The combination of long-lifetime polaritons, the AC Stark shift, and a stress trap could bring these experiments into fruition for polaritons. By creating a polariton condensate at the bottom of a stress trap, then tearing it apart using a quick AC Stark barrier, the initial condensate would be separated into two parts and be driven up the walls of the stress trap. When the two fractions return to the center of the trap, the Stark-shifted potential would no longer exist allowing the two condensates to merge into one. This process should reproduce the same effects seen in Ketterle's experiments.

APPENDIX A

2ND QUANTIZED POLARITON HAMILTONIAN

A.1 CONDUCTION AND VALENCE BAND HAMILTONIAN

In this appendix, I will show a full calculation of the polariton Hamiltonian, following Hanamura and Haug [55], beginning from the full second-quantized Hamiltonian (Eq. (1.1)),

$$\begin{aligned} H = &\int \mathbf{\Psi}(\mathbf{x})^\dagger \left(-\frac{\hbar^2}{2m}\nabla^2 + U(\mathbf{x}) \right) \mathbf{\Psi}(\mathbf{x}) d\mathbf{x} \\ &+ \frac{1}{2} \int\int \mathbf{\Psi}(\mathbf{x})^\dagger \mathbf{\Psi}(\mathbf{x}')^\dagger \frac{e}{|\mathbf{x}-\mathbf{x}'|} \mathbf{\Psi}(\mathbf{x}) \mathbf{\Psi}(\mathbf{x}') d\mathbf{x} d\mathbf{x}'. \end{aligned} \tag{A.1}$$

Simplifying in terms of the Bloch functions, for which we will consider two classes, the conduction band and the valence band, we have

$$\Psi(\mathbf{x}) = \frac{1}{\sqrt{V}} \sum_{\mathbf{k}} \left[e^{i\mathbf{k}\cdot\mathbf{x}} u_{c,\mathbf{k}}(\mathbf{x}) \mathbf{b}_{c,\mathbf{k}} + e^{i\mathbf{k}\cdot\mathbf{x}} u_{v,\mathbf{k}}(\mathbf{x}) \mathbf{b}_{v,\mathbf{k}} \right], \tag{A.2}$$

with the Bloch functions being eigenfunctions of the single-particle Hamiltonian such that

$$H = \left(-\frac{\hbar^2}{2m}\nabla^2 + U(\mathbf{x}) \right) e^{i\mathbf{k}\cdot\mathbf{x}} u_{i,\mathbf{k}}(\mathbf{x}) = E_i(\mathbf{k}) e^{i\mathbf{k}\cdot\mathbf{x}} u_{i,\mathbf{k}}(\mathbf{x}). \tag{A.3}$$

Inserting the Bloch functions into Eq. (A.1), we find

$$\begin{aligned} H = &\sum_{\mathbf{k}} E_c(\mathbf{k}) \mathbf{b}^\dagger_{\mathbf{k},c} \mathbf{b}_{\mathbf{k},c} + \sum_{\mathbf{k}} E_v(\mathbf{k}) \mathbf{b}^\dagger_{\mathbf{k},v} \mathbf{b}_{\mathbf{k},v} + \frac{1}{2} \sum_{\{\mathbf{k}\}} V^{c,c,c,c}_{\mathbf{k_1},\mathbf{k_2},\mathbf{k_3},\mathbf{k_4}} \mathbf{b}^\dagger_{\mathbf{k_1},c} \mathbf{b}^\dagger_{\mathbf{k_2},c} \mathbf{b}_{\mathbf{k_3},c} \mathbf{b}_{\mathbf{k_4},c} \\ &+ \frac{1}{2} \sum_{\{\mathbf{k}\}} V^{v,v,v,v}_{\mathbf{k_1},\mathbf{k_2},\mathbf{k_3},\mathbf{k_4}} \mathbf{b}^\dagger_{\mathbf{k_1},v} \mathbf{b}^\dagger_{\mathbf{k_2},v} \mathbf{b}_{\mathbf{k_3},v} \mathbf{b}_{\mathbf{k_4},v} + \sum_{\{\mathbf{k}\}} V^{c,v,v,c}_{\mathbf{k_1},\mathbf{k_2},\mathbf{k_3},\mathbf{k_4}} \mathbf{b}^\dagger_{\mathbf{k_1},c} \mathbf{b}^\dagger_{\mathbf{k_2},v} \mathbf{b}_{\mathbf{k_3},v} \mathbf{b}_{\mathbf{k_4},c} \\ &+ \sum_{\{\mathbf{k}\}} V^{c,v,c,v}_{\mathbf{k_1},\mathbf{k_2},\mathbf{k_3},\mathbf{k_4}} \mathbf{b}^\dagger_{\mathbf{k_1},c} \mathbf{b}^\dagger_{\mathbf{k_2},v} \mathbf{b}_{\mathbf{k_3},c} \mathbf{b}_{\mathbf{k_4},v}, \end{aligned} \tag{A.4}$$

with $V^{i,j,l,m}_{\mathbf{k_1},\mathbf{k_2},\mathbf{k_3},\mathbf{k_4}}$ representing the Fourier transform of $V(\mathbf{x}-\mathbf{x}')$:

$$V^{i,j,l,m}_{\mathbf{k_1},\mathbf{k_2},\mathbf{k_3},\mathbf{k_4}} = \frac{1}{V^2}\int d^3x d^3x' e^{i(\mathbf{k_4}-\mathbf{k_1})\cdot\mathbf{x}+i(\mathbf{k_3}-\mathbf{k_2})\cdot\mathbf{x}} \times V(\mathbf{x}-\mathbf{x}')u^*_{\mathbf{k_1},i}(\mathbf{x})u^*_{\mathbf{k_2},j}(\mathbf{x}')u_{\mathbf{k_3},l}(\mathbf{x})u_{\mathbf{k_4},m}(\mathbf{x}'). \tag{A.5}$$

We've also neglected terms which change the number of electrons in a given band, such as $V^{v,c,c,c}$, since the electrons kinetic energy at low temperature is presumed to be much less than the band gap energy. As discussed in Section 1.1.1, adopting the picture of the Fermi sea, replacing $\mathbf{b}_{\mathbf{k},c}$ with $\mathbf{e}_\mathbf{k}$ and $\mathbf{b}_{\mathbf{k},v}$ with $\mathbf{h}_{-\mathbf{k}}$, and working through the commutators we find:

$$\begin{aligned} H = E_0 &+ \sum_\mathbf{k} E_e(\mathbf{k})\mathbf{e}^\dagger_\mathbf{k}\mathbf{e}_\mathbf{k} + \sum_\mathbf{k} E_h(\mathbf{k})\mathbf{h}^\dagger_\mathbf{k}\mathbf{h}_\mathbf{k} + \frac{1}{2}\sum_{\{\mathbf{k}\}} V^{c,c,c,c}_{\mathbf{k_1},\mathbf{k_2},\mathbf{k_3},\mathbf{k_4}}\mathbf{e}^\dagger_{\mathbf{k_1}}\mathbf{e}^\dagger_{\mathbf{k_2}}\mathbf{e}_{\mathbf{k_3}}\mathbf{e}_{\mathbf{k_4}} \\ &+ \frac{1}{2}\sum_{\{\mathbf{k}\}} V^{v,v,v,v}_{-\mathbf{k_1},-\mathbf{k_2},-\mathbf{k_3},-\mathbf{k_4}}\mathbf{h}^\dagger_{\mathbf{k_1}}\mathbf{h}^\dagger_{\mathbf{k_2}}\mathbf{h}_{\mathbf{k_3}}\mathbf{h}_{\mathbf{k_4}} - \sum_{\{\mathbf{k}\}}\left(V^{c,v,v,c}_{\mathbf{k_1},\mathbf{k_2},\mathbf{k_3},\mathbf{k_4}} - V^{c,v,c,v}_{\mathbf{k_1},\mathbf{k_2},\mathbf{k_3},\mathbf{k_4}}\right)\mathbf{e}^\dagger_{\mathbf{k_1}}\mathbf{h}^\dagger_{\mathbf{k_2}}\mathbf{h}_{\mathbf{k_3}}\mathbf{e}_{\mathbf{k_4}}, \end{aligned} \tag{A.6}$$

and the electron and hole energies are redefined in terms of an effective mass equation:

$$\begin{aligned} E_0 &= \sum E^0_v(\mathbf{k}) + \sum_{\mathbf{k},\mathbf{k}'}\left(V^{v,v,v,v}_{\mathbf{k},\mathbf{k}',\mathbf{k}',\mathbf{k}} - V^{v,v,v,v}_{\mathbf{k},\mathbf{k}',\mathbf{k},\mathbf{k}'}\right) \\ E_e(\mathbf{k}) &= E^0_c(\mathbf{k}) + \sum_{\mathbf{k}'}\left(V^{c,v,v,c}_{\mathbf{k},\mathbf{k}',\mathbf{k}',\mathbf{k}} - V^{c,v,c,v}_{\mathbf{k},\mathbf{k}',\mathbf{k},\mathbf{k}'}\right) = E_g + \frac{\hbar^2k^2}{2m_e} \\ E_h(\mathbf{k}) &= -E^0_v(-\mathbf{k}) - \sum_{\mathbf{k}'}\left(V^{v,v,v,v}_{\mathbf{k}',-\mathbf{k},-\mathbf{k},\mathbf{k}'} - V^{v,v,v,v}_{\mathbf{k}',-\mathbf{k},\mathbf{k}',-\mathbf{k}}\right) = \frac{\hbar^2k^2}{2m_h}, \end{aligned} \tag{A.7}$$

These are the renormalized bands taking into account the local density of the valence band electrons. Since we are dealing with low temperature semiconductors Umklapp processes are ignored.

A.2 THE EXCITON CREATION OPERATOR

The general correlated electron-hole state has the general form:

$$\mid X\rangle = \sum_{\mathbf{k}_e,\mathbf{k}_h} A_{\mathbf{k}_e,\mathbf{k}_h} \mathbf{e}^\dagger_{\mathbf{k}_e} \mathbf{h}^\dagger_{\mathbf{k}_h} \mid 0\rangle, \tag{A.8}$$

where $\mid 0\rangle$ is the vacuum, represented by a filled valence band and empty conduction band. Applying this to Eq. (A.6) gives the exciton eigenvalue equation:

$$\left(E_e(\mathbf{k}_e) + E_h(\mathbf{k}_h) - E\right) A_{\mathbf{k}_e,\mathbf{k}_h} - \sum_{\mathbf{l},\mathbf{l}'} \left(V^{c,v,v,c}_{\mathbf{k}_e,-\mathbf{l}',-\mathbf{k}_h,\mathbf{l}} - V^{c,v,c,v}_{\mathbf{k}_e,-\mathbf{l}',\mathbf{l},-\mathbf{k}_h}\right) A_{\mathbf{l},\mathbf{l}'} = 0. \tag{A.9}$$

If we neglect the short-range parts of the Coulomb interaction and only keep the long range parts as in Eq. (3.13) (this neglects short-range exchange which we add back later as a perturbation), then taking the Fourier transform of Eq. (A.9) yields the Schrödinger equation

$$\left(-\frac{\hbar^2}{2m_e}\nabla^2_e - \frac{\hbar^2}{2m_h}\nabla^2_h + E_g - \frac{e^2}{\epsilon_0 \mid \mathbf{x}_e - \mathbf{x}_h \mid}\right) \phi(\mathbf{x}_e,\mathbf{x}_h) = E\phi(\mathbf{x}_e,\mathbf{x}_h), \tag{A.10}$$

with $\phi(\mathbf{x}_e,\mathbf{x}_h)$ representing the Fourier transform of $A_{\mathbf{k}_e,\mathbf{k}_h}$, or

$$\phi(\mathbf{x}_e,\mathbf{x}_h) = \sum_{\mathbf{k}_e,\mathbf{k}_h} A_{\mathbf{k}_e,\mathbf{k}_h} e^{i\mathbf{k}_e\cdot\mathbf{x}e + i\mathbf{k}_h\cdot\mathbf{x}_h}. \tag{A.11}$$

The exciton, like any other $V \propto 1/r$ orbital problem in physics, is best described in a center-of-mass coordinate system where we'll define the new coordinates as:

$$\mathbf{r} = \mathbf{x}_e - \mathbf{x}_h \quad \text{and} \quad \mathbf{X}_{cm} = (m_e\mathbf{x}_e + m_h\mathbf{x}_h)/(m_e + m_h), \tag{A.12}$$

where $\mathbf{x}_e$ and $\mathbf{x}_h$ are the positions of the electron and hole and m_e and m_h are the effective masses of the conduction-band electron and valence-band hole. The conjugate variables to $\mathbf{r}$ and $\mathbf{X}_{cm}$ become

$$\mathbf{k} = i\nabla_{\mathbf{r}} = (m_h\mathbf{k}_e - m_e\mathbf{k}_h)/(m_e + m_h) \quad \text{and} \quad \mathbf{K}_{cm} = \nabla_{\mathbf{X}_{cm}} = \mathbf{k}_e + \mathbf{k}_h, \tag{A.13}$$

such that $\mathbf{k}_e$ and $\mathbf{k}_h$ expressed in this new coordinate system are given by

$$\mathbf{k}_e = \frac{m_e}{m_e + m_h}\mathbf{K}_{cm} + \mathbf{k} \quad \text{and} \quad \mathbf{k}_h = \frac{m_h}{m_e + m_h}\mathbf{K}_{cm} - \mathbf{k}. \tag{A.14}$$

In the new reduced-mass coordinate system, the single particle Schrödinger equation becomes

$$\left(-\frac{\hbar^2}{2(m_h+m_e)}\nabla^2_{\mathbf{X}_{cm}} - \frac{\hbar^2}{2m_r}\nabla^2_{\mathbf{r}} - \frac{e^2}{4\pi\epsilon \mid \mathbf{r} \mid}\right)\phi(\mathbf{X}_{cm},\mathbf{r}) = E\phi(\mathbf{X}_{cm},\mathbf{r}), \tag{A.15}$$

where m_r is the reduced mass $m_r^{-1} = m_h^{-1} + 1/m_e^{-1}$. The solutions to the $\mathbf{X}_{cm}$ part of the Schrödinger equation are simply plane waves; now we can separate the solution into a product of two functions

$$\phi_\nu(\mathbf{X}_{cm},\mathbf{r}) = \frac{e^{i\mathbf{K}_{cm}\cdot\mathbf{X}_{cm}}}{\sqrt{V}}\phi_\nu(\mathbf{r}) = \frac{e^{i\mathbf{K}_{cm}\cdot\mathbf{X}_{cm}}}{\sqrt{V}}\sum_{\mathbf{k}}\phi_\nu(\mathbf{k})\frac{e^{i\mathbf{k}\cdot\mathbf{r}}}{\sqrt{V}}. \tag{A.16}$$

$\phi_\nu(\mathbf{r})$ are the solutions to the radial Schrödinger equation with index ν. We can then form the exciton creation operator

$$\mathbf{X}^\dagger_\nu(\mathbf{K}_{CM}) = \sum_{\mathbf{k}}\phi_\nu(\mathbf{k})\mathbf{e}^\dagger_{\mathbf{K}_{CM}/2+\mathbf{k}}\mathbf{h}^\dagger_{\mathbf{K}_{CM}/2-\mathbf{k}}. \tag{A.17}$$

If instead one needs the 2D quantum well wave functions, the expansion of the solutions can be considered as a cylindrical problem, i.e.

$$\phi_{nm}(\mathbf{X}_{cm},\mathbf{r}) = \frac{e^{i\mathbf{K}_{cm}\cdot\mathbf{X}_{cm}}}{\sqrt{V}}F(\rho,z_e,z_h) = \frac{e^{i\mathbf{K}_{cm}\cdot\mathbf{X}_{cm}}}{\sqrt{V}}\sum_m\sum_n\phi_{nm}(\rho)f_n(z_e)f_m(z_h), \tag{A.18}$$

with $f_i(z)$ being the ith solution to the confined direction of the finite square well problem for both the conduction-band electron and the valence-band hole. This is the starting point of the exciton wave function and all other terms, such as the exchange interactions, are treated as perturbations.

A.3 EXCITON-PHOTON COUPLING

The exciton coupling to the photon-field is given by Eq. (1.7) [16]:

$$H_{phot-int} = \int \Psi^{\dagger}(\mathbf{x}) \left(-\frac{e}{m_e} \mathbf{A} \cdot \mathbf{p} \right) \Psi(\mathbf{x}) d\mathbf{x}. \tag{A.19}$$

Before we begin simplifying this equation, it is worth noting that intraband transitions, at least in bulk material, are only allowed when the transition conserves both energy and momentum. Figure A1 illustrates the absorption of a photon. Since the dispersion relation of a photon ($E = \hbar c/nk$) is so steep, it is approximately vertical on the relevant energy scales of the exciton. In quantum wells, the confinement gives rise to additional electron-

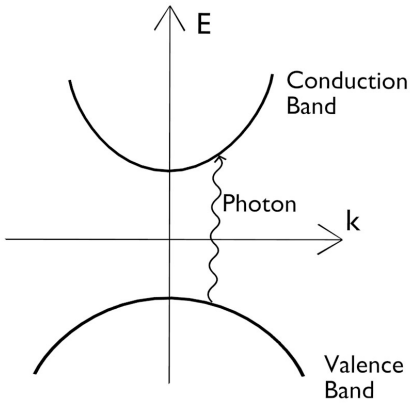

Figure A1: The only processes which conserve both momentum and energy with the photon interaction in bulk GaAs are interband transitions

hole states where photon transitions are possible, but these transitions are on energy scales of ∼100 meV, which are much lower than our polariton energy of 1.6 eV. Also, the exciton itself has possible transitions between orbitals, similar to the hydrogen atom, which allow for the possibility for photon absorption and emission but these are ∼10 meV, even further in energy from the polariton. We can then safely ignore intraband transitions and only

include transitions between the valence and conduction bands near the Γ point. With these simplifications, the photon interaction then becomes

$$\begin{aligned} H_{int} = &-\frac{e}{m_e}\mathbf{A}_0 \cdot \int d^3\mathbf{x} \\ &\times \Bigg[\sum_{\mathbf{k}} e^{-i\mathbf{k}\cdot\mathbf{x}} u^*_{c,\mathbf{k}}(\mathbf{x}) \mathbf{b}^\dagger_{c,\mathbf{k}} \sum_q \left(\mathbf{a}_\mathbf{q} e^{i\mathbf{q}\cdot\mathbf{x}} + \mathbf{a}^\dagger_\mathbf{q} e^{-i\mathbf{q}\cdot\mathbf{x}} \right) \mathbf{p} \sum_{\mathbf{k}'} e^{i\mathbf{k}'\cdot\mathbf{x}} u_{v,\mathbf{k}'}(\mathbf{x}) \mathbf{b}_{v,\mathbf{k}'} \\ &+ \sum_{\mathbf{k}} e^{-i\mathbf{k}\cdot\mathbf{x}} u^*_{v,\mathbf{k}}(\mathbf{x}) \mathbf{b}^\dagger_{v,\mathbf{k}} \sum_q \left(\mathbf{a}_\mathbf{q} e^{i\mathbf{q}\cdot\mathbf{x}} + \mathbf{a}^\dagger_\mathbf{q} e^{-i\mathbf{q}\cdot\mathbf{x}} \right) \mathbf{p} \sum_{\mathbf{k}'} e^{i\mathbf{k}'\cdot\mathbf{x}} u_{c,\mathbf{k}'}(\mathbf{x}) \mathbf{b}_{c,\mathbf{k}'} \Bigg], \end{aligned} \tag{A.20}$$

where we've used

$$\mathbf{A}(\mathbf{x}) = \mathbf{A}_0 \sum_{\mathbf{q}} (\mathbf{a}_\mathbf{q} e^{i\mathbf{q}\cdot\mathbf{x}} + \mathbf{a}^\dagger_\mathbf{q} e^{-i\mathbf{q}\cdot\mathbf{q}}) \tag{A.21}$$

for the vector potential. Under the assumptions of the rotating-wave approximation, we can also throw away terms which transition an electron from the valence band to the conduction band through the creation of a photon and terms which transition a electron from the conduction band to the valence band through the destruction of a photon, i.e., the terms that look like $\mathbf{b}^\dagger_c \mathbf{a}^\dagger_\mathbf{q} \mathbf{b}_v$ and $\mathbf{b}_c \mathbf{a}_\mathbf{q} \mathbf{b}^\dagger_v$. Also noting that $\mathbf{p}(e^{i\mathbf{k}\cdot\mathbf{x}} f(\mathbf{x})) = i\mathbf{k} e^{i\mathbf{k}\cdot\mathbf{x}} f(\mathbf{x}) + e^{i\mathbf{k}\cdot\mathbf{x}} \mathbf{p} f(\mathbf{x})$ we find

$$\begin{aligned} H_{int} = &-\frac{e}{m_e}\mathbf{A}_0 \cdot \int d^3\mathbf{x} \\ &\times \sum_{\mathbf{k},\mathbf{k}',\mathbf{q}} \Big[e^{-i(\mathbf{k}-\mathbf{q}-\mathbf{k}')\cdot\mathbf{x}} u^*_{c,\mathbf{k}}(\mathbf{x}) (i\mathbf{k}' u_{v,\mathbf{k}'}(\mathbf{x}) + \mathbf{p} u_{v,\mathbf{k}'}(\mathbf{x})) \mathbf{b}^\dagger_{c,\mathbf{k}} \mathbf{a}_\mathbf{q} \mathbf{b}_{v,\mathbf{k}'} \\ &+ e^{-i(\mathbf{k}+\mathbf{q}-\mathbf{k}')\cdot\mathbf{x}} u^*_{v,\mathbf{k}}(\mathbf{x}) (i\mathbf{k}' u_{c,\mathbf{k}'}(\mathbf{x}) + \mathbf{p} u_{c,\mathbf{k}'}(\mathbf{x})) \mathbf{b}^\dagger_{v,\mathbf{k}} \mathbf{a}^\dagger_\mathbf{q} \mathbf{b}_{c,\mathbf{k}'} \Big]. \end{aligned} \tag{A.22}$$

In the same way that we did earlier in Chapter 3.2.1, assuming that the oscillations ($e^{-i(\mathbf{k}-\mathbf{q}-\mathbf{k}')}$) are slowly varying over a single unit cell, we can separate the integral into a sum over unit cells times the integral over a single unit cell to obtain

$$\begin{aligned} H_{int} = &-\frac{e}{m_e}\mathbf{A}_0 \cdot \\ &\times \sum_{\mathbf{k},\mathbf{k}',\mathbf{q}} \Bigg[\underbrace{\sum_{\mathbf{X}} e^{-i(\mathbf{k}-\mathbf{q}-\mathbf{k}')\cdot\mathbf{X}}}_{\delta_{\mathbf{k},\mathbf{k}'+\mathbf{q}}} \left(i\mathbf{k}' \int d^3\mathbf{y} u^*_{c,\mathbf{k}}(\mathbf{y}) u_{v,\mathbf{k}'}(\mathbf{y}) + \int d^3\mathbf{y} u^*_{c,\mathbf{k}}(\mathbf{y}) \mathbf{p} u_{v,\mathbf{k}'}(\mathbf{y}) \right) \mathbf{b}^\dagger_{c,\mathbf{k}} \mathbf{a}_\mathbf{q} \mathbf{b}_{v,\mathbf{k}'} \\ &+ \underbrace{\sum_{\mathbf{X}} e^{-i(\mathbf{k}+\mathbf{q}-\mathbf{k}')\cdot\mathbf{X}}}_{\delta_{\mathbf{k},\mathbf{k}'-\mathbf{q}}} \left(i\mathbf{k}' \int d^3\mathbf{y} u^*_{v,\mathbf{k}}(\mathbf{y}) u_{c,\mathbf{k}'}(\mathbf{y}) + \int d^3\mathbf{y} u^*_{v,\mathbf{k}}(\mathbf{y}) \mathbf{p} u_{c,\mathbf{k}'}(\mathbf{y}) \right) \mathbf{b}^\dagger_{v,\mathbf{k}} \mathbf{a}_\mathbf{q} \mathbf{b}_{c,\mathbf{k}'} \Bigg]. \end{aligned} \tag{A.23}$$

The integrals terms without $\mathbf{p}$ are zero due to orthogonality of the Bloch functions, and we make the definition $\mathbf{p}_{cv} = \int d^{\mathbf{x}} u_{c,\mathbf{k}}(\mathbf{x}) \mathbf{p} u_{v,\mathbf{k}}(\mathbf{x})$ which is a measured material parameter for GaAs. Also the sums out front give momentum-conserving delta functions. The above equation becomes

$$H_{int} = -\frac{e}{m_e} \mathbf{A}_0 \cdot \sum_{\mathbf{k},\mathbf{q}} \left(\mathbf{p}_{c,v} \mathbf{b}^{\dagger}_{c,\mathbf{k}+\mathbf{q}} \mathbf{b}_{v,\mathbf{k}} \mathbf{a}_{\mathbf{q}} + \mathbf{p}_{v,c} \mathbf{b}^{\dagger}_{v,\mathbf{k}} \mathbf{b}_{c,\mathbf{k}+\mathbf{q}} {\mathbf{a}_{\mathbf{q}}}^{\dagger} \right). \tag{A.24}$$

Rearranging this in terms of the exciton field operator (Eq. (A.17)and adding this to Eq. (A.6), we find the form of the polariton Hamiltonian

$$H = \sum_{\mathbf{k}} E_P(\mathbf{k}) \mathbf{a}^{\dagger}_{\mathbf{k}} \mathbf{a}_{\mathbf{k}} + \sum_{\mathbf{k}} E_X(\mathbf{k}) \mathbf{X}^{\dagger}_{\mathbf{k}} \mathbf{X}_{\mathbf{k}} + \sum_{\mathbf{k}} \Omega(\mathbf{k}) (\mathbf{a}_{\mathbf{k}} \mathbf{X}^{\dagger}_{\mathbf{k}} + \mathbf{X}_{\mathbf{k}} \mathbf{a}^{\dagger}_{\mathbf{k}}), \tag{A.25}$$

where

$$\Omega = \mid \phi_{1s}(\mathbf{r} = 0) \mid \boldsymbol{\epsilon} \cdot \mathbf{p}_{c,v} \left(-\frac{e}{m_e} \sqrt{\frac{\hbar}{2\epsilon_0 \omega_{\mathbf{q}} V}} \right), \tag{A.26}$$

and we have used $\mathbf{A}_0 = \left(\sqrt{\frac{\hbar}{2\epsilon_0 \omega_{\mathbf{q}} V}} \right) \boldsymbol{\epsilon}$ and $\boldsymbol{\epsilon}$ is the polarization vector.

APPENDIX B

STRESS-STRAIN MODEL

To determine all of the physical effects the stressing apparatus (Fig. 3.1a) has on our polaritons, it is first necessary to determine how the boundary conditions (Fig. 3.2) produce strain inside the sample [16], particularly inside the quantum wells. To do so, we used a finite difference computer simulation to integrate the following equation, starting from an unstrained lattice:

$$\rho \ddot{u}_i = f_i + \sum_j \frac{\partial \sigma_{ij}}{\partial x_j}, \tag{B.1}$$

where σ_{ij} is the stress tensor. This equation is just Newton's second law when the total forces on an infinitesimal volume are summed. The u_i's are the displacement of the volume relative to their unstrained position, and the σ_{ij}'s only act on the surface of the infinitesimal volume. The assignment of the stress tensor indices is shown in Fig. B1.

If the strains are small, then the material stresses are linearly related to the strains through a generalization of Hooke's Law using the stiffness tensor [23],

$$\begin{pmatrix} \sigma_1 \\ \sigma_2 \\ \sigma_3 \\ \sigma_4 \\ \sigma_5 \\ \sigma_6 \end{pmatrix} = \begin{pmatrix} C_{11} & C_{12} & C_{12} & 0 & 0 & 0 \\ C_{12} & C_{11} & C_{12} & 0 & 0 & 0 \\ C_{12} & C_{12} & C_{11} & 0 & 0 & 0 \\ 0 & 0 & 0 & C_{44} & 0 & 0 \\ 0 & 0 & 0 & 0 & C_{44} & 0 \\ 0 & 0 & 0 & 0 & 0 & C_{44} \end{pmatrix} \begin{pmatrix} \epsilon_1 \\ \epsilon_2 \\ \epsilon_3 \\ \epsilon_4 \\ \epsilon_5 \\ \epsilon_6 \end{pmatrix}, \tag{B.2}$$

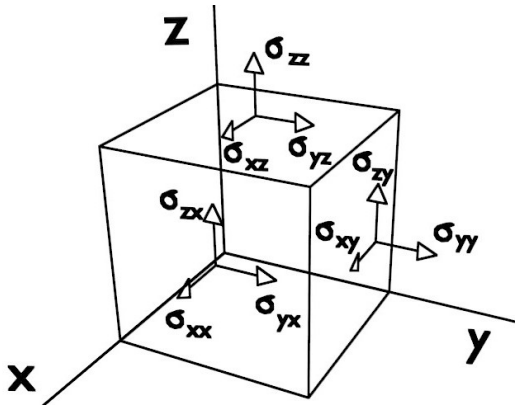

Figure B1: Graphical representation of the way stress in a crystal acts on an infinitesimal volume.

with the standard simplifications

$$\begin{aligned}
&\sigma_1 = \sigma_{xx}; \quad \epsilon_1 = \epsilon_{xx}; \quad \sigma_4 = \sigma_{yz}; \quad \epsilon_4 = 2\epsilon_{yz}; \\
&\sigma_2 = \sigma_{yy}; \quad \epsilon_2 = \epsilon_{yy}; \quad \sigma_5 = \sigma_{xz}; \quad \epsilon_5 = 2\epsilon_{xz}; \\
&\sigma_3 = \sigma_{zz}; \quad \epsilon_3 = \epsilon_{zz}; \quad \sigma_6 = \sigma_{xy}; \quad \epsilon_6 = 2\epsilon_{xy},
\end{aligned} \tag{B.3}$$

This tensor is applicable to materials with the same crystal symmetry as GaAs. For GaAs, $C_{11} = 11.879$ N/cm^2, $C_{12} = 5.376$ N/cm^2 and $C_{44} = 5.94$ N/cm^2 [23]. As noted earlier, AlAs has approximately the same values of the stiffness tensor with $C_{11} = 12.5$ N/cm^2, $C_{12} = 5.34$ N/cm^2 and $C_{44} = 5.42$ N/cm^2 [23]; therefore, we can approximately treat our samples as uniform GaAs for the purposes of this calculation.

The strain is related to the displacements u_i through the equation

$$\epsilon_{ij} = \frac{1}{2}\left(\frac{\partial u_i}{\partial x_j} + \frac{\partial u_j}{\partial x_i}\right), \tag{B.4}$$

and when this equation and Eq. (B.2) are applied to Eq. (B.1), it yields the differential equation for the motion of the body of the material,

$$\begin{aligned}
\rho\ddot{u}_x &= \left(C_{11}\tfrac{\partial^2}{\partial x^2} + C_{44}\left(\tfrac{\partial^2}{\partial y^2} + \tfrac{\partial^2}{\partial z^2}\right)\right)u_x + \left(C\tfrac{\partial^2}{\partial x \partial y}\right)u_y + \left(C\tfrac{\partial^2}{\partial x \partial z}\right)u_z \\
\rho\ddot{u}_y &= \left(C\tfrac{\partial^2}{\partial x \partial y}\right)u_x + \left(C_{11}\tfrac{\partial^2}{\partial y^2} + C_{44}\left(\tfrac{\partial^2}{\partial x^2} + \tfrac{\partial^2}{\partial z^2}\right)\right)u_y + \left(C\tfrac{\partial^2}{\partial y \partial z}\right)u_z \\
\rho\ddot{u}_z &= \left(C\tfrac{\partial^2}{\partial x \partial z}\right)u_x + \left(C\tfrac{\partial^2}{\partial y \partial z}\right)u_y + \left(C_{11}\tfrac{\partial^2}{\partial y^2} + C_{44}\left(\tfrac{\partial^2}{\partial x^2} + \tfrac{\partial^2}{\partial z^2}\right)\right)u_z,
\end{aligned} \tag{B.5}$$

with $C \equiv C_{12} + C_{44}$. At the surface of the sample directly in contact with the clamping plates (the blue colored area in Fig. 3.2), the boundary conditions are $u_x = u_y = u_z = 0$. On the unconstrained surfaces (shown as red in Fig. 3.2) the z-components of the stress must go to zero:

$$\begin{aligned} \sigma_{zz} = 0 = C_{12}(\epsilon_{xx} + \epsilon_{yy}) + C_{11}\epsilon_{zz} \\ \sigma_{xz} = 0 = C_{44}\epsilon_{xz} \\ \sigma_{yz} = 0 = C_{44}\epsilon_{yz}. \end{aligned} \tag{B.6}$$

These free boundary conditions are illustrated in Fig. B2

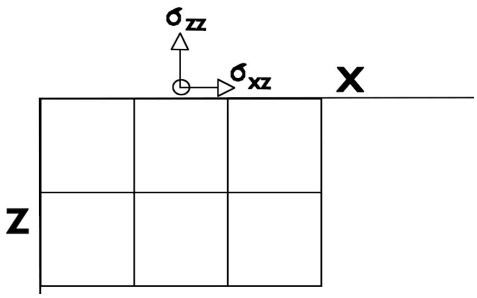

Figure B2: The stresses on the z-face must go to zero at the unconstrained z-boundary of the crystal.

We are looking for a steady-state solution and in order to obtain it, we treat the problem as one of a viscously damped object with the damping force opposite to the stress forces, or

$$F_{\text{damp}} \propto -F_i(u_i) = -c\frac{\Delta u_i}{\Delta t}. \tag{B.7}$$

This equation is iterated in time until the displacements, u_i, reach equilibrium. The results of such a simulation are shown in Fig. B3. They are represented in a form which is easily inserted into the Pikus-Bir Hamiltonian. There are commercially available programs that were also used to solve for strain, such as ANSYS.

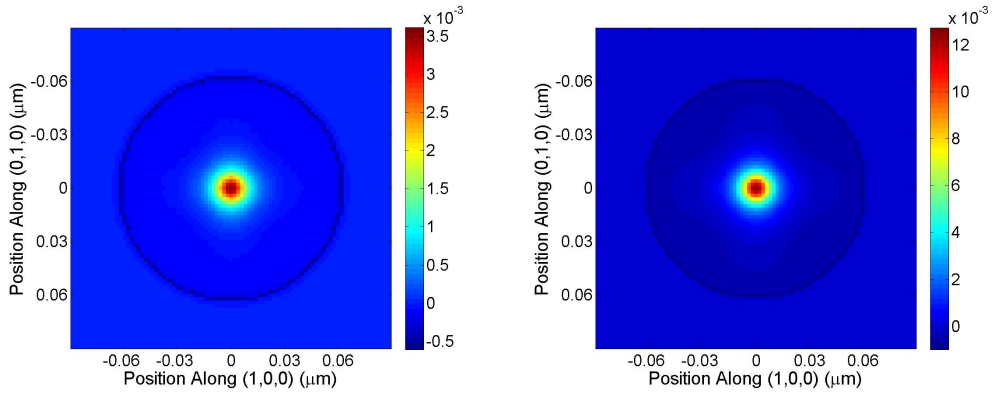

(a) $\epsilon_{xx} + \epsilon_{yy} + \epsilon_{zz}$

(b) $\epsilon_{xx} + \epsilon_{yy} - 2\epsilon_{zz}$

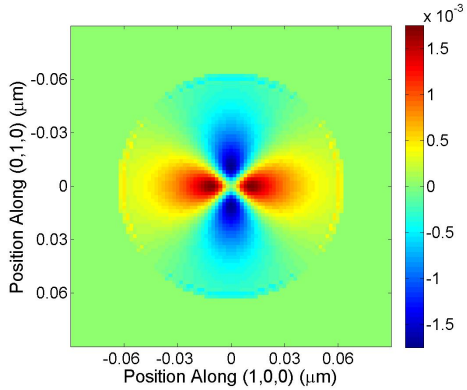

(c) $\epsilon_{xx} - \epsilon_{yy}$

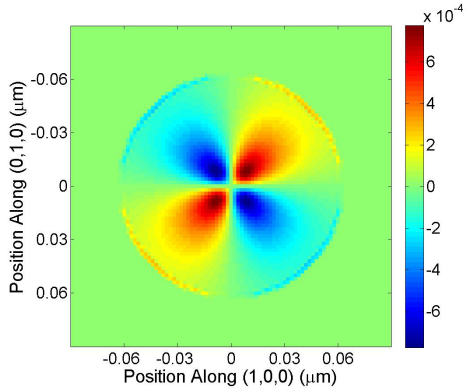

(d) ϵ_{xy}

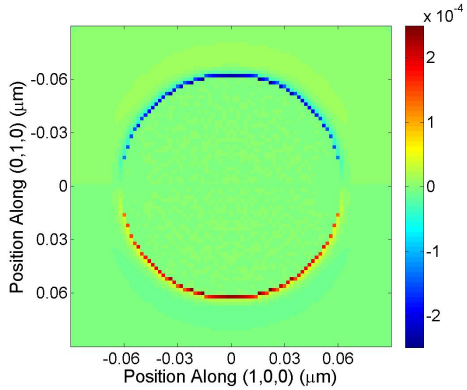

(e) ϵ_{xz}

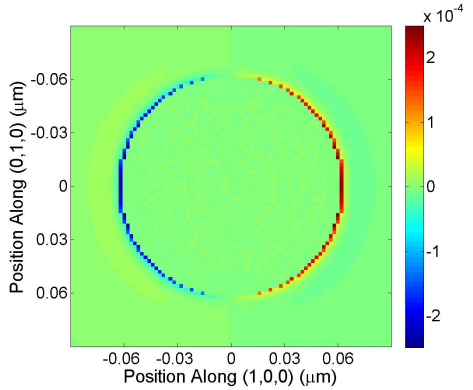

(f) ϵ_{yz}

Figure B3: Results of a strain calculation applying a point force of .66 N to the pin under the boundary conditions given by Fig. 3.2. These are the calculated values of the strains inside the quantum wells that are used in the Pikus-Bir Hamiltonian.

APPENDIX C

THE LUTTINGER-KOHN AND PIKUS-BIR HAMILTONIANS

C.1 K.P THEORY

At this point, the second-quantized notation will be dropped to simplify the calculations of the Luttinger-Kohn and Pikus-Bir Hamiltonians. $\mathbf{k}\cdot\mathbf{p}$ theory is a well known perturbative approach and can be found in many textbooks [16, 23, 91]. If we expand the full Hamiltonian in terms of the Bloch functions about $\mathbf{k}=0$ we find

$$\left(\frac{p^2}{2m_e}+U(\mathbf{x})+\frac{\hbar^2k^2}{2m_e}+\frac{\hbar}{m_e}\mathbf{k}\cdot\mathbf{p}\right)u_{n\mathbf{k}}(\mathbf{x})=E_n(\mathbf{k})u_{n\mathbf{k}}(\mathbf{x}). \tag{C.1}$$

This expansion is most useful about $\mathbf{k}=0$ because, as in Eq. (1.2), the Bloch functions at $\mathbf{k}=0$ have the full symmetry of the crystal. This form of the Hamiltonian is known as the $\mathbf{k}\cdot\mathbf{p}$ Hamiltonian [16]. The general idea of this calculation is to treat the $\mathbf{k}\cdot\mathbf{p}$ term as a perturbation and exploit the symmetry of the bands of interest. Rearranging Eq. (C.1), we have

$$\left(\underbrace{\frac{p^2}{2m_e}+U(\mathbf{x})}_{H_0}+\underbrace{\frac{\hbar}{m_e}\mathbf{k}\cdot\mathbf{p}}_{H'}\right)u_{n\mathbf{k}}(\mathbf{x})=\left(E_n(\mathbf{k})-\frac{\hbar^2k^2}{2m_e}\right)u_{n\mathbf{k}}(\mathbf{x}), \tag{C.2}$$

with $H_0u_{n0}(\mathbf{x})=E_n(0)u_{n0}(\mathbf{x})$. Expanding in the non-degenerate method of perturbation theory yields the first-order energy

$$E_n(\mathbf{k})=E_n(0)+\frac{\hbar^2k^2}{2m_e}+\frac{\hbar}{m_e}\mathbf{k}\cdot\mathbf{p}_{nn'}, \tag{C.3}$$

where $\mathbf{p}_{nn'}\equiv\int d^3\mathbf{x}u^*_{n0}(\mathbf{x})\mathbf{p}u_{n'0}(\mathbf{x})$ and is only non-zero when $n'\neq n$ as discussed earlier.

Even though GaAs lacks inversion symmetry, as do the $\mid u_{n0} >$'s, and the $\mathbf{p}$ operator has odd parity, the first-order expansion of $E_n(\mathbf{k})$ turns out to have a negligible contribution toward the energy [23]. The first-order expansion of the Bloch functions is

$$u_{n\mathbf{k}}(\mathbf{x}) = u_{n0}(\mathbf{x}) + \sum_{n' \neq n} \frac{\hbar}{m_e} \frac{\mathbf{k} \cdot \mathbf{p}_{nn'}}{E_n(0) - E_{n'}(0)} u_{n'0}(\mathbf{x}). \tag{C.4}$$

Since the first-order correction to the energy is zero, we must consider the second-order term. The second-order expansion of the energy is

$$E_n(\mathbf{k}) = E_n(0) + \sum_{\alpha\beta} \left(\frac{\hbar^2}{2m_e} \delta_{\alpha\beta} + \frac{\hbar^2}{2m_e} \sum_{n' \neq n} \frac{p^\alpha_{nn'} p^\beta_{n'n} + p^\beta_{nn'} p^\alpha_{n'n}}{E_n(0) - E_{n'}(0)} \right) k_\alpha k_\beta. \tag{C.5}$$

Equations (C.4) and (C.5) are applicable to the conduction band since it is non degenerate, but for degenerate and potentially coupled bands like the valence band, we must use a degenerate perturbation theory. Expanding Eq. (C.2) in the basis $u_{n\mathbf{k}}(\mathbf{x}) = \sum_{n'} a_{n,n'}(\mathbf{k}) u_{n'0}(\mathbf{x})$ we find the set of coupled equations to be solved are

$$\sum_{n'} \left\{ \left(E_n(0) + \frac{\hbar^2 k^2}{2m_e} \right) \delta_{nn'} + \frac{\hbar}{m_e} \mathbf{k} \cdot \mathbf{p}_{nn'} \right\} a_{n'} = E_n(\mathbf{k}) a_n, \tag{C.6}$$

which amounts to an eigenvalue problem.

C.2 THE LUTTINGER-KOHN HAMILTONIAN

In the derivation of the Luttinger-Kohn Hamiltonian, spin-orbit interaction is an important aspect to take into account because it lifts the degeneracy of the valence band and potentially couples the individual bands. With the spin-orbit interaction included, the Hamiltonian becomes [23]

$$H = \frac{p^2}{2m_e} + U(\mathbf{x}) + \frac{\hbar}{4m_e^2 c^2} [\nabla U \times \mathbf{p}] \cdot \boldsymbol{\sigma}, \tag{C.7}$$

where $\boldsymbol{\sigma}$ is the vector form of the Pauli spin matrices. Now the new form of the $\mathbf{k}\cdot\mathbf{p}$ Hamiltonian (Eq. (C.1)) becomes

$$\left(\frac{p^2}{2m_e}+U(\mathbf{x})+\frac{\hbar^2k^2}{2m_e}+\frac{\hbar}{m_e}\mathbf{k}\cdot(\mathbf{p}+\frac{\hbar}{4m_ec^2}\boldsymbol{\sigma}\times\nabla U)+\frac{\hbar}{4m_e^2c^2}[\nabla U\times\mathbf{p}]\cdot\boldsymbol{\sigma} + \underbrace{\frac{\hbar^2}{4m_e^2c^2}[\nabla U\times\mathbf{k}]\cdot\boldsymbol{\sigma}}_{\approx 0}\right)u_{n\mathbf{k}}(\mathbf{x})=E_n(\mathbf{k})u_{n\mathbf{k}}(\mathbf{x}). \tag{C.8}$$

We have dropped the second, k-dependent term because the crystal momentum is much smaller than the orbital momentum $\mathbf{p}$.

The effects of other bands beyond the conduction and valence band are relevant and must be taken into account. For example, if these other bands are not considered, such as in Kane's model [23], the heavy-hole mass is negative and equivalent to the free-electron mass. Instead of the standard perturbation theory described above, we consider Löwdin perturbation theory [92] where the bands are divided into two classes, A and B, so that:

$$u_{n\mathbf{k}}(\mathbf{x})=\sum_{j'}^{A}a_{n,j'}u_{j'0}(\mathbf{x})+\sum_{\gamma}^{B}a_{n,\gamma}u_{\gamma 0}(\mathbf{x}), \tag{C.9}$$

where A is the valence band set and B is the set of all other bands. At this point, I will skip the details of Löwdin perturbation theory and just present the results. First, note the definitions:

$$\begin{aligned}
-\frac{\hbar^2}{2m_e}\gamma_1&=\frac{1}{3}\left(\left\{\frac{\hbar^2}{2m_e}+\frac{\hbar^2}{m_e^2}\sum_{\gamma}^{B}\frac{p_{x\gamma}^xp_{\gamma x}^x}{E_n(0)-E_\gamma}\right\}+2\left\{\frac{\hbar^2}{2m_e}+\frac{\hbar^2}{m_e^2}\sum_{\gamma}^{B}\frac{p_{x\gamma}^yp_{\gamma x}^y}{E_n(0)-E_\gamma}\right\}\right)\\
-\frac{\hbar^2}{2m_e}\gamma_2&=\frac{1}{6}\left(\left\{\frac{\hbar^2}{2m_e}+\frac{\hbar^2}{m_e^2}\sum_{\gamma}^{B}\frac{p_{x\gamma}^xp_{\gamma x}^x}{E_n(0)-E_\gamma}\right\}-\left\{\frac{\hbar^2}{2m_e}+\frac{\hbar^2}{m_e^2}\sum_{\gamma}^{B}\frac{p_{x\gamma}^yp_{\gamma x}^y}{E_n(0)-E_\gamma}\right\}\right)\\
-\frac{\hbar^2}{2m_e}\gamma_3&=\frac{\hbar^2}{m_e^2}\sum_{\gamma}^{B}\frac{p_{x\gamma}^xp_{\gamma x}^x+p_{x\gamma}^yp_{\gamma y}^x}{E_n(0)-E_\gamma}.
\end{aligned} \tag{C.10}$$

where γ_1, γ_2 and γ_3 are the Luttinger parameters and are measured material parameters. Expanded in the basis $u_{n0}(\mathbf{x})$, found in Eq. (1.3), the Luttinger-Kohn Hamiltonian becomes

$$H_{LK} = -\begin{pmatrix} P+Q & -S & R & 0 & -S/\sqrt{2} & \sqrt{2}R \\ -S^\dagger & P-Q & 0 & R & -\sqrt{2}Q & \sqrt{3/2}S \\ R^\dagger & 0 & P-Q & S & \sqrt{3/2}S^\dagger & \sqrt{2}Q \\ 0 & R^\dagger & S^\dagger & P+Q & -\sqrt{2}R^\dagger & -S^\dagger/\sqrt{2} \\ -S^\dagger/\sqrt{2} & -\sqrt{2}Q^\dagger & \sqrt{3/2}S & -\sqrt{2}R & P+\Delta & 0 \\ \sqrt{2}R & \sqrt{3/2}S^\dagger & \sqrt{2}Q^\dagger & -S/\sqrt{2} & 0 & P+\Delta \end{pmatrix}, \tag{C.11}$$

with

$$\begin{aligned} P &= \frac{\hbar^2\gamma_1}{2m_e}\left(k_x^2+k_y^2+k_z^2\right) \\ Q &= \frac{\hbar^2\gamma_2}{2m_e}\left(k_x^2+k_y^2-2k_z^2\right) \\ R &= \sqrt{3}\frac{\hbar^2}{2m_e}\left[-\gamma_2\left(k_x^2-k_y^2\right)+i2\gamma_3 k_x k_y\right] \\ S &= \sqrt{3}\frac{\hbar^2\gamma_3}{2m_e}\left(k_x-ik_y\right)k_z \\ \Delta &\equiv \frac{2\hbar i}{4m_e^2c^2}\langle X \mid \frac{\partial U}{\partial x}p_y+\frac{\partial U}{\partial y}p_x \mid Y\rangle. \end{aligned} \tag{C.12}$$

In GaAs, the split-off energy, Δ is ~ 0.3 eV. In most cases, Δ is much larger than any of the off-diagonal coupling elements of the Luttinger-Kohn Hamiltonian, and therefore the split-off states have very little effect on the states of interest (the heavy- and light-hole states). We can therefore safely neglect the last two rows and columns of the Luttinger-Kohn Hamiltonian when considering our microcavity system.

C.3 THE PIKUS-BIR HAMILTONIAN

Here I will outline the original work by G.E. Pikus and G.L. Bir [20], where they calculate the energy band shifts in a method similar to those methods used by J.M. Luttinger and W. Kohn [19]. The calculation begins with the simple relation that relates the new strained coordinates, x_i' in terms of the unstrained position x_i:

$$x_i' = x_i + \sum_j \epsilon_{ij}x_j, \tag{C.13}$$

where σ_{ij} is the strain tensor. From here, we can deduce a new canonical momentum p_i' as:

$$p_i' = i\hbar\frac{\partial}{\partial x_i'} = i\hbar\sum_j \frac{\partial x_j}{\partial x_i'}\frac{\partial}{\partial x_j} = i\hbar\left(\frac{\partial}{\partial x_i} - \sum_j \epsilon_{ij}\frac{\partial}{\partial x_j}\right) = p_i - \sum_j \epsilon_{ij}p_j. \tag{C.14}$$

The terms that show up in the Hamiltonian are p^2, or in tensor notation:

$$p'^2 = p^2 - 2\sum_{ij} p_i\epsilon_{ij}p_j, \tag{C.15}$$

where we have dropped terms of second-order in ϵ because the strains are assumed to be small.

The new potential $U(\mathbf{x}')$ can also be calculated. Here we assume the functional form of U does not change with strain. A first-order expansion of $U(\mathbf{x}')$ in terms of ϵ_{ij} gives

$$U(\mathbf{x}') = U(\mathbf{x}) + \sum_{ij} \underbrace{\frac{\partial U}{\partial \epsilon_{ij}}}_{\equiv U_{ij}} \epsilon_{ij}. \tag{C.16}$$

The Hamiltonian then becomes

$$H' = \frac{p'^2}{2m_e} + U(\mathbf{x}') = \frac{p^2}{2m_e} + U(\mathbf{x}) + \sum_{ij}\left(\frac{p_ip_j}{m_e} + U_{ij}\right)\epsilon_{ij}. \tag{C.17}$$

Now expanding H' in the $\mathbf{k}\cdot\mathbf{p}$ formalism, we first must consider how the new Bloch functions change with strain. It is obvious that the new crystal momentum, being analogous to $\mathbf{p}$ transforms the same way as p such that $\mathbf{k}'_i = \mathbf{k}_i - \sum_j \epsilon_{ij}\mathbf{k}_j$. The new Bloch functions are then represented as

$$\psi_{n\mathbf{k}'}(\mathbf{x}') = e^{i\mathbf{k}'\cdot\mathbf{x}'}u_{n\mathbf{k}'}(\mathbf{x}') = e^{i\mathbf{k}(1+\epsilon)\cdot(1-\epsilon)\mathbf{x}}u_{n\mathbf{k}'}(\mathbf{x}') = e^{i\mathbf{k}\cdot\mathbf{x}}u_{n\mathbf{k}'}(\mathbf{x}'). \tag{C.18}$$

Also note that the unstrained Bloch functions form an over complete basis for the expansion of the new Bloch functions, $u_{n\mathbf{k}'}(\mathbf{x}')$, only if the strain lowers the symmetry (or at least maintains the symmetry) of the lattice. When we apply these new Bloch functions to H' we find the new $\mathbf{k}\cdot\mathbf{p}$ Hamiltonian:

$$\begin{aligned}\left(\frac{p^2}{2m_e} + U(\mathbf{x}) + \frac{\hbar}{m_e}\mathbf{k}\cdot\mathbf{p} + \sum_{ij}\left(\frac{p_ip_j}{m_e} + U_{ij}\right)\epsilon_{ij} - \frac{2\hbar}{m_e}\sum_{ij}k_ip_j\epsilon_{ij}\right)u_{n\mathbf{k}'}(\mathbf{x}') \\ = \left(E_n(\mathbf{k}') - \frac{\hbar^2k^2}{2m_e}\right)u_{n\mathbf{k}'}(\mathbf{x}').\end{aligned} \tag{C.19}$$

Finally, we can expand this in the same method of perturbation theory (Löwdin perturbation theory) used for the Luttinger-Kohn Hamiltonian. The results give the same coupled set of equations as Eq. (C.11), except the matrix elements are reformulated:

$$H_{PB} = -\begin{pmatrix} P+Q & -S & R & 0 \\ -S^\dagger & P-Q & 0 & R \\ R^\dagger & 0 & P-Q & S \\ 0 & R^\dagger & S^\dagger & P+Q \end{pmatrix}, \tag{C.20}$$

where we have neglected the split-off band because it is not relevant. The constants are similar to the Luttinger constants with the exception that $k_\alpha k_\beta \Rightarrow \epsilon_{\alpha\beta}$ and

$$\begin{aligned} \frac{\hbar^2\gamma_1}{2m_e} &\Rightarrow -a_v \\ \frac{\hbar^2\gamma_2}{2m_e} &\Rightarrow -\frac{b}{2} \\ \frac{\hbar^2\gamma_3}{2m_e} &\Rightarrow -\frac{d}{2\sqrt{3}}. \end{aligned} \tag{C.21}$$

The new Pikus-Bir constants under these transformations become

$$\begin{aligned} P &= -a_v(\epsilon_{xx}+\epsilon_{yy}+\epsilon_{zz}) \\ Q &= -\frac{b}{2}(\epsilon_{xx}+\epsilon_{yy}-2\epsilon_{zz}) \\ R &= -\frac{\sqrt{3}b}{2}(\epsilon_{xx}-\epsilon_{yy}) - id\epsilon_{xy} \\ S &= -d(\epsilon_{xz}-i\epsilon_{yz}). \end{aligned} \tag{C.22}$$

BIBLIOGRAPHY

[1] R. Balili, V. Hartwell, D.W. Snoke, L. Pfeiffer, and K. West. *Science*, 316(1007), 2007.

[2] H. Deng, Gregor Weihs, Charles Santori, Jacqueline Bloch, and Yoshihisa Yamamoto. *Science*, 298(199), 2002.

[3] J. Kasprzak, M. Richard, A. Baas, P. Jeambrun, J.M. Keeling, F.M. Marchetti, M.H. Szymańska, R. André, J.L. Staehli, V. Savona, P.B. Littlewood, B. Deveaud, and Le Si Dang. *Nature*, 443(409), 2006.

[4] D. Bajoni, P. Senellart, A. Lemaitre, and J. Bloch. *Phys. Rev. B*, 76(201305(R)), 2007.

[5] E.A. Cerda-Méndez, D.N. Krizhanovskii, M. Wouters, R. Bradley, K. Biermann, K. Guda, R. Hey, P.V. Santos, D. Sarkar, and M.S. Skolnick. *Phys. Rev. Lett.*, 105(116402), 2010.

[6] A. Amo, D. Sanvitto, F.P. Laussy, D. Ballarini, E. del Valle, M.D. Martin, A. Lemaître, J. Bloch, D.N. Krizhanovskii, M.S. Skolnick, C. Tejedor, and L. Viña. *Phys. Rev. B*, 76(201305(R)), 2007.

[7] R. Balili and D.W. Snoke. *App. Phys. Lett.*, 88(031110), 2006.

[8] K. G. Lagoudakis, B. Pietka, M. Wouters, R. André, and B. Deveaud-Plédran. *Phys. Rev. Lett*, 105(120403), 2010.

[9] Daniele Bajoni, Pascale Senellart, Esther Wertz, Isabelle Sagnes, Audrey Miard, Aristide Lemaître, and Jacqueline Bloch. *Phys. Rev. Lett.*, 100(047401), 2008.

[10] B. Nelsen, R. Balili, D.W. Snoke, L. Pfeiffer, and K. West. *J. App. Phys.*, 105(122414), 2009.

[11] R. Balili, B. Nelsen, D.W. Snoke, L. Pfeiffer, and K. West. *Phys. Rev. B*, 79(075319), 2009.

[12] B. Nelsen, M. Steger, G. Liu, D.W. Snoke, L. Pfeiffer, and K. West. Sharp onset of bose-einstein condensation of long-lifetime polaritons. *Submitted to Nature.*

[13] J.J. Hopfield. *Phys. Rev.*, 112(5), 1958.

[14] C. Weisbuch, M. Nishioka, A. Ishikawa, and Y. Arakawa. *Phys. Rev. Lett.*, 69(23), 1992.

[15] P.G. Savvidis, J.J. Baumberg, R.M. Stevenson, M.S. Skolnick, D.M. Whittaker, and J.S. Roberts. *Phys. Rev. Lett.*, 84(7), 2000.

[16] David W. Snoke. *Solid State Physics Essential Concepts*. Addison-Wesley, 2009.

[17] Neil W. Ashcroft and N. David Mermin. *Solid State Physics*. Brooks Cole, 1st edition, 1976.

[18] Charles Kittel. *Introduction to Solid State Physics*. Wiley, eighth edition, 2004.

[19] J.M. Luttinger and W. Kohn. *Phys. Rev.*, 97(4), 1954.

[20] G.L. Bir and G.E. Pikus. *Symmetry and strain induced effects in semiconductors*. Wiley, 1972.

[21] L.D. Landau. *Sov. Phys. JETP*, 3(920), 1956.

[22] D. Gammon, B. V. Shanabrook, and D. S. Katzer. *Phys. Rev. Lett.*, 67(12), 1991.

[23] Shun Lien Chuang. *Physics of Photonic Devices*. John Wiley and Sons, Ink., second edition, 2009.

[24] J. J. Sakurai. *Modern Quantum Mechanics*, pages 337–339. Addison-Wesly, first edition, 1994.

[25] Sadao Adachi. *J. Appl. Phys.*, 58(3), 1985.

[26] S. Kéna-Cohen and S. R. Forrest. *Nature Photonics*, 4(371), 2010.

[27] G. Bastard, E. E. Mendez, L. L. Chang, and L. Esaki. *Phys. Rev. B.*, 26(4), 1982.

[28] Alexey V. Kavokin, Jeremy J. Baumberg, Guillaume Malpuech, and Fabrice P. Laussy. *Microcavities*. Oxford University Press, 1st edition, 2007.

[29] Bangfen Zhu. *Phys. Rev. B.*, 37(9), 1988.

[30] B.R Mollow. *Phys. Rev.*, 5(188), 1969.

[31] C. Weisbuch, M. Nishioka, A. Ishikawa, and Y. Arakawa. *Phys. Rev. B*, 53(16), 1996.

[32] Gabriel Christmann, Raphaël Butté, Eric Feltin, Jean-Francois Carlin, and Nicolas Grandjean. *App. Phys. Lett.*, 93(051102), 2008.

[33] Oliver Penrose and Lars Onsager. *Phys. Rev.*, 104(3), 1956.

[34] A.J. Leggit. *Quantum Liquids*, pages 31–33. Oxford University Press, first edition, 2006.

[35] N.N. Bogoliubov. *J. Phys. USSR*, 11(23), 1947.

[36] C.N. Yang. *Rev. Mod. Phys.*, 34(4), 1962.

[37] J.M. Kosterlitz and D.J. Thouless. *J. Phys. C*, 6(1181), 1973.

[38] R. Balili. *BOSE-EINSTEIN CONDENSATION OF MICROCAVITY POLARITONS*. PhD thesis, 2009.

[39] K.G. Lagoudakis, M. Wouters, M. Richard, A. Baas, I. Carusotto, R. André, Le Si Dang, and B. Deveaud-Plédran. *Nature Physics*, 4(706), 2008.

[40] L. Sapienza, A. Vasanelli, R. Colombelli, C. Ciuti, Y. Chassagneux, C. Manquest, U. Gennser, and C. Sirtori. *Phys. Rev. Lett.*, 100(136806), 2008.

[41] R. Houdré, C. Weisbuch, R.P. Stanley, U. Oesterle, P. Pellandini, and M. Ilegems. *Phys. Rev. Lett.*, 73(2043), 1994.

[42] Amnon Yariv and Pochi Yeh. *Photonics*, pages 199–204. Oxford University Press, sixth edition, 2007.

[43] S. Gehrsitz, F.K. Reinhart, C. Gourgon, N. Herres, A. Vonlanthen, and H. Sigg. *J. App. Phys.*, 87(7825), 2000.

[44] Richard Nötzel, Takashi Fukui, Hideki Hasegawa, Jiro Temmyo, and Toshiaki Tamamura. *App. Phys. Lett.*, 65(2854), 1994.

[45] A.P.D. Love, D.N. Krizhanovskii, R. Bouchekioua, D. Sanvitto, S. Al Rizeiqi, R. Bradley, M.S. Skolnick, P.R. Eastham, R. André, and Le Si Dang. *Phys. Rev. Lett.*, 101(067404), 2008.

[46] K.B. Davis, M.-O. Mewes, M.R. Andrews, N.J. van Druten, D.S. Durfee, D.M. Kurn, and W. Ketterle. *Phys. Rev. Lett.*, 75(22), 1995.

[47] E. Blackwood, M.J. Snelling, R.T. Harley, S.R. Andrews, and C.T.B. Foxon. *Phys. Rev. B*, 50(14246), 1994.

[48] N. Romanov and P. Baranov. *Nanotechnology*, 12(585), 201.

[49] Z. Vörös. *INTERACTION OF EXCITONS IN TWO-DIMENSIONAL POTENTIALS*. PhD thesis, 2008.

[50] V. Negoita and D.W. Snoke. *App. Phys. Lett.*, 75(14), 1999.

[51] E. Ivchenko and G. Pikus. *Superlattices and Other Heterostructures*. Springer, Berlin, second edition, 1997.

[52] E.L. Ivchenko, A.Yu. Kaminski, and U. Rössler. *Phys. Rev. B*, 54(8), 1996.

[53] H.W. van Kesteren, E.C. Cosman, and W.A.J.A. van der Poel. *Phys. Rev. B*, 41(8), 1990.

[54] R. Balili, B. Nelsen, and D.W. Snoke. *Phys. Rev. B*, 81(125311), 2010.

[55] E. Hanamura and H. Haug. *Phys. Rev. C*, 33(4), 1977.

[56] N.W. Sinclair, J.K. Wuenschell, Z. Vörös, B. Nelsen, D.W. Snoke, M.H. Szymanska, A. Chin, J. Keeling, L.N. Pfeiffer, and K.W. West. *Phys. Rev. B*, 83(245304), 2011.

[57] Z. Vörös, D.W. Snoke, L.N. Pfeiffer, and K.W. West. *Phys. Rev. Lett.*, 103(016403), 2009.

[58] P. Nozières. Bose-einstein condensation. Cambridge University Press, Cambridge, England, 1995.

[59] O.L. Berman, Yu.E. Lozovik, and D.W. Snoke. *Phys. Rev. B*, 77(155317), 2008.

[60] M. Holzmann, G. Baym, J.-P. Blaizot, and F. Laloë. *Proc. Natl. Acad. Sci. U.S.A.*, 104(1476), 2007.

[61] I. Carusotto and C. Ciuti. *Phys. Rev. B*, 72(125335), 2005.

[62] D. Whittaker. *Phys. Rev. B*, 63(193395), 2001.

[63] S. Utsunomiya, L. Tian, G. Roumpos, C.W. Lai, N. Kumada, T. Fujisawa, M. Kuwata-Gonokami, A. Löffler, S. Höfling, A. Forchel, and Y. Yamamoto. *Nat. Phys.*, 4(700), 2008.

[64] H. Deng, G. Weihs, D. Snoke, J. Bloch, and Y. Yamamoto. *Proc. Natl. Acad. Sci. U.S.A.*, 100(15318), 2003.

[65] Semiconductors: Basic data. Springer, New York, 1996.

[66] R.P. Stanley, R. Houdré, C. Weisbuch, U. Oesterle, and M. Ilegemes. *Phys. Rev. B*, 53(10995), 1996.

[67] R.K. Pathria. *Statistical Mechanics*, pages 63–64. Elsevier Butterworth-Heinemann, second edition, 1996.

[68] L. Pitaevskii and S. Stringari. *Bose-Einstein Condensation*. Oxford University Press, first edition, 2003.

[69] D.W. Snoke. *Solid State Comm.*, 146, 2008.

[70] D. Semkat, F. Richter, D. Kremp, G. Manzke, W.-D. Kraeft, and K. Hennenberger. *Phys. Rev. B*, 80(155201), 2009.

[71] V.E. Hartwell and D.W. Snoke. *Phys. Rev. B*, 82(075307), 2010.

[72] E.P. Gross. *Il Nuovo Cimento*, 20(1766), 1961.

[73] L.P. Pitaevskii. *Sov. Phys. JETP*, 13(451), 1961.

[74] Lydie Ferrier, Esther Wertz, Robert Johne, Dmitry D. Solnyshkov, Pascale Senellart, Isabelle Sagnes, Aristide Lemaître, Guilluame Malpuech, and Jacqueline Bloch. *Phys. Rev. Lett.*, 106(126401), 2010.

[75] E. Wertz, L. Ferrier, D. Solnyshkov, R. Johne, D. Sanvitto, A. Lemaître, I. Sagnes, R. Grousson, A.V. Kavokin, P. Senellart, G. Malpuech, and J. Bloch. *Nature Phys.*, 6(860-864), 2010.

[76] Georgios Roumpos, Wolfgang H. Nitsche, Sven Höfling, Alfred Forchel, and Yoshihisa Yamamoto. *Phys. Rev. Lett.*, 104(126403), 2010.

[77] G. Tosi, G. Christmann, N.G. Berloff, P. Tsotsis, T. Gao, Z. Hatzopoulos, P.G. Savvidis, and J.J. Baumberg. *Nature Phys*, In Press, 2012.

[78] A. Amo, S. Pigeon, C. Adrados, R. Houdré, E. Giacobino, C. Ciuti, and A. Bramati. *Phys. Rev. B*, 82(081301), 2010.

[79] Esther Wertz, Lydie Ferrier, Dmitry D. Solnyshkov, Pascale Senellart, Daniele Bajoni, Audrey Miard, Aristide Lemaître, Guilluame Malpuech, and Jacqueline Bloch. *Applied Phys. Lett.*, 95(051108), 2009.

[80] J. Wiersig, C. Gies, F. Jahnke, M. Aßmann, T. Berstermann, M. Bayer, C. Kistner, S. Reitzenstein, C. Schneider, S. Höfling, A. Forchel, C. Kruse, J. Kalden, and D. Hommel. *Nature Phys.*, 460(245-249), 2009.

[81] M. D. Fraser, G. Roumpos, and Y. Yamamoto. *New J. Phys*, 11(113048), 2009.

[82] D. Sanvitto, F.M. Marchetti, M.H. Szymańska, G. Tosi, M. Baudisch, F.P. Laussy, D.N. Krizhanovskii, M.S. Skolnick, L. Marrucci, A. Lemaître, J. Bloch, C. Tejedor, and L. Viña. *Nature Phys.*, 6(527-533), 2010.

[83] D. Sanvitto, A. Amo, D. Ballarini, M. De Giorgi, I. Carusotto, R. Hivet, F. Pisanello, V.G. Sala, P.S.S. Guimaraes, R. Houdré, E. Giacobino, C. Ciuti, A. Bramati, and G. Gigli. *Nature Photonics*, 5(610-614), 2011.

[84] Gaël Nardin, Gabriele Grosso, Yoan Léger, Barbara Pietka, Franǫis Morier-Genoud, and Benoît Deveaud-Plédran. *Nature Pysics*, 7(635-641), 2011.

[85] V. Hartwell. *DYNAMICS OF TRAPPED POLARITONS IN STRESSED GAAS QUANTUM WELL-MICROCAVITY STRUCTURES: EXPERIMENTS AND NUMERICAL SIMULATIONS*. PhD thesis, 2008.

[86] B. Sermage, G. Malpuech, A.V. Kavokin, and V. Thierry-Mieg. *Phys. Rev. B*, 64(081303), 2001.

[87] Alex Hayat, Christoph Lange, Lee A. Rozema, Ardavan Darabi, Henry M. van Driel, Aephraim M. Steinberg, Bryan Nelsen, David W. Snoke, Loren N. Pfeiffer, and Kenneth W. West. Dynamic stark effect in strongly coupled microcavity exciton-polaritons. *Submitted to Phys. Rev. Lett.*

[88] A. Mysyrowicz, D. Hulin, A. Antonetti, A. Migus, W.T. Masselink, and H. Morko¸ *Phys. Rev. Lett.*, 56(25), 1986.

[89] S. Schmitt-Rink, D.S. Chemla, and H. Haug. *Phys. Rev. B*, 37(2), 1988.

[90] M.R. Andrews, C.G. Townsend, H.-J. Miesner, D.S. Durfee, D.M. Kurn, and W. Ketterle. *Science*, 275(637-641), 1997.

[91] Yongke Sun, Scott E. Thompson, and Toshikazu Nishida. *Strain Effects in Semiconductors.* Springer, first edition, 2010.

[92] Per-Olov Löwdin. *J. Chem. Phys.*, 19(11), 1951.